

OPTICAL STUDIES OF IMPURITIES AND RADIATION
INDUCED DEFECTS IN KMgF_3

By

SOO IN YUN

//

Bachelor of Science
Pusan National University
Pusan, Korea
1960

Master of Science
Pusan National University
Pusan, Korea
1962

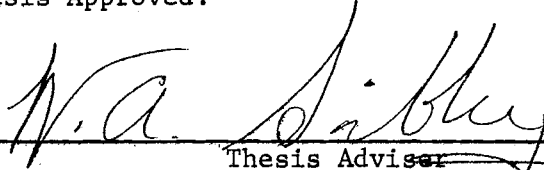
Master of Science
Carnegie-Mellon University
Pittsburgh, Pennsylvania
1970

Submitted to the Faculty of the Graduate College
of the Oklahoma State University
in partial fulfillment of the requirements
for the Degree of
DOCTOR OF PHILOSOPHY
May, 1973

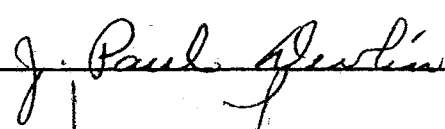
FEB 18 1974

OPTICAL STUDIES OF IMPURITIES AND RADIATION
INDUCED DEFECTS IN KMgF_3

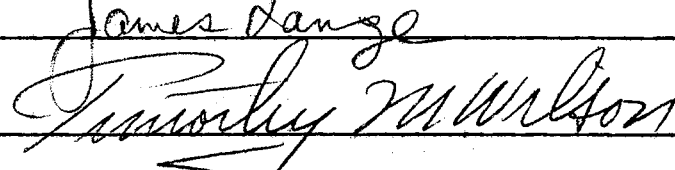
Thesis Approved:



Thesis Advisor



James Lange



D. D. Durham

Dean of the Graduate College

873471

ACKNOWLEDGMENTS

The author wishes to express his appreciation to his major adviser, W. A. Sibley, for his suggestion of the problem and patient guidance throughout this study. Appreciation is also expressed to R. C. Powell for many valuable discussions and for taking the lifetime data on some of the samples used in this work; to W. E. Vehse for sending several crystals to the author as well as for providing useful information; to E. Sonder and Y. Chen of the Oak Ridge National Laboratory for irradiating several samples and helpful discussions and suggestions; to the National Science Foundation for supporting this work.

Thanks are also extended to C. T. Butler, L. A. Kappers, L. Feuerhelm and J. A. MacInerney for their assistance during this work; to H. Hall and the staff of the Chemistry-Physics Machine Shop for the design and fabrication of the apparatus and to Mrs. Janet Saltee for her excellence in typing the manuscript.

Finally, special gratitude is expressed to my wife, Hyun Young, for her understanding and many sacrifices.

TABLE OF CONTENTS

Chapter	Page
I. INTRODUCTION.	1
II. THEORY.	8
Absorption and Emission of Photons	8
Polarized Bleaching.	21
Vibrational-Electronic Interaction	26
Configuration Coordinate Model for the Optical Band Shape.	30
Allowed Energy Terms of Mn^{2+} Ion ($3d^5$)	34
Selection Rules.	35
III. EXPERIMENTAL PROCEDURE.	41
IV. OPTICAL ABSORPTION AND EMISSION FROM DEFECTS IN $KMgF_3$. .	48
Color Center Absorption in $KMgF_3$	48
Color Center Emission in $KMgF_3$	58
590 nm Emission	58
465 nm Emission	63
750 nm Emission	67
Other Emission Bands.	71
Absorption in $KMgF_3:Mn$ Crystal	71
Emission in $KMgF_3:Mn$ Crystals.	88
V. DISCUSSION.	101
VI. SUMMARY AND PROBLEMS FOR FURTHER STUDY.	115
BIBLIOGRAPHY.	118

LIST OF TABLES

Table	Page
I. Absorption Coefficient for Linearly Polarized Light as a Function of the Type of Center	23
II. Relative Intensities of Polarized Emission	25
III. Enumeration of Allowed Terms of $3d^5$	36
IV. Observed and Predicted Absorption Coefficients From Oriented F_2 Centers in $KMgF_3$	56
V. Emission Intensity Ratios for Samples Bleached With Polarized Light and the Defect Distributions Determined From the Ratios	61
VI. The Spacing of the Lines Both in Emission and Absorption at LHeT.	85
VII. Assignment of Mn^{2+} Transitions in $KMgF_3:KMnF_3$ and in Electron Irradiated $KMgF_3:Mn$ at $77^\circ K$	86

LIST OF FIGURES

Figure	Page
1. Two Unit Cells for KMgF_3	3
2. Schematic Illustrations of the Sample Orientation With Respect to Both the Incident Light and the Detection Systems for Absorption and Emission and of Defect Orientations in Cubic Crystals.	22
3. Block Diagram of Luminescence Apparatus.	44
4. Response of Luminescence Detection System as a Function of Photon Energy.	45
5. Spectral Irradiance of PEK-75 Xenon Short Arc Lamp as a Function of Photon Energy.	46
6. Absorption Spectrum of KMgF_3 at 15°K Following an Electron Irradiation at 300°K	49
7. Gaussian Plot for 570 nm Absorption Band in KMgF_3	50
8. Temperature Dependence of $W_{1/2}$ and ϵ_{max}^A for 570 nm Absorption Band in KMgF_3	51
9. Temperature Dependence of Half-Width of 570 nm Absorption Band in KMgF_3	52
10. Anisotropic Absorption in KMgF_3 as a Function of Photon Energy Following an 254 nm Optical Orientation	54
11. Isochronal Annealing Curves for 395 (F_3), 445 (F_2), 275 (F) and 570 nm Absorption Bands in KMgF_3	57
12. Absorption Spectrum in KMgF_3 Following a 254 nm Bleaching at 200°K	59
13. Annealing Curves for 220 and 340 nm Band in KMgF_3	60
14. Plot of the Emission Intensity at 590 nm Due to 436 nm Light Excitation Versus the Absorption Coefficient at 445 nm	62
15. Excitation Spectrum for 590 nm (F_2) Emission Band in KMgF_3 at 300°K	64

LIST OF FIGURES (Continued)

Figure	Page
16. Excitation Spectrum and 590 nm (F_2) Emission Band in $KMgF_3$ at 15°K.	65
17. Emission Intensity at 465 nm Due to 365 nm Light Excitation as a Function of the Absorption Coefficient at 395 nm	66
18. Excitation Spectrum for 465 nm (F_3) Emission Band in $KMgF_3$ at 300°K	68
19. Excitation Spectrum and 465 nm (F_3) Emission Band in $KMgF_3$ at 15°K.	69
20. Plot of the Emission Intensity at 750 nm Due to 580 nm Light Excitation Versus the Absorption Coefficient at 570 nm	70
21. Excitation Spectrum and 750 nm Emission Band in $KMgF_3$ at 15°K	72
22. Gaussian Plot for 750 nm Emission Band in $KMgF_3$	73
23. Temperature Dependence of $W_{1/2}$ and ϵ_{max}^A for 750 nm Emission Band in $KMgF_3$	74
24. Temperature Dependence of Half-Width of 750 nm Emission Band in $KMgF_3$	75
25. Excitation Spectrum and 410 nm Emission Band in $KMgF_3$ at 15°K	76
26. 465, 590, and 750 nm Emission Bands Excited by Light of Wavelength 395, 445, and 570 nm at 300°K	77
27. Absorption Spectrum and Excitation Spectrum of $KMgF_3:Mn$ (1.4 at. %) at 300°K Following an Electron Irradiation at 80°K.	78
28. Absorption Spectrum of $KMnF_3$ at 300°K.	80
29. (a) Effect of a Room Temperature [100] Polarized Bleach on an Electron Irradiated $KMgF_3:Mn$ (1.4 at. %) Crystal. Measuring Light Polarized Along [010] (—) Along [100] (·····). (b) Anisotropic Absorption Curve From (a).	81
30. Side Bands at 394, 427, 435, and 597 nm Near the Major Absorption Bands at 410 and 565 nm at 300°K.	82

LIST OF FIGURES (Continued)

Figure	Page
31. Temperature Dependence of Small Bands Near the Major Absorption Bands at 410 and 565 nm in an Electron Irradiated $\text{KMgF}_3\text{:Mn}$ (1.4 at. %)	83
32. Absorption Spectra of 0.4 and 0.04 at. % Mn-Doped KMgF_3 Crystal Following an Electron Irradiated at 80°K	87
33. Optical Bleaching Curves of Absorption Bands in $\text{KMgF}_3\text{:Mn}$ (1.4 at. %) Which was Electron Irradiation at 80°K	89
34. Absorption Spectrum of $\text{KMgF}_3\text{:Mn}$ (1.4 at. %) at 300°K Following an Electron Irradiation at 300°K	90
35. Absorption Spectrum at 15°K of $\text{KMgF}_3\text{:Mn}$ (1.4 at. %) Following an Electron Irradiation at 300°K	91
36. 250 nm Absorption Band in $\text{KMgF}_3\text{:Mn}$ (0.04 at. %) at 273°K After Bleach With UV Light at 273°K	92
37. Emission Bands in an Electron Irradiated $\text{KMgF}_3\text{:Mn}$ (1.4 at. %). The left side of the figure is the emission band at 300°K and the right side of the figure is the emission band at 4.2°K . Inset shows the temperature dependence of the peak positions for the emission band in electron irradiated $\text{KMgF}_3\text{:Mn}$ (1.4 at. %)	94
38. Absorption Spectrum and Excitation Spectrum for an Electron Irradiated $\text{KMgF}_3\text{:Mn}$ (1.4 at. %) at 77°K	95
39. Excitation Spectrum for 720 nm Emission Band in an Irradiated $\text{KMgF}_3\text{:Mn}$ (1.4 at. %) at 80°K	96
40. 720 and 750 nm Emission Bands at 300°K in an Electron Irradiated $\text{KMgF}_3\text{:Mn}$ (0.04 at. %)	98
41. Excitation Spectrum of 720 and 650 nm Emission Band in $\text{KMgF}_3\text{:Mn}$ (0.4 at. %) Following an Electron Irradiation at 300°K	99
42. Emission Spectrum in KMnF_3 at 15°K	100
43. Configuration Coordinate Diagram for the Center Responsible for 570 nm Absorption Band and 750 nm Emission Band in KMgF_3	102
44. Orgel Diagram for $3d^5$ Configuration.	106

LIST OF FIGURES (Continued)

Figure		Page
45.	Temperature Dependence of the Emission Lifetime for 677 nm Emission in $\text{KMgF}_3\text{:Mn}$ (1.4 at. %)	110
46.	Configuration Coordinate Diagram for the Luminescence System of Mn^{2+} in an Electron Irradiated $\text{KMgF}_3\text{:Mn}$	112

CHAPTER I

INTRODUCTION

When an alkali-halide crystal is heated in the vapor of an alkali metal⁽¹⁻³⁾, it acquires a characteristic color. It is found that this color is due to a bell-shaped absorption band in colored alkali-halide crystal. Pohl⁽⁴⁾ called this band the F band and the defects responsible for it the F centers.

Color centers in solids have been studied intensively for nearly half a century. During this time a number of excellent reviews of the subject have appeared. Some of these are summaries and books by Seitz^(5,6), Schulman and Compton⁽⁷⁾, Compton and Rabin⁽⁸⁾, Fowler⁽⁹⁾, and Crawford and Slifkin⁽¹⁰⁾.

Color centers may be produced by the methods of additive coloration⁽¹¹⁻¹⁴⁾, electrolytic coloration^(11,15-17) or by exposure to ionizing radiation (electrons, protons, X-rays, and gamma-rays)⁽¹⁸⁾ or energetic particles (neutrons)⁽¹⁸⁻¹⁹⁾. These processes produce intrinsic defects in the lattice as well as changes in the state of impurities in the crystal. Sometimes the changes may involve the production of intrinsic defects bound to impurities, or they may only involve a change in the valence state of the impurities.

From time to time specific models of color centers have been proposed by various investigators^(1,5,6,20). In 1937 de Boer⁽²¹⁾ proposed a model for the F center, which consisted of an electron trapped at the

position of a halogen ion vacancy. This model has proved to be correct for alkali materials. Since color center research is important for materials other than alkali-halides, it is useful to have a reasonably consistent nomenclature for color centers which is applicable to all polar crystals. According to the new nomenclature for defect centers suggested by Sonder and Sibley⁽¹⁸⁾, the designation F center is reserved for negative-ion vacancies containing the same number of electrons as the charge of the normal lattice ion. The existence of F center aggregates called F_2 , F_3 , and F_4 centers (M, R, and N centers) has also been reasonably well established by means of optical and spin resonance measurements. The F_2 center consists of two adjacent F centers and the F_3 center is formed from three adjacent F centers. The self-trapped hole center (V_k or X_2^- center) consists of a hole which is self-trapped on two adjacent anions.

Many important properties of solids are controlled as much or more by the defects and impurities in the solids as by the nature of the host crystal. Thus, it is important to understand how materials properties are altered by inadvertent or deliberate irradiation. Moreover, materials that will be used in high radiation fields must be tested to determine how seriously hostile environments affect them.

Even though considerable color center research has been done on alkali-halides, relatively few studies have been made on other transparent ionic materials. Perovskite materials such as $KMgF_3$, $KZnF_3$ and $KMnF_3$ are technologically important because of their potential usefulness as phosphors, laser hosts, and other devices⁽²²⁻²⁶⁾. The two units cells for $KMgF_3$ are shown in Figure 1. The "as grown" $KMgF_3$ is transparent from about 120 to 10,000 nm⁽²⁷⁾ and has a lattice constant of

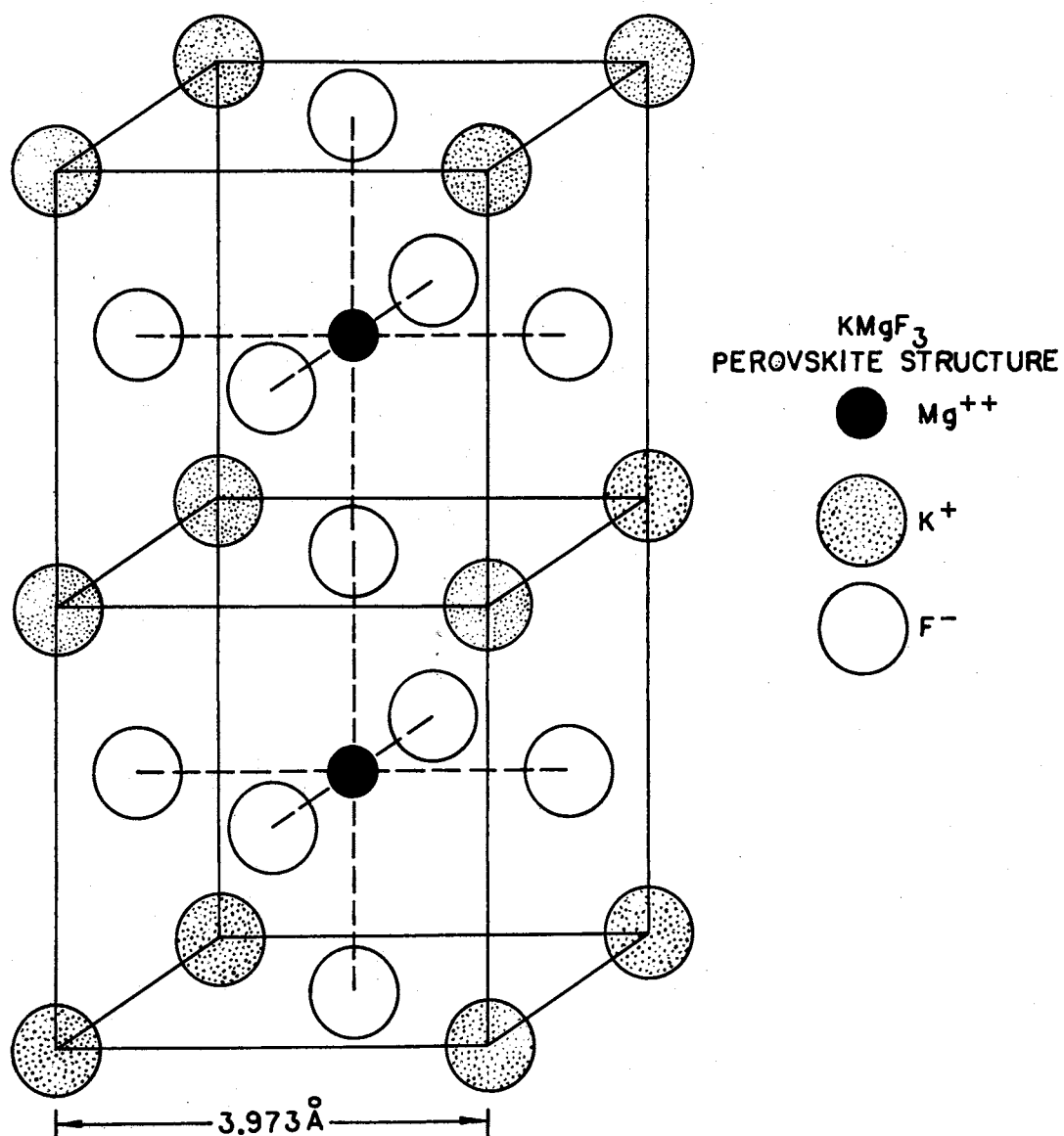


Figure 1. Two Unit Cells for KMgF_3

3.973⁽²⁸⁾.

Recently there have been several investigations of radiation induced defects in KMgF_3 crystals^(27,29-33). These experiments have dealt primarily with the identification of the optical absorption bands arising from these defects, with the kinetics of the defects themselves, and the radiation damage mechanism. It would be highly desirable to study the emission from irradiated KMgF_3 and make assignments of the observed bands to either defects induced by radiation or present as impurities.

In KMgF_3 crystals the F centers have D_{4h} symmetry, F_2 centers (M centers) and V_k centers (X_2^- centers) have C_{2v} symmetry, and F_3 centers (R centers) have C_{3v} symmetry. Optical bleaching with $[110]$ and/or $[100]$ polarized light has been shown to result in anisotropic absorption characteristic of each type of oriented centers⁽³⁴⁾. Once the defects have been rearranged into orientations which are no longer random it should be possible to observe polarized emission from these defects, and to use this polarized emission to identify the defects responsible for the various emission bands seen after irradiation. From the excitation spectrum technique it is possible to show which absorption bands are responsible for particular emission bands.

Hall and Leggeat⁽²⁹⁾, tentatively identified F, F_2 and V_k center absorption bands in an irradiated KMgF_3 crystal by means of electron spin resonance (ESR) and polarized luminescence. Riley and Sibley^(27, 31) identified F, F_2 , F_3 and V_k center absorption bands by using the polarized bleaching method and from the kinetics of these defects. In addition, they tentatively identified F_2 and F_3 center emission bands in electron irradiated KMgF_3 crystals. More extensive studies on V_k centers in KMgF_3 have been done by Lewis et al.⁽³³⁾

Over the past years much research has been done on optical absorption bands in KMnF_3 , RbMnF_3 , and MnF_2 ⁽³⁵⁻³⁸⁾. The magnetic ordering and the fluorescence of KMnF_3 and other concentrated Mn^{2+} systems have been investigated by Holloway, et al. ⁽³⁹⁾ and by Klasens et al. ⁽⁴⁰⁾ They observed that the fluorescence spectral output of these concentrated Mn^{2+} systems are strongly dependent on temperature, especially in the regions close to T_N and $\frac{1}{2}T_N$ (T_N is Néel temperature). This effect was not observed in the fluorescence of dilute Mn^{2+} systems.

Over the past decade or so the excellent research of McClure, Ferguson, their coworkers and others ^(35,41-51) have extended our knowledge of the 3d impurity ion transitions in various crystal fields. The optical spectra of single transition metal ions in dilute crystals are now well understood and the details of the spectra can be explained with some success. However, much work has to be done in understanding the magnetic exchange interactions among the paramagnetic ions in crystals. The discovery of the absorption bands due to pairs of Cr^{3+} ions in Al_2O_3 ⁽⁵²⁾ opened a new era. Many other crystals have been investigated ^(46,52-57) and have been analyzed in terms of exchange coupling with the Heisenberg Hamiltonian $\vec{J}\vec{S}\cdot\vec{S}$. Unfortunately, these transitions are strongly forbidden and difficult to observe experimentally. In the case of an O_h crystal field symmetry many of these transitions are spin and parity forbidden having extremely small oscillator strength in the range of 10^{-7} . This is a severe limitation since only a few absorption bands can be studied even in relatively thick crystals. High concentrations of 3d ions result in other problems such as concentration quenching of luminescence and precipitation effects. Therefore, it would be highly desirable to find a way to increase the intensity of these

strongly forbidden transitions. High resolution optical data for more of these transitions would greatly improve our understanding of spin orbit coupling, exchange effects and the interaction of 3d ions with the lattice phonons.

Considerable research has been done on the pair transitions that occur when ionic crystals are doped with Mn, Mn and Cu, Mn and Ni, etc. (35,45,46,53,58-60). From these measurements it was found that the oscillator strength for the impurity pair transitions can be increased up to three orders of magnitude greater than that for a single impurity ion. This enhancement is attributed to exchange interactions which partially lift the spin forbiddenness of the transitions.

Recently Sell and Stokowski⁽⁶¹⁾ have reported that they observed in MnF_2 a small increase in the Mn^{2+} absorption induced by the presence of Ca impurities. These Ca impurities lower the crystal field symmetry around the Mn^{2+} ion site and partially remove the parity forbiddenness of the transitions.

Vehse and Sibley⁽³⁰⁾ found a series of optical absorption bands in Mn-doped KMgF_3 crystals which were electron irradiated at 80°K. They suggested an F center-impurity complex as being responsible for these bands. It is possible to optically bleach the center with polarized light to produce a dichroism which indicates that the defect orientation is $\langle 100 \rangle$. Moreover, optical bleaching experiments allow a determination of which electric vector, $\vec{e}_{\ell mn}$, is responsible for the transition. It should be noted that the polarization of the F center-complex is accomplished by a selective destruction of the complex rather than a reorientation. This excludes the model of a single Mn-ion perturbed by an F center and strongly suggests that two Mn ions are involved. In fact, a

study of the perovskite structure suggests that the simplest model for a defect which satisfies all of the experimental observations is that of an F center at a fluorine site between two adjacent substitutional Mn-ion impurities. We designate this defect which has its major axis along $\langle 100 \rangle$, by the symbol $\text{Mn}-F-\text{Mn}$. The addition of defects next to the Mn impurities, such as an F center replacing a fluorine ion, should result in even greater effective oscillator strength for the transitions due to exchange interactions and symmetry changes. Okada et al.⁽⁶²⁾ have studied color centers in MgO:Ni induced by neutron irradiation. They found new absorption bands at 365 and 460 nm and suggested that the Ni ion center associated with a vacancy or an irradiation defect in the MgO crystal was responsible for these two new absorption bands. They also considered that the 365 nm band might be due to a defect center resembling the F_A center in alkali-halide crystals. Agrawal and Rao⁽⁶³⁾ have reported several new absorption bands in $\text{CaF}_2:\text{Mn}$ which has been irradiated. But they gave no explanation as to the origin of the new bands.

The object of the present investigation is twofold:

(1) to study the radiation damage, emphasizing the optical emission from irradiated KMgF_3 crystals, and

(2) to study the luminescence and the mechanism involved in the enhancement of the Mn^{2+} ion transitions in irradiated $\text{KMgF}_3:\text{Mn}$ crystals.

CHAPTER II

THEORY

An outline of the theory related to the absorption and emission of photons and phonons by point defects in solids will now be presented. We consider the absorption and emission of light, polarized bleaching experiments, vibrational-electron interactions and finally selection rules.

Absorption and Emission of Photons

The theory of optical absorption by ions in crystals has been reviewed by Shore and Menzel⁽⁶⁴⁾, Di Bartolo⁽⁶⁵⁾, Fowler⁽⁶⁶⁾, Fitchen⁽⁶⁷⁾, Schiff⁽⁶⁸⁾, Stepanov et al.⁽⁶⁹⁾, Dexter⁽⁷⁰⁾, Condon and Shortley⁽⁷¹⁾, and Pines⁽⁷²⁾. The nonrelativistic Hamiltonian for an ion with one electron and the electromagnetic field is⁽⁶⁴⁾

$$H = \frac{1}{2m} \left(\vec{p} - \frac{e\vec{A}}{c} \right)^2 + e\phi + \frac{1}{8\pi} \int (\vec{E}^2 + \vec{H}^2) d\tau + \frac{e}{mc} \vec{s} \cdot \vec{H}, \quad (1)$$

where \vec{p} is the generalized momentum, \vec{A} is the vector potential, ϕ , the potential due to central charge, and \vec{s} , the spin of an electron. By using the creation and annihilation operators $a_k^{\lambda+}$ and a_k^λ , the vector potential \vec{A} can be expressed by⁽⁶⁵⁾

$$\vec{A} = \sum_{k,\lambda} \left(\frac{hc^2}{\omega_k V} \right)^{1/2} \hat{n}_k^\lambda (a_k^\lambda e^{i\vec{k} \cdot \vec{r}} + a_k^{\lambda+} e^{-i\vec{k} \cdot \vec{r}}), \quad (2)$$

where λ indicates polarization, $\hat{\Pi}_k^\lambda$ is the unit vector in the direction of polarization, and \vec{k} is the wave vector for the electromagnetic wave.

H consists of four parts:

$$H = H_0 + H_R + H_{\text{int}} + H', \quad (3)$$

where

$$H_0 = \frac{\vec{p}^2}{2m} + e\phi, \quad (4)$$

$$H_R = \frac{1}{8\pi} \int (\vec{E}^2 + \vec{H}^2) d\tau = \sum_{k,\lambda} (a_k^{\lambda+} a_k^\lambda + \frac{1}{2} \hbar \omega_k), \quad (5)$$

$$\begin{aligned} H_{\text{int}} &= -\frac{e}{mc} \vec{p} \cdot \vec{A} + \frac{e}{mc} \vec{s} \cdot \vec{H} \\ &= -\frac{e}{mc} \sum_{k,\lambda} \left(\frac{\hbar}{\omega_k V} \right)^{1/2} \hat{\Pi}_k^\lambda \cdot \vec{p} (a_k^\lambda e^{i\vec{k} \cdot \vec{r}} + a_k^{\lambda+} e^{-i\vec{k} \cdot \vec{r}}) + \frac{e}{mc} \vec{s} \cdot \vec{H}, \end{aligned} \quad (6)$$

and

$$\begin{aligned} H' &= \frac{e^2}{2mc^2} \vec{A}^2 = \frac{e^2}{m} \frac{\hbar}{V} \sum_{k,\lambda} \sum_{k',\lambda'} (\omega_k \omega_{k'})^{-1/2} \hat{\Pi}_k^\lambda \\ &\quad \cdot \hat{\Pi}_{k'}^{\lambda'} (a_k^\lambda e^{i\vec{k} \cdot \vec{r}} + a_k^{\lambda+} e^{-i\vec{k} \cdot \vec{r}}) (a_{k'}^{\lambda'} e^{i\vec{k}' \cdot \vec{r}} + a_{k'}^{\lambda'+} e^{-i\vec{k}' \cdot \vec{r}}). \end{aligned} \quad (7)$$

H_R is the Hamiltonian for the radiation field alone, and H' corresponds to various two-photon processes. These two-photon processes are important in studying the scattering of photons, but can be neglected for our purposes. The term $\frac{1}{2} \hbar \omega_k$ in H_R is the zero-point energy and infinite. This infinite energy is not objectionable since it does not interact with matter and is customary to subtract this contribution from H_R .

Let us take the periodic boundary condition over a cube of volume V . The number of final states of photon in the range of \vec{k} and $\vec{k} + d\vec{k}$ with a particular polarization is given by

$$\begin{aligned} g(\vec{k})d\vec{k} &= \frac{V}{(2\pi)^3} d\vec{k} = \frac{V}{8\pi^3} k^2 dk d\Omega_k = \frac{V}{8\pi^3 c^3} \omega_k^2 d\omega_k d\Omega_k \\ &= g(\omega_k) d\omega_k d\Omega_k, \end{aligned} \quad (8)$$

where $d\Omega_k$ indicates the element of solid angle in the direction \vec{k} . The density of final states $g(\nu_k)$ for the emission or absorption of frequency ν_k and a certain polarization, in any direction of space, is given by integrating Equation (8):

$$4\pi g(\nu_k) = g(\omega_k) \frac{d\omega_k}{d\nu_k} 4\pi = \frac{4\pi V}{3} \nu_k^2. \quad (9)$$

From Fermi's Golden rule^(68,73), the radiative transition rate

$P_k(i \rightarrow f)$ is given by

$$P_k(i \rightarrow f) = \frac{2\pi}{\hbar} |M_k|^2 g(\omega_k) = \frac{1}{\hbar} |M_k|^2 g(\nu_k), \quad (10)$$

where $M_k = \langle \Psi_f | H_{int} | \Psi_i \rangle$, and $|\Psi_f\rangle$ and $|\Psi_i\rangle$ are the final (fth) and initial (ith) states, respectively, of the total system (ion and radiation). For the function $|\Psi_i\rangle = |\Psi_i^{el}\rangle |n_2\rangle \dots |n_k\rangle \dots |a_k^+\rangle$ and a_k have the following relations:^(64,72)

$$a_k^+ |\Psi_i\rangle = (n_k + 1)^{\frac{1}{2}} |\Psi_i^{el}\rangle |n_1\rangle \dots |n_{k-1}\rangle |n_k+1\rangle |n_{k+1}\rangle \dots,$$

and

$$a_k |\Psi_i\rangle = (n_k)^{\frac{1}{2}} |\Psi_i^{el}\rangle |n_1\rangle \dots |n_{k-1}\rangle |n_k-1\rangle |n_{k+1}\rangle \dots$$

The n_k 's are commonly called occupation numbers for each k , because they specify the number of photons of each type composing the field.

The transition rate for the system to lose or gain a photon of k th mode and polarization \hat{n}_k^λ , in the direction given by $d\Omega_k$ is⁽⁶⁵⁾

$$P_k^\lambda (i \rightarrow f) d\Omega_k = \frac{V}{8\pi^3 c^3} \omega_k^3 d\Omega_k \frac{2\pi}{\hbar} |M_k^\lambda|^2$$

$$= \frac{\omega_k^2}{hc^3 m} \left\{ \frac{n_k}{n_k+1} \right\} \left| \begin{array}{c} \langle \Psi_f^{el} | \sum_i e^{i\vec{k} \cdot \vec{r}_i} \hat{n}_k^\lambda \cdot \vec{p}_i | \Psi_i^{el} \rangle \\ \langle \Psi_f^{el} | \sum_i e^{-i\vec{k} \cdot \vec{r}_i} \hat{n}_k^\lambda \cdot \vec{p}_i | \Psi_i^{el} \rangle \end{array} \right|^2 d\Omega_k, \quad (11)$$

where the upper row corresponds to the absorption and the lower row to the emission of a photon and $|\Psi_f^{el}\rangle$ and $|\Psi_i^{el}\rangle$ represent the final and initial states, respectively, of the ionic system. Using the orthogonality of \vec{k} and \hat{n}_k^λ and the hermiticity of the operator $\vec{V} = -\frac{\vec{p}}{\hbar}$, we have

$|\langle \Psi_f^{el} | e^{-i\vec{k} \cdot \vec{r}} \hat{n}_k^\lambda \cdot \vec{p} | \Psi_i^{el} \rangle|^2 = |\langle \Psi_i^{el} | e^{i\vec{k} \cdot \vec{r}} \hat{n}_k^\lambda \cdot \vec{p} | \Psi_f^{el} \rangle|^2$. If we choose the dipole approximation of the expansion (first term only in the expansion)

$$(e^{\pm i\vec{k} \cdot \vec{r}}) \cdot \vec{p} = \vec{p} \pm i(\vec{k} \cdot \vec{r}) \cdot \vec{p} + \dots, \quad (12)$$

then corresponding H_{int} becomes

$$H_{int}^{EL} = -\frac{e}{m} \sum_{k,\lambda} \left(\frac{2\pi\hbar}{\omega_k V} \right)^{1/2} \hat{n}_k^\lambda \cdot \vec{p} (a_k^\lambda + a_k^{\lambda+}). \quad (13)$$

Since

$$P_x = m \frac{dx}{dt} = i \frac{m}{\hbar} [H, x],$$

then

$$H_{int}^{EL} = -i \sum_{k,\lambda} \left(\frac{2\pi\hbar\omega_k}{V} \right)^{1/2} [a_k^\lambda \hat{n}_k^\lambda + a_k^{\lambda+} \hat{n}_k^\lambda] \cdot \left(\sum_i \vec{e}_i \vec{r}_i \right) \quad (14)$$

where i is the sum over all the electron coordinates for a multielectron ion. H_{int}^{E1} is called an electric dipole interaction Hamiltonian. The first term corresponds to absorption (removes a photon), the second, to emission (adds a photon) of radiation. The second term in Equation (12),

$$(\vec{k} \cdot \vec{r}) \cdot \vec{P} = \frac{1}{2} \{ (\vec{k} \cdot \vec{r}) \vec{P} + (\vec{k} \cdot \vec{P}) \vec{r} \} + \frac{1}{2} \{ (\vec{k} \cdot \vec{r}) \vec{P} - (\vec{k} \cdot \vec{P}) \vec{r} \}, \quad (15)$$

the second term of Equation (15) can be expressed by

$$-\frac{1}{2} \{ \vec{k} \times (\vec{r} \times \vec{P}) \} = -\frac{\omega_k}{2c} (\hat{1}_k \times \vec{L}),$$

and the corresponding H_{int} term becomes,

$$H_{int}^{M1} = \frac{1}{k} \sum_{\lambda} \left(\frac{\hbar \omega_k}{V} \right)^{\frac{1}{2}} (a_k^{\lambda} \hat{\Pi}_k^{\lambda} - a_k^{\lambda+} \hat{\Pi}_k^{\lambda}) \cdot [\hat{1}_k \times \frac{e}{2mc} (\vec{L} + 2\vec{S})]. \quad (16)$$

H_{int}^{M1} is called a magnetic dipole interaction Hamiltonian, where $\vec{L} = \sum_i \vec{\ell}_i$, $\vec{S} = \sum_i \vec{s}_i$, and $\hat{1}_k$ is the unit vector in the direction of \vec{k} . Here we have added the spin magnetic moment $\frac{e}{mc} \vec{S}$. The corresponding Hamiltonian for the first term in Equation (15) will be the electric quadrupole interaction Hamiltonian.

The transition rates for the absorption or emission of a photon from or to any direction with any polarization are given by

$$P_i(i \rightarrow f) = \frac{\omega_k^3}{hc^3} \left\{ \frac{n_k}{n_k+1} \right\} \sum_{\lambda} \int d\Omega_k |\langle \psi_f^{el} | \vec{M} \cdot \hat{\Pi}_k^{\lambda} | \psi_i^{el} \rangle|^2, \quad (17)$$

where the upper row describes an absorption of one photon, whereas the lower row describes an emission of a photon. Note that although the probability for absorption is proportional to the initial number of

photons n_k , the emission probability is proportional to $n_k + 1$. Therefore, emission can be induced by the presence of a field, or can take place spontaneously. \vec{M} in Equation (17) may be any dipole moment.

The probability of spontaneous emission of one k th mode photon in the direction $k(\theta, \phi)$ is

$$dA_k(i \rightarrow f) = \sum_{\lambda} \frac{\omega_k^3}{\lambda hc^3} |\langle \psi_f^{e1} | \vec{M} \cdot \hat{n}_k^\lambda | \psi_i^{e1} \rangle|^2 d\Omega_k. \quad (18)$$

By integrating over the whole space and considering the orthogonality of \hat{n}_k^1 , \hat{n}_k^2 , and \vec{k} we have

$$\begin{aligned} A_k(i \rightarrow f) &= \frac{\omega_k^3}{hc^3} |\langle \psi_f^{e1} | \vec{M} | \psi_i^{e1} \rangle|^2 \int_0^\pi \int_0^{2\pi} \sin^3 \theta \, d\theta \, d\phi \\ &= \frac{8\pi\omega_k^3}{3hc^3} |\langle \psi_f^{e1} | \vec{M} | \psi_i^{e1} \rangle|^2. \end{aligned} \quad (19)$$

This is the probability of spontaneous emission of a photon of k th mode from level i to f . For convenience we write Equation (19) in the following form:

$$A_{fi} = \frac{8\pi\omega^3}{3hc^3} |M|^2, \quad (20)$$

here M is the matrix element of the dipole operator.

We can now introduce the dimensionless quantity⁽⁶⁵⁾,

$$f_{fi} = \frac{2m\omega}{3\hbar e^2} |M|^2, \quad (21)$$

and f_{fi} is called the oscillator strength of the transition from i state

to f state. Since the relation between A_{fi} and the radiative lifetime

$$\tau_o \text{ is } A_{fi} = \frac{1}{\tau_o},$$

$$f_{fi} \tau_o = \frac{mc^3}{2e^2 \omega^2} = 1.51 \lambda_o^2, \quad (22)$$

where λ_o is the wavelength of the radiation in the vacuum.

Let ρ_v is the energy density of the radiative field, then

$$\int \rho_v dv = \sum_{k,\lambda} \frac{h\nu_k (n_k^\lambda + \frac{1}{2})}{V} = \frac{2}{V} \int dk g(k) h\nu_k (n_k + \frac{1}{2}), \quad (23)$$

where the factor two arises from the two polarization directions. Using Equation (9), Equation (23), is given by

$$\int \rho_v dv = \int \frac{8\pi\nu^2}{c^3} h\nu (n_v + \frac{1}{2}) dv. \quad (24)$$

Then we have

$$\rho_v = \frac{8\pi h\nu^3}{c^3} n_v, \quad (25)$$

and the term $1/2$ has been eliminated.

If B is the transition rate of the induced emission of a photon of frequency ν , then

$$\frac{A}{B} = \frac{\rho_v}{n_v} = \frac{8\pi h\nu^3}{c^3},$$

where A and B are the so-called Einstein coefficients^(65,69). Considering the electric field in the crystal

$$\frac{A_{fi}}{B_{fi}} = \frac{8 \pi h \nu^3}{c^3 / n_o^3}, \quad (26)$$

and

$$\frac{B_{if}}{B_{fi}} = \frac{g_f}{g_i}, \quad (27)$$

where n_o is the index of refraction of crystal, and g_i and g_f are the statistical weights (degeneracy) of state i and f , respectively. Then

$$\frac{f_{fi}}{f_{if}} = \frac{g_i}{g_f}. \quad (28)$$

As the radiation propagates in the absorbing medium, the flux gradually decreases:

$$-\frac{d\rho_\nu}{dt} = N_i W_{if} h\nu g(\nu) - N_f W_{fi} h\nu g(\nu), \quad (29)$$

where ρ_ν is the energy density of beam per unit frequency per unit solid angle (erg sec cm^{-3}), W_{fi} and W_{if} are the probabilities for induced emission and absorption per unit time, $g(\nu)$ is the normalized line shape of transition (sec), N_i and N_f are the densities of absorbing centers in i and f states, and t is the time (sec). Since $W_{fi} = B_{fi} \rho_\nu$,

$W_{if} = B_{if} \rho_\nu$, $\nu = \frac{dx}{dt}$ and $E = h\nu = 2\pi\hbar\nu$, Equation (29) may be written as

$$-d\rho_E = \frac{E}{\nu} \left(\frac{g_f}{g_i} n_i - n_f \right) B_{fi} \rho_E g(E) dx, \quad (30)$$

where x is the light path length in the absorbing medium. Let N_i^0 and N_f^0 the densities of absorbing centers in i and f states in absence of

radiation and assume that the absorption is independent of the intensity of the beam (this is the basic assumption of linear optics), then

$B_{if} \rho_E \ll 1$ and

$$N_i - \frac{g_i}{g_f} N_f \approx N_i^0 - \frac{g_i}{g_f} N_f^0. \quad (31)$$

Finally Equation (30) can be written

$$-\frac{1}{\rho_E} \frac{d\rho_E}{dx} = \frac{E}{v} B_{if} \left(N_i^0 - \frac{g_i}{g_f} N_f^0 \right) g(E). \quad (32)$$

From this equation we have

$$\rho_E(x) = \rho_E(0) e^{-\alpha(E)x} \quad (\text{Beer's law})^{(74)}, \quad (33)$$

where

$$\alpha(E) = \frac{E}{v} (B_{if} N_i - B_{fi} N_f) g(E) = \frac{\lambda^2}{8\pi\tau_0} \frac{g_f}{g_i} \left(N_i^0 - \frac{g_i}{g_f} N_f^0 \right) g(E) \quad (34)$$

and $\rho_E(0)$ is the energy density after a path length $x = 0$. We call $\alpha(E)$ the absorption coefficient, and Equation (33) indicates that the intensity of a beam of radiation which passes through an absorbing medium decreases exponentially. By integrating Equation (34) over band-width, we have

$$\int \alpha(E) dE = \frac{\lambda^2}{4\tau_0} \frac{g_f}{g_i} N_i^0 \left(1 - \frac{g_i}{g_f} \frac{N_f^0}{N_i^0} \right). \quad (35)$$

Furthermore, for low intensity beams, $n_f \ll n_i$, then

$$\int \alpha(E) dE \approx \frac{\lambda^2}{4} \frac{\hbar}{g_f} \frac{g_i}{\tau_o} \frac{N_i^o}{N_1^o} . \quad (36)$$

This is the fundamental formula of absorption spectroscopy. It must be emphasized that $\int \alpha(E) dE$ is quite different from the $\alpha(E)$ in Beer's law, Equation (33), and does not unambiguously determine the rate of attenuation of the beam intensity of radiation in the medium.

The absorption cross section of a transition is defined by

$$\sigma(E) = \frac{\alpha(E)}{N_1} . \quad (37)$$

Using Equation (36)

$$\int \sigma(E) dE = \frac{\lambda^2}{4} \frac{g_f}{g_i} \frac{\hbar}{\tau_o} . \quad (38)$$

To treat the optical absorption of ions in crystal, Equation (20) must be modified since electric dipole transition probability is proportional to the square of the electric field at the ion site. This equation must be multiplied by $(\epsilon_{\text{eff}}/\epsilon)^2$, where ϵ_{eff} is the electric field at the ion site and ϵ is the field in the vacuum. It should be remembered that

$$k = \frac{\omega}{v} = \frac{n_o \omega}{c} , \quad (39)$$

where n_o is the index of refraction. In addition, an extra factor n_o^3 has to be included in the Equation (20), because the density of final states is proportional to $k^2 dk$ and by introducing the dielectric constant $= n_o^2$, we have

$$\frac{\epsilon_{eff}}{\epsilon} = \frac{1}{n_o} \frac{\epsilon_{eff}}{\epsilon_o}, \quad (40)$$

where ϵ_o is the average electric field in the crystal. Finally Equation (20) may be written as:

$$A_{fi}^{El} = \frac{8\pi\omega^3}{3nc^3} |M|^2 \left(\frac{\epsilon_{eff}}{\epsilon_o}\right)^2 n_o, \quad (41)$$

and

$$A_{fi}^{Ml} = \frac{8\pi\omega^3}{3nc^3} |M|^2 n_o^3. \quad (42)$$

Moreover, Equation (22) becomes,

$$f_{fi}^{El} \tau_o = 1.51 \left(\frac{\epsilon_o}{\epsilon_{eff}}\right)^2 \frac{\lambda_o^2}{n_o}, \quad (43)$$

and

$$f_{fi}^{Ml} \tau_o = 1.51 \frac{\lambda_o^2}{n_o}, \quad (44)$$

where λ_o is the wavelength of the radiation in the vacuum. Considering the above argument, we can write Equation (38) for electric dipole transition as

$$\begin{aligned} \int \sigma(E) dE &= \frac{2\hbar\pi^2 e^2}{mc} \frac{g_f}{g_i} \left(\frac{\epsilon_{eff}}{\epsilon_o}\right)^2 \frac{1}{n_o} f_{fi}^{El} \\ &= \frac{2\hbar\pi^2 e^2}{mc} \left(\frac{\epsilon_{eff}}{\epsilon_o}\right)^2 \frac{1}{n_o} f_{if}^{El} \end{aligned} \quad (45)$$

For the magnetic dipole transition, Equation (38) becomes

$$\int \sigma(E) dE = \frac{2\pi^2 e^2}{mc} \frac{g_f}{g_i} n_o f_{fi}^{M1} = \frac{2\pi^2 e^2}{mc} n_o f_{if}^{M1}. \quad (46)$$

From Equation (37), we have

$$\int \sigma(E) dE = \frac{1}{N_1} \int \alpha(E) dE, \quad (47)$$

and thus Equation (45) can be written in the form

$$N_1 f_{if}^{E1} = \frac{n_o mc}{2\pi^2 \hbar e^2} \left(\frac{\epsilon_o}{\epsilon_{eff}} \right)^2 \int \alpha(E) dE. \quad (48)$$

This is the Smakula's equation⁽⁷⁵⁾. Dexter^(70,76) suggested that the Lorentz local field expression for the effective electric field in the crystal could be written,

$$\frac{\epsilon_{eff}}{\epsilon_o} \approx 1 + \frac{n_o^2 - 1}{3} \quad (49)$$

and from this, Equation (48) may be rewritten as

$$N_1 f_{if}^{E1} = \frac{n_o mc}{2\pi^2 \hbar e^2} \frac{9}{(n_o^2 + 2)^2} \int \alpha(E) dE = 8.21 \times 10^{16} \frac{n_o}{(n_o^2 + 2)^2} \int \alpha(E) dE, \quad (50)$$

where α is in reciprocal centimeters and E in electron volts.

If the shape of the absorption curve is of the classical Lorentzian form,

$$\int \alpha(E) dE = \frac{1}{2} \pi \alpha_{max} W_{1/2}, \quad (51)$$

where $W_{1/2}$ is the full width at half-maximum and α_{max} is the maximum ab-

sorption coefficient, then

$$N_i f_{if}^{E1} = 1.29 \times 10^{17} \frac{n_o}{(n_o^2 + 2)^2} \alpha_{\max} W_{1/2}. \quad (52)$$

For absorption bands which are Gaussian in shape,

$$\int \alpha(E) dE = \frac{1}{2} \left(\frac{\pi}{\ln 2} \right)^{1/2} \alpha_{\max} W_{1/2}, \quad (53)$$

and

$$N_i f_{if}^{E1} = 0.87 \times 10^{17} \frac{n_o}{(n_o^2 + 2)^2} \alpha_{\max} W_{1/2}. \quad (54)$$

Similarly, for the magnetic dipole transition, we also have

$$\frac{1}{N_i} \int \alpha(\nu) d\nu = \frac{\pi e^2}{mc} n_o f_{if}^{M1} \quad (55)$$

and then

$$N_i f_{if}^{M1} = \frac{mc}{\pi e^2 n_o} \frac{1}{2\pi h} \int \alpha(E) dE = 9.11 \times 10^{15} \frac{1}{n_o} \int \alpha(E) dE. \quad (56)$$

For bands with Lorentzian shape, we have

$$N_i f_{if}^{M1} = 1.43 \times 10^{16} \frac{1}{n_o} \alpha_{\max} W_{1/2}, \quad (57)$$

and for Gaussian bands,

$$N_i f_{if}^{M1} = 0.967 \times 10^{16} \frac{1}{n_o} \alpha_{\max} W_{1/2}. \quad (58)$$

If the concentration, the index of refraction, and the optical absorption are measured, the oscillator strength can be calculated from these equations.

Polarized Bleaching

Although the theoretical calculations for polarized absorption and emission by oriented defects have been published in the past^(9,34,77) in the interest of clarity and especially since sample orientation plays a major role in the calculations, we will briefly review these calculations as they apply to our experimental situation. Figure 2 is a schematic of the sample orientation, with respect to both the exciting light and the detection system, and of the orientation of different types of defects in a cubic lattice. The major electric dipole axis is designated σ , the dipole axis perpendicular to σ but in the same $\{100\}$ plane is shown as π_1 , and the dipole axis perpendicular to both of these directions is labeled π_2 . For the case of absorption when incident light is polarized along a direction \hat{u} the interaction of this light with the various defect configurations \hat{r}_i^β , where β is either the major electric dipole axis σ or one of the minor electric dipole axes π_1 or π_2 , results in an absorption coefficient given by⁽⁹⁾

$$\alpha_{\hat{u}} = \bar{\sigma} \sum_i n_i |\hat{u} \cdot \hat{r}_i^\sigma|^2 + \bar{\pi}_1 \sum_i n_i |\hat{u} \cdot \hat{r}_i^{\pi_1}|^2 + \bar{\pi}_2 \sum_i n_i |\hat{u} \cdot \hat{r}_i^{\pi_2}|^2. \quad (59)$$

Here $\bar{\sigma}$, $\bar{\pi}_1$, and $\bar{\pi}_2$ are factors unique to the dipole axes and contain several constants⁽²⁷⁾, n_i is the number of centers whose major axis lies along one of the orientations shown in Figure 2. The results of this type of calculation are shown in Table I for light propagating along the

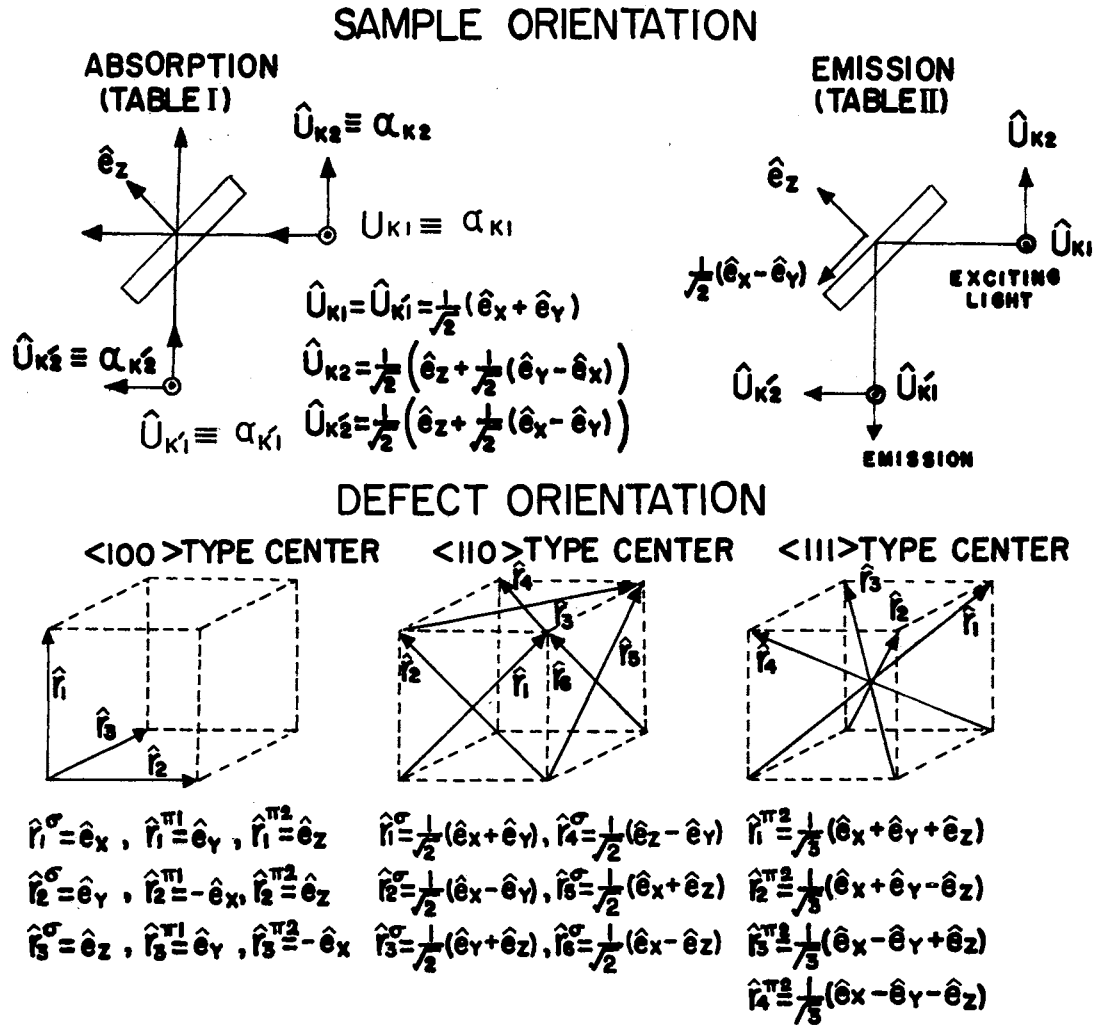


Figure 2. Schematic Illustrations of the Sample Orientation With Respect to Both the Incident Light and the Detection Systems for Absorption and Emission and of Defect Orientations in Cubic Crystals

TABLE I

ABSORPTION COEFFICIENT FOR LINEARLY POLARIZED LIGHT AS A FUNCTION OF THE TYPE OF CENTER

Absorption coefficient	$\langle 110 \rangle$ -type center	$\langle 111 \rangle$ -type center
$\alpha_{K1}(\epsilon) = \alpha_{K'1}(\epsilon)$	$\sigma(\epsilon)[n_1 + \frac{1}{4}(n_3 + n_4 + n_5 + n_6)]$ $+ \pi_1(\epsilon)[n_2 + \frac{1}{4}(n_3 + n_4 + n_5 + n_6)]$ $+ \pi_2(\epsilon)[\frac{1}{2}(n_3 + n_4 + n_5 + n_6)]$	$\sigma(\epsilon)[\frac{1}{6}(n_1 + n_2) + \frac{1}{2}(n_3 + n_4)]$ $+ \pi_1(\epsilon)[\frac{1}{6}(n_1 + n_2) + \frac{1}{2}(n_3 + n_4)]$ $+ \frac{2}{3}\pi_2(\epsilon)(n_1 + n_2)$
$\alpha_{K2}(\epsilon)$	$\sigma(\epsilon)[\frac{1}{2}n_2 + \frac{1}{8}\delta(n_3 + n_6) + \frac{1}{8}\gamma(n_4 + n_5)]$ $+ \pi_1(\epsilon)[\frac{1}{2}n_1 + \frac{1}{8}\gamma(n_3 + n_6) + \frac{1}{8}\delta(n_4 + n_5)]$ $+ \pi_2(\epsilon)[\frac{1}{2}(n_1 + n_2) + \frac{1}{4}(n_3 + n_4 + n_5 + n_6)]$	$\frac{1}{12}\sigma(\epsilon)(5n_1 + 5n_2 + \delta n_3 + \gamma n_4)$ $+ \frac{1}{12}\pi_1(\epsilon)(5n_1 + 5n_2 + \delta n_3 + \gamma n_4)$ $+ \frac{1}{6}\pi_2(\epsilon)(n_1 + n_2 + \gamma n_3 + \delta n_4)$
$\alpha_{K'2}(\epsilon)$	$\sigma(\epsilon)[\frac{1}{2}n_2 + \frac{1}{8}\gamma(n_3 + n_6) + \frac{1}{8}\delta(n_4 + n_5)]$ $+ \pi_1(\epsilon)[\frac{1}{2}n_1 + \frac{1}{8}\delta(n_3 + n_6) + \frac{1}{8}\gamma(n_4 + n_5)]$ $+ \pi_2(\epsilon)[\frac{1}{2}(n_1 + n_2) + \frac{1}{4}(n_3 + n_4 + n_5 + n_6)]$	$\frac{1}{12}\sigma(\epsilon)(5n_1 + 5n_2 + \gamma n_3 + \delta n_4)$ $+ \frac{1}{12}\pi_1(\epsilon)(5n_1 + 5n_2 + \gamma n_3 + \delta n_4)$ $+ \frac{1}{6}\pi_2(\epsilon)(n_1 + n_2 + \delta n_3 + \gamma n_4)$
$\alpha_{110}(\epsilon)$	$\sigma(\epsilon)[n_1 + \frac{1}{4}(n_3 + n_4 + n_5 + n_6)]$ $+ \pi_1(\epsilon)[n_2 + \frac{1}{4}(n_3 + n_4 + n_5 + n_6)]$ $+ \frac{1}{2}\pi_2(\epsilon)[n_3 + n_4 + n_5 + n_6]$	$\frac{1}{6}\sigma(\epsilon)(n_1 + n_2 + 3n_3 + 3n_4)$ $+ \frac{1}{6}\pi_1(\epsilon)(n_1 + n_2 + 3n_3 + 3n_4)$ $+ \frac{2}{3}\pi_2(\epsilon)(n_1 + n_2)$
$\alpha_{110}^-(\epsilon)$	$\sigma(\epsilon)[n_2 + \frac{1}{4}(n_3 + n_4 + n_5 + n_6)]$ $+ \pi_1(\epsilon)[n_1 + \frac{1}{4}(n_3 + n_4 + n_5 + n_6)]$ $+ \frac{1}{2}\pi_2(\epsilon)[n_3 + n_4 + n_5 + n_6]$	$\frac{1}{6}\sigma(\epsilon)(3n_1 + 3n_2 + n_3 + n_4)$ $+ \frac{1}{6}\pi_1(\epsilon)(3n_1 + 3n_2 + n_3 + n_4)$ $+ \frac{2}{3}\pi_2(\epsilon)(n_3 + n_4)$

\hat{U}_{k2} , $\hat{U}_{k'2}$, and $[001]$ directions. The notation α_{k2} denotes the absorption coefficient for light polarized along the \hat{U}_{k2} direction. The square of the direction cosine between light propagating in $\hat{U}_{k'2}$ direction and polarized along the direction \hat{U}_{k2} and \hat{r}_3^β and \hat{r}_6^β is denoted as $\frac{1}{8} \delta$; and $\frac{1}{8} \gamma$ is the square of the direction cosine between \hat{U}_{k2} and \hat{r}_4^β and \hat{r}_5^β . For the sample orientation used in this experiment, i.e., 45° to the incident beam, $\delta = (\sqrt{2} + 1)^2$ and $\gamma = (\sqrt{2} - 1)^2$. When the direction of the propagation is perpendicular to the sample face, the equation is much simplified as can be seen from the expression for α_{110} . The optical anisotropy is defined as:

$$A_{100} = \alpha_{100} - \alpha_{010} = -A_{010},$$

and

(60)

$$A_{110} = \alpha_{110} - \alpha_{1\bar{1}0} = -A_{1\bar{1}0}.$$

Now we will compare the relative intensities of the polarized emission from $\langle 110 \rangle$ - and $\langle 111 \rangle$ -type centers. The emission may be written in the form

$$I_{j\ell} = \rho \sum_i n_i |\hat{r}_i^{\beta_1} \cdot \hat{U}_{k'j}|^2 |\hat{r}_i^{\beta_2} \cdot \hat{U}_{k\ell}|^2, \quad (61)$$

where ρ is a constant and j and ℓ denote the polarization of the excitation and emission respectively, e.g., $j, \ell = 1, 2$ and $\hat{U}_{k\ell}$ and $\hat{U}_{k'j}$ are the polarization vectors shown in Figure 2 for emission. Note that the emission is not required to be from the same state involved in absorption and the cases $\beta_1, \beta_2 = \sigma, \pi_1; \pi_2$ have also been considered. The computed intensities are shown in Table II. The second row in each case

TABLE II
RELATIVE INTENSITIES FOR POLARIZED EMISSION

Type of Center	$\alpha \beta$	I_{11}	I_{12}	I_{21}	I_{22}
<100>	$\sigma-\sigma$	$\frac{1}{4}\rho[n_1 + n_2]$ $\frac{1}{2}\rho \bar{n}$	$\frac{1}{8}\rho[n_1 + n_2]$ $\frac{1}{4}\rho \bar{n}$	$\frac{1}{8}\rho[n_1 + n_2]$ $\frac{1}{4}\rho \bar{n}$	$\frac{1}{16}\rho[n_1 + n_2 + 4n_3]$ $\frac{3}{8}\rho \bar{n}$
	$\sigma-\pi$	$\frac{1}{8}\rho[n_1 + n_2]$ $\frac{1}{4}\rho \bar{n}$	$\frac{3}{16}\rho[n_1 + n_2]$ $\frac{3}{8}\rho \bar{n}$	$\frac{1}{16}\rho[n_1 + n_2 + 4n_2]$ $\frac{3}{8}\rho \bar{n}$	$\frac{1}{32}\rho[3n_1 + 3n_2 + 4n_3]$ $\frac{5}{16}\rho \bar{n}$
	$\pi-\sigma$	$\frac{1}{8}\rho[n_1 + n_2]$ $\frac{1}{4}\rho \bar{n}$	$\frac{1}{16}\rho[n_1 + n_2 + 4n_2]$ $\frac{3}{8}\rho \bar{n}$	$\frac{3}{16}\rho[n_1 + n_2]$ $\frac{3}{8}\rho \bar{n}$	$\frac{1}{32}\rho[3n_1 + 3n_2 + 4n_3]$ $\frac{5}{16}\rho \bar{n}$
	$\pi-\pi$	$\frac{1}{16}\rho[n_1 + n_2 + 4n_3]$ $\frac{3}{8}\rho \bar{n}$	$\frac{1}{32}\rho[3n_1 + 3n_2 + 4n_3]$ $\frac{5}{16}\rho \bar{n}$	$\frac{1}{32}\rho[3n_1 + 3n_2 + 4n_3]$ $\frac{5}{16}\rho \bar{n}$	$\frac{1}{64}\rho[9n_1 + 9n_2 + 4n_3]$ $\frac{11}{32}\rho \bar{n}$
<110>	$\sigma-\sigma$	$\frac{1}{16}\rho[16n_1 + n_3 + n_4 + n_5 + n_6]$ $\frac{5}{4}\rho \bar{n}$	$\frac{1}{32}\rho[\gamma(n_3 + n_6) + \delta(n_4 + n_5)]$ $\frac{3}{8}\rho \bar{n}$	$\frac{1}{32}\rho[\delta(n_3 + n_6) + \gamma(n_4 + n_5)]$ $\frac{3}{8}\rho \bar{n}$	$\frac{1}{64}\rho[16n_2 + n_3 + n_4 + n_5 + n_6]$ $\frac{5}{16}\rho \bar{n}$
	$\sigma-\pi_1$	$\frac{1}{16}\rho[n_3 + n_4 + n_5 + n_6]$ $\frac{1}{4}\rho \bar{n}$	$\frac{1}{32}\rho[16n_1 + \delta(n_3 + n_6) + \gamma(n_4 + n_5)]$ $\frac{7}{8}\rho \bar{n}$	$\frac{1}{32}\rho[16n_2 + \delta(n_3 + n_6) + \gamma(n_4 + n_5)]$ $\frac{7}{8}\rho \bar{n}$	$\frac{1}{64}\rho[\delta^2(n_3 + n_6) + \gamma^2(n_4 + n_5)]$ $\frac{17}{16}\rho \bar{n}$
	$\sigma-\pi_2$	$\frac{1}{8}\rho[n_3 + n_4 + n_5 + n_6]$ $\frac{1}{2}\rho \bar{n}$	$\frac{1}{16}\rho[8n_1 + n_3 + n_4 + n_5 + n_6]$ $\frac{3}{4}\rho \bar{n}$	$\frac{1}{16}\rho[\delta(n_3 + n_6) + \delta(n_4 + n_5)]$ $\frac{3}{4}\rho \bar{n}$	$\frac{1}{32}\rho[8n_2 + \delta(n_3 + n_6) + \gamma(n_4 + n_5)]$ $\frac{5}{8}\rho \bar{n}$
<111>	$\pi_1-\sigma$	$\frac{1}{36}\rho[n_1 + n_2 + 9n_3 + 9n_4]$ $\frac{5}{9}\rho \bar{n}$	$\frac{1}{72}\rho[5n_1 + 5n_2 + 3\gamma n_3 + 3\delta n_4]$ $\frac{7}{18}\rho \bar{n}$	$\frac{1}{72}\rho[5n_1 + 5n_2 + 3\delta n_3 + 3\gamma n_4]$ $\frac{7}{18}\rho \bar{n}$	$\frac{1}{144}\rho[25n_1 + 25n_2 + n_3 + n_4]$ $\frac{13}{36}\rho \bar{n}$
	$\sigma-\pi_2$	$\frac{1}{9}\rho[n_1 + n_2]$ $\frac{2}{9}\rho \bar{n}$	$\frac{1}{36}\rho[n_1 + n_2 + 3\delta n_3 + 3\gamma n_4]$ $\frac{5}{9}\rho \bar{n}$	$\frac{5}{18}\rho[n_1 + n_2]$ $\frac{5}{9}\rho \bar{n}$	$\frac{1}{72}\rho[5n_1 + 5n_2 + \delta^2 n_3 + \gamma^2 n_4]$ $\frac{11}{18}\rho \bar{n}$
	$\pi_2-\sigma$	$\frac{1}{9}\rho[n_1 + n_2]$ $\frac{2}{9}\rho \bar{n}$	$\frac{1}{18}\rho[5n_1 + 5n_2]$ $\frac{5}{9}\rho \bar{n}$	$\frac{1}{36}\rho[n_1 + n_2 + 3\gamma n_3 + 3\delta n_4]$ $\frac{5}{9}\rho \bar{n}$	$\frac{1}{72}\rho[5n_1 + 5n_2 + \gamma^2 n_3 + \delta^2 n_4]$ $\frac{11}{18}\rho \bar{n}$
	$\pi_2-\pi_1$	$\frac{4}{9}\rho[n_1 + n_2]$ $\frac{8}{9}\rho \bar{n}$	$\frac{1}{9}\rho[n_1 + n_2]$ $\frac{2}{9}\rho \bar{n}$	$\frac{1}{9}\rho[n_1 + n_2]$ $\frac{2}{9}\rho \bar{n}$	$\frac{1}{36}\rho[n_1 + n_2 + n_3 + n_4]$ $\frac{1}{9}\rho \bar{n}$
	$\pi_2-\pi_2$	$\frac{4}{9}\rho[n_1 + n_2]$ $\frac{8}{9}\rho \bar{n}$	$\frac{1}{9}\rho[n_1 + n_2]$ $\frac{2}{9}\rho \bar{n}$	$\frac{1}{9}\rho[n_1 + n_2]$ $\frac{2}{9}\rho \bar{n}$	$\frac{1}{36}\rho[n_1 + n_2 + n_3 + n_4]$ $\frac{1}{9}\rho \bar{n}$
	$\pi_2-\pi_2$	$\frac{4}{9}\rho[n_1 + n_2]$ $\frac{8}{9}\rho \bar{n}$	$\frac{1}{9}\rho[n_1 + n_2]$ $\frac{2}{9}\rho \bar{n}$	$\frac{1}{9}\rho[n_1 + n_2]$ $\frac{2}{9}\rho \bar{n}$	$\frac{1}{36}\rho[n_1 + n_2 + n_3 + n_4]$ $\frac{1}{9}\rho \bar{n}$

gives the value for a random distribution of centers. the absorption coefficients for the directions connected with these measurements are also given in Table I. When both polarized emission and absorption data are available, an intercomparison of the two sets of data allows a determination of the defect population of the various orientations shown in Figure 2.

Vibrational-Electronic Interaction

The optical transitions from defects in crystals sometimes have strongly temperature dependent absorption or emission spectra whose frequencies do not correspond to any transition in the energy level scheme. These transitions involve two simultaneous events. One is a change in electronic state and the other is a change in the excitation state of a vibrational lattice mode. The bands due to these transitions are called vibrational side bands. Absorption or emission of a photon with absorption or emission of a phonon results in vibrational side bands to the blue or red of the zero-phonon line in absorption and emission band. These transitions are called vibrational-electronic or vibronic. The vibrational frequencies which affect the spectra of an optically active center are due to the modulating effects of ligand motion. The state function of the total system is given by

$$|\psi\rangle = |\psi^{el}; n_1, n_2, \dots, n_q, \dots; n_1, n_2, \dots, n_k, \dots\rangle, \quad (62)$$

where n_q 's are the phonon occupation numbers and n_k 's are the photon occupation numbers. If we employ Born-Oppenheimer approximation⁽⁷⁰⁾ which separates the nuclear and electronic coordinate systems, then

$$|\Psi\rangle = |\Psi^{el}\rangle |n_1, n_2, \dots, n_q, \dots\rangle |n_1, n_2, \dots, n_k, \dots\rangle. \quad (63)$$

The Hamiltonian for a system which consists of a central ion, the molecular vibration of the molecular complex and the radiation field is given by⁽⁶⁵⁾

$$H = H_{ion} + H_{vib} + H_{rad} + H_{int}. \quad (64)$$

Where

$$H_{ion} = H_o \text{ (free ion)} + H_{cryst.} + H_{S.O.}, \quad (65)$$

$$H_{vib} = \sum_q \hbar \omega_q (b_q^+ b_q + \frac{1}{2}), \quad (66)$$

$$H_{rad} = \sum_{k,\lambda} \hbar \omega_k (a_k^{\lambda+} a_k^\lambda + \frac{1}{2}), \quad (67)$$

and $H_{int} = H_{int}^{EL} + H_{int}^{ER}$, b_q^+ and b_q are the creation and annihilation operators for phonon, H_{int}^{EL} is the Hamiltonian for electron and lattice interaction and H_{int}^{ER} is the Hamiltonian for electron and radiation interaction. H_{int}^{ER} is the same as H_{int} in Equation (6).

If the nucleus of the central ion is taken as origin for the coordinate axes, then the crystalline potential can be expressed in terms of the normal displacements of the molecule as:

$$V_{cryst.} = V_o + \sum_q \frac{\partial V}{\partial Q_q} \Big|_o Q_q + \frac{1}{2!} \sum_{q,q'} \frac{\partial^2 V}{\partial Q_q \partial Q_{q'}} \Big|_o Q_q Q_{q'} + \dots, \quad (68)$$

where each normal coordinate Q_q is a linear combination of the displacements of the ions. V_o is the static perturbation that produces the crystal field, i.e., $V_o = H_{cryst.}$. If we choose the first order approxi-

mation, then

$$H_{int}^{EL} \approx \sum_q V_q Q_q = \sum_q V_q \left(\frac{\hbar}{2\omega_q} \right)^{1/2} (b_q + b_q^+), \quad (69)$$

where $V_q = \left. \frac{\partial V}{\partial Q_q} \right|_0$ is a function of the coordinate of the central ion.

The matrix element for the creation of a photon of mode k with polarization $\hat{\pi}_k^\lambda$ and of a phonon of mode q is

$$|M(n_q+1; n_k+1)| = \sum_j \frac{\langle \psi_f^{el}; n_q+1; n_k+1 | H_{int}^{EL} + H_{int}^{ER} | \psi_j \rangle \langle \psi_j | H_{int}^{EL} + H_{int}^{ER} | \psi_i^{el}; n_q; n_k \rangle}{E_i - E_j} \quad (70)$$

From the orthogonality condition,

$$\begin{aligned} & |M(n_q+1; n_k+1)| \\ &= \sum_j \frac{\langle \psi_f^{el}; n_q+1; n_k+1 | H_{int}^{ER} | \psi_j^{el}; n_q+1; n_k \rangle \langle \psi_j^{el}; n_q+1; n_k | H_{int}^{EL} | \psi_i^{el}; n_q; n_k \rangle}{E_i^{el} - (E_j^{el} + \hbar\omega_q)} \\ &+ \sum_i \frac{\langle \psi_f^{el}; n_q+1; n_k+1 | H_{int}^{EL} | \psi_j^{el}; n_q; n_k+1 \rangle \langle \psi_j^{el}; n_q; n_k+1 | H_{int}^{ER} | \psi_i^{el}; n_q; n_k \rangle}{E_i^{el} - (E_j^{el} + \hbar\omega_k)} \\ &= \sum_j \left[\frac{\langle \psi_f^{el}; n_k+1 | H_{int}^{ER} | \psi_j^{el}; n_k \rangle \langle \psi_j^{el} | \Gamma_v | \psi_i^{el} \rangle (n_q+1)^{1/2}}{E_i^{el} - (E_j^{el} + \hbar\omega_q)} \right. \\ &\quad \left. + \frac{\langle \psi_f^{el} | \Gamma_v | \psi_j^{el} \rangle \langle \psi_j^{el}; n_k+1 | H_{int}^{ER} | \psi_i^{el}; n_k \rangle (n_q+1)^{1/2}}{E_i^{el} - (E_j^{el} + \hbar\omega_k)} \right] \left(\frac{\hbar}{2\omega_q} \right)^{1/2}, \end{aligned}$$

then

$$|M(n_q+1, n_k+1)|$$

$$= \frac{e}{m} \left(\frac{\hbar}{2\omega_q} \right)^{1/2} \left(\frac{2\pi\hbar}{\omega_k V} \right)^{1/2} \left\{ \frac{n_k+1}{n_k} \right\}^{1/2} (n_q+1)^{1/2} \left[\sum_j \frac{\langle \psi_f^{el} | \sum_i e^{-i\vec{k} \cdot \vec{r}_i} \vec{p} \cdot \hat{\pi}_k^\lambda | \psi_j^{el} \rangle \langle \psi_j^{el} | \Gamma_v | \psi_i^{el} \rangle}{E_i^{el} - (E_j^{el} + \hbar\omega_q)} \right], \quad (71)$$

where Γ_v represents one of the possible modes of vibration of complex, and j run for all electrons in ion. The second term in [] is neglected because $\omega_k \gg \omega_q$. The upper matrix element represents the process of the creation of a photon plus creation of a phonon (emission in the low energy band) whereas the lower matrix element represents the absorption of a photon and a creation of a phonon (absorption in high energy band). Similarly the matrix elements involved in the absorption of a phonon are

$$|M(n_q-1; n_k \pm 1)|$$

$$= \frac{e}{m} \left(\frac{\hbar}{2\omega_q} \right)^{1/2} \left(\frac{2\pi\hbar}{\omega_k V} \right)^{1/2} \left[\sum_j \frac{\langle \psi_f^{el} | \sum_i e^{-i\vec{k} \cdot \vec{r}_i} \vec{p} \cdot \hat{\pi}_k^\lambda | \psi_j^{el} \rangle \langle \psi_j^{el} | \Gamma_v | \psi_i^{el} \rangle}{E_i^{el} - (E_j^{el} - \hbar\omega_q)} \right]$$

$$\cdot \left\{ \frac{n_k+1}{n_k} \right\}^{1/2} (n_q)^{1/2}. \quad (72)$$

The upper matrix element represents the process of the creation of a photon and absorption of a phonon (emission in the high energy band) whereas the lower matrix element represents the absorption of a photon and absorption of a phonon (absorption in the low energy band). Since

$$n_q = \frac{1}{e^{\hbar\omega_q/kT} - 1}, \text{ then } n_q = 0 \text{ at } T = 0, \text{ and so the second process is}$$

not active at low temperature.

Configuration Coordinate Model for the Optical Band Shape

The configuration coordinate scheme suggested^(9,11,65,78-81) by the results of the Born-Oppenheimer approximation can be used as a model to explain the optical band shape. In the linear coupling model, two non-degenerate electronic states, ψ_i and ψ_f are assumed to couple linearly to a normal coordinate Q of the lattice. In the Born-Oppenheimer approximation the nuclear motion problem is reduced to that of solving for the vibrational states for the adiabatic potentials approximation to the ground and excited electronic states. These potentials are

$$E_i(Q) = \frac{1}{2} m\omega^2 Q^2$$

and

$$E_f(Q) = E_{if} + A\hbar\omega \left(\frac{m\omega}{\hbar}\right)^{1/2} Q + \frac{1}{2} m\omega^2 Q^2. \quad (73)$$

Here Q is the normal coordinate and A is a dimensionless constant which characterizes the strength of the linear interaction. The energy separation between the excited state and ground state potential at $Q=0$ is E_{if} . The quantum mechanical solutions for the ground states are

$$|n_\alpha\rangle_i = |\dots n_\alpha \dots\rangle_i = \left[\frac{(m\omega/\hbar)^{1/2}}{\pi^{1/2} 2^\alpha \alpha!} \right]^{1/2} e^{-\frac{1}{2}\rho^2} H_\alpha(\rho), \quad (74)$$

where $\rho = \left(\frac{m\omega}{\hbar}\right)^{1/2} Q$ and $H_\alpha(\rho)$ is a Hermite polynomial. The possible ground state energies are

$$\epsilon_{i\alpha} = (\alpha + \frac{1}{2}) \hbar\omega. \quad (75)$$

The solutions for the excited state are

$$|n_\beta\rangle_f = |\cdots n_\beta \cdots\rangle_f = \left[\frac{(\hbar\omega/\hbar)^{\frac{1}{2}}}{\pi^{\frac{1}{2}} 2^\beta \beta!} \right]^{\frac{1}{2}} e^{-\frac{1}{2}(\rho+A)^2} H_\beta(\rho+A), \quad (76)$$

with energies

$$\epsilon_{f\beta} = (\beta + \frac{1}{2})\hbar\omega + \epsilon_{if} - \frac{A^2}{2} \hbar\omega. \quad (77)$$

The ground and excited state "vibronic" wave function for the coupled defects are taken to be product function of the form $\psi_g^{el}(\vec{r}, \vec{Q}) |\cdots n_\alpha \cdots\rangle_i$ and $\psi_i^{el}(\vec{r}, \vec{Q}) |\cdots n_\beta \cdots\rangle_f$, where \vec{r} is the electronic coordinate. By employing the usual Frank-Condon approximation, the matrix element can be written as $\langle \psi_e^{el} | \vec{M} | \psi_g^{el} \rangle_f \langle \cdots n_\beta \cdots | \cdots n_\alpha \cdots \rangle_i$. Thus, the optical band shape is determined by the overlap integral, $\langle \cdots n_\alpha \cdots | \cdots n_\beta \cdots \rangle_i$. The probability for the transition can be expressed as a normalized Gaussian and the full width at half-maximum is

$$W_{\frac{1}{2}}(T) = W_{\frac{1}{2}}(0) \left(\coth \frac{\hbar\omega}{2kT} \right)^{\frac{1}{2}}. \quad (78)$$

The overlap integral between displaced harmonic oscillator wave functions is ⁽⁸¹⁾

$$\langle \cdots n_\beta \cdots | \cdots n_\alpha \cdots \rangle_i = e^{-A^2/4} \left(\frac{\alpha!}{\beta!} \right)^{\frac{1}{2}} \left(\frac{A^2}{2} \right)^{\frac{1}{2}(\beta-\alpha)} L_\alpha^{\beta-\alpha} (A^2/2), \quad (79)$$

where $L_\alpha^{\beta-\alpha}$ is the Laguerre polynomial. If $S = A^2/2$ then the normalized transition probability is

$$W_{\beta\alpha} = e^{-S} \left(\frac{\alpha!}{\beta!} \right) S^{\beta-\alpha} [L_{\alpha}^{\beta-\alpha}(S)]^2, \quad (80)$$

where S is Huang-Rhys factor⁽⁸²⁾. For $T = 0^\circ\text{K}$, the only occupied initial level is $\alpha = 0$, and $L_0^\beta(S) = 1$, and the probability for the transition to the β th level of the excited state is

$$W_{\beta 0} = \frac{S^\beta}{\beta!} e^{-S}. \quad (81)$$

This leads to an absorption spectrum consisting of a series of lines at

$$E_\beta = (E_{if} - S\hbar\omega) + \beta\hbar\omega = E_0 + \beta\hbar\omega. \quad (82a)$$

From this we know that the zero-phonon transition at E_0 has the normalized probability $W_{00} = e^{-S}$. The same is true for the emission band. At low temperature an emission spectrum consisting of a series of lines at

$$E_\alpha = E_0 + \alpha\hbar\omega, \quad (82b)$$

is mirrored about the zero-phonon line. If $S = 0$, the spectrum is a single unbroadened line at the static lattice position E_{if} . For $S > 0$, the zero-phonon line is displaced from the static lattice position by the amount $S\hbar\omega$.

If the individual components of the line series are not resolved, it is convenient to describe the line shape by its moments. In those cases where only the envelope is observed for a line series with large values of S , the second moment is related to the $W_{1/2}(0)$ by

$$W_{1/2}(0) \approx 8 \ln 2 [M_2(0)]^{1/2}, \quad (83)$$

where $M_2(0)$ is the second moment and is $S(\hbar\omega)^2$ at $T = 0^\circ\text{K}$.

The semiclassical treatment of the configuration coordinate scheme⁽⁸⁰⁾ suggested by the results of the Born-Oppenheimer and Frank-Condon approximations will be reviewed. Under these assumptions the configuration coordinate describes a simple harmonic oscillator with force constants K_g and K_e for the ground and excited states, respectively. The minima of the two states are displaced in energy by ϵ_{ge} and in coordinate by Q_0 . This model allows for a simple description of the Stokes shift of emission and the origin of broad absorption and emission bands. At low temperature only the lowest vibrational level will be populated so that the energy of the ground state above the classical minimum will be $\epsilon_g = \frac{1}{2}\hbar\omega_g$ and the excited state has an energy $\epsilon_e = \epsilon_{ge} + \frac{1}{2}K_e(Q - Q_0)^2$.

According to the Frank-Condon principle the absorbed energy is therefore

$$\epsilon^A(Q) = (\epsilon_{ge} - \frac{\hbar\omega_g}{2} + \frac{1}{2}K_e Q_0^2) - (K_e Q_0)Q + (K_e/2)Q^2.$$

It has been customary to drop the last term in this equation since the range of values over which Q is taken is usually small. The probability of an absorption transition as a function of ϵ is given by

$$P_A(\epsilon) = (K_g/2\pi kT^*)^{\frac{1}{2}} \exp[-K_g Q^2/2kT^*] \frac{dQ}{dt},$$

where T^* , an effective temperature, given by

$$T^* = (\hbar\omega_g/2k) \coth(\hbar\omega_g/2kT).$$

Substituting for $dQ/d\epsilon$ from above equation and taking the low tempera-

ture limit, one obtains

$$P_A(\epsilon) = [K_e (Q - Q_0)]^{-1} (K_g / \pi \omega_g \hbar)^{1/2} \exp(-K_g Q^2 / \hbar \omega_g)$$

which is a normalized Gaussian with

$$\epsilon_{\max}^A = \epsilon_{ge} + \frac{1}{2} K_e Q_0^2 - \frac{1}{2} \hbar \omega_g. \quad (84a)$$

For emission, we have

$$\epsilon^E(Q) = (\epsilon_{ge} - \frac{1}{2} K_g Q_0^2 + \frac{1}{2} \hbar \omega_e) - K_g Q Q_0$$

and

$$\epsilon_{\max}^E = \epsilon_{ge} - \frac{1}{2} K_g Q_0^2 + \frac{1}{2} \hbar \omega_e. \quad (84b)$$

Where energies are in electron volts and Q_0 is in \AA . It is customary, considering the breathing mode as predominant, to take the mass to be the sum of the masses of the nearest neighbors. To describe configuration coordinate diagrams in this model, four constants ϵ_{ge} , Q_0 , K_g , and K_e are required. Therefore, a minimum of four experimental facts are needed.

Allowed Energy Terms of Mn^{2+} Ion ($3d^5$)

In 1967, Tuttle⁽⁸³⁾ developed a very simple method of finding the terms from a configuration containing a number of equivalent electrons based on two assumptions: (1) the Pauli exclusion principle, and (2) one and only one completely antisymmetric wave function can be constructed from any given set of allowed quantum numbers. The terms are repre-

sented in the form of $2S + 1_L$. The S and L are the total spin and orbital angular momentum of the system, respectively.

The following is the short outline of the steps to find the allowed energy terms of a $3d^5$ configuration:

(1) Enter values of m_ℓ in a row sequentially, from left to right, starting with $m_\ell = 1$ in column 1, according to the following rules: wherein the spin-up section (or the spin-down section) values of m_ℓ must decrease from left to right, without repeating values.

(2) For the first row of the chart, the term is simply $S = M_S$ and $L = M_L$. As chart grows larger, rows of given M_S and M_L must repeat all the preceeding terms for which $S \geq M_S$ and $L \geq M_L$. There will be at least as many rows having the given M_S and M_L as there are terms previously found with $S \geq M_S$ and $L \geq M_L$. If we have more rows than terms, we have new term (or terms), for which $S = M_S$ and $L = M_L$.

(3) Now decrease M_L by unity and repeat the above steps. Continue until the case $M_L = 0$, and then repeat the steps with M_S lower by 1. This time start the row of m_ℓ values in column 2 (or subsequent columns as calculations proceed) instead of column 1. Continue until the case $M_L = 0$ and $M_S = 0$ or $1/2$ is reached. Table III is the complete table for finding the allowed terms for a $3d^5$ configuration. The allowed terms of $3d^5$ configuration are $^6(S)$, $^4(G, F, D, P)$, and $^2(I, H, G_1, G_2, F_1, F_2, D_1, D_2, D_3, S)$.

Selection Rules

By replacing $e^{i\vec{k} \cdot \vec{r}_P}$ in Equation (71) by \vec{M} we can write the matrix element in Equation (71) as

TABLE III
ENUMERATION OF ALLOWED TERMS OF $3d^5$

S	M _S	m _l	M _S	M _L	Terms
$\frac{5}{2}$	$\frac{1}{2} \frac{1}{2} \frac{1}{2} \frac{1}{2} \frac{1}{2}$	2 1 0 -1 -2	$\frac{5}{2}$	0	6S
$\frac{3}{2}$	$\frac{1}{2} \frac{1}{2} \frac{1}{2} \frac{1}{2} \frac{1}{2}$	2 1 0 -1 2	$\frac{3}{2}$	4	4G
		2 1 0 -1 1		3	4G
		2 1 0 -2 2			4F
		2 1 0 -2 1		2	4G
		2 1 0 -1 0			4F
		2 1 -1 -2 2			4D
		2 1 0 -1 -1		1	4G
		2 1 0 -2 0			4F
		2 1 -1 -2 1			4D
		2 0 -1 -2 2			4P
		2 1 0 -1 -2		0	6S
		2 1 0 -2 -1			4G
		2 1 -1 -2 0			4F
		2 1 -1 -2 1			4D
		1 0 -1 -2 2			4P
$\frac{1}{2}$	$\frac{1}{2} \frac{1}{2} \frac{1}{2} -\frac{1}{2} -\frac{1}{2}$	2 1 0 2 1		6	2I
		2 1 0 2 0		5	2I
		2 1 -1 2 1			2H
		2 1 0 2 -1		4	4G
		2 1 0 1 0			2I

TABLE III (Continued)

S	M _S	m _ℓ	M _S	M _L	Terms
$\frac{1}{2}$	$\frac{1}{2} \frac{1}{2} \frac{1}{2} -\frac{1}{2} -\frac{1}{2}$	2 1 -1 2 0	$\frac{1}{2}$	4	^2H
		2 1 -2 2 1			$^2\text{G}_1$
		2 0 -1 2 1			$^2\text{G}_2$
		2 1 0 1 -1		3	^4G
		2 1 0 2 -2			^4F
		2 1 0 2 -2			^4F
		2 1 -1 2 -1			^2I
		2 1 -1 1 0			^2H
		2 1 -2 2 0			$^2\text{G}_1$
		2 0 -2 2 1			$^2\text{G}_2$
		2 0 -1 2 0			$^2\text{F}_1$
		1 0 -1 2 1			$^2\text{F}_2$
		2 1 0 1 -2		2	^4G
		2 1 -1 2 -2			^4F
		2 1 -2 2 -1			^4D
		2 0 -2 2 0			^2I
		2 0 -1 2 -1			^2H
		2 1 0 0 -1			$^2\text{G}_1$
		2 1 -1 1 -1			$^2\text{G}_2$
		2 1 -2 1 0			$^2\text{F}_1$
		2 -1 -2 2 1			$^2\text{F}_2$

TABLE III (Continued)

S	M _S	m _ℓ	M _S	M _L	Terms
$\frac{1}{2}$	$\frac{1}{2} \frac{1}{2} \frac{1}{2} -\frac{1}{2} -\frac{1}{2}$	2 0 -1 1 0	$\frac{1}{2}$	2	$2D_1$
		1 0 -1 2 0			$2D_2$
		1 0 -2 2 1			$2D_3$
		2 1 0 0 -2		1	$4G$
		2 1 -1 1 -2			$4F$
		2 1 -1 0 -1			$4D$
		2 1 -2 2 -2			$4P$
		2 1 -2 1 -1			$2I$
		2 0 -2 2 -1			$2H$
		2 0 -2 1 0			$2G_1$
		2 -1 -2 2 0			$2G_2$
		1 0 -2 2 0			$2F_1$
		2 0 -1 2 -2			$2F_2$
		2 0 -1 1 -1			$2D_1$
		1 0 -1 2 -1			$2D_2$
		1 0 -1 1 0			$2D_3$
		2 1 0 -1 -2		0	$6S$
		2 1 -1 0 -2			$4G$
		2 1 -2 1 -2			$4F$
		2 1 -2 0 -1			$4D$
		2 0 -2 2 -2			$4P$

TABLE III (Continued)

S	M _S	m _ℓ	M _S	M _L	Terms
$\frac{1}{2}$	$\frac{1}{2} \frac{1}{2} \frac{1}{2} - \frac{1}{2} - \frac{1}{2}$	2 0 -2 1 -1	$\frac{1}{2}$	0	2I
		2 -1 -2 2 -1			2H
		2 -1 -2 1 0			2G_1
		1 0 -2 2 -1			2G_2
		1 0 -2 1 0			2F_1
		2 0 -1 1 -2			2F_2
		2 0 -1 0 -1			2D_1
		1 0 -1 2 -2			2D_2
		1 0 -1 1 -1			2D_3
		0 -1 -2 2 1			2S

$$\langle \psi_f^{el} | \vec{M} \hat{\pi}_k^\lambda | \psi_j^{el} \rangle = \langle \psi_j^{el} | \Gamma_v | \psi_i^{el} \rangle . \quad (85)$$

The three components of the electric dipole operator transform as x , y , and z ; the three components of the magnetic dipole operator as the components of orbital angular momentum, i.e., L_x , L_y , and L_z . The electric dipole operator is an odd operator while magnetic dipole operator is an even operator.

If Γ_i and Γ_f are, respectively, the initial and the final state of the vibronic transition, and Γ_r is the representation of the dipole operator, then the selection rules may be stated simply by saying that a transition is allowed if the direct product $\Gamma_r \times \Gamma_v \times \Gamma_i$ contains Γ_f . In other words, if the direct product $\Gamma_f \times \Gamma_r \times \Gamma_v \times \Gamma_i$ contains the totally symmetric representation, the transition from i to f state is allowed. When we ignore an active vibrational mode, the transition from i to f is allowed if the direct product $\Gamma_r \times \Gamma_i$ contains Γ_f .

CHAPTER III

EXPERIMENTAL PROCEDURE

The KMgF_3 and $\text{KMgF}_3:\text{Mn}$ crystals used in these experiments were grown by the Stockbarger technique^(27,84). The Mn-doped crystals contain 0.04, 0.4, and 1.4 at. % Mn respectively and the concentrations were used to calculate the oscillator strengths of the observed Mn^{2+} optical transitions in the crystals. Impurity analyses of some of these samples have been published⁽³¹⁾.

Vehse et al.⁽⁸⁵⁾ have demonstrated that KMgF_3 and KMnF_3 form solid solutions in all proportions and it is felt that the Mn^{2+} ions are well distributed even in the heavily doped samples.

Samples about 1 mm thick were cut parallel to the thermal fracture planes {100} using an IMANCO Macrotome diamond saw, and polished using a Syntron LP-01 vibratory polisher with a Linde A/distilled water slurry. Any major irregularities were removed before polishing by hand lapping on a glass plate with number 600 carborundum grit in mineral oil. Crystal orientations were checked using Laue X-ray back reflection techniques.

The samples were irradiated either with ^{60}Co gamma source or 2 Mev electrons from a Van de Graaff accelerator at dose rate of about 1.85×10^{13} Mev/cm² sec. Most of the samples were irradiated either at room temperature or 80°K. For low temperature irradiation the samples were held in the cryostat manufactured by the Sulfrin Cryogenic Corporation.

Most of the optical absorption measurements were made on a Cary 14 spectrophotometer between liquid helium temperature and room temperature. When high resolution spectra were needed, a one-meter Jarrel-Ash Czerny-Turner monochromator with a dispersion of $8.2 \text{ \AA}/\text{mm}$ and a GE 200 w quartz-iodine standard lamp were used. All polarized absorption measurements were made in a Cary 14 spectrophotometer using Polaroid type HNP'B unsupported ultraviolet polarizers in both the sample and reference beams. This system transmitted light as low as 190 nm, but the polarization was effective only to about 230 nm. The polarizers could be oriented to place the transmission direction for the electric vector of the incident light along any desired crystallographic direction of the crystal being studied.

The Cary 14 spectrophotometer records the optical density as a function of wavelength. The optical density, $\text{O.D.} = \log_{10}(I_0/I)$, is related to the absorption coefficient by $\alpha = 2.303 (\text{O.D.}/x) \text{ cm}^{-1}$, where I and I_0 are the intensities of the optical beam respectively and x is the sample thickness. The sample thickness was carefully measured in several places using micrometer. The oscillator strengths (f numbers) were determined by means of the formula of Smakula, i.e., Equation (54), and from the measured area under the absorption bands.

Luminescence measurements were made on the Jarrel-Ash one-meter monochromator with excitation accomplished by means of various light sources (75 w short arc Xenon lamp X-75 by PEK, Inc., 100 w short arc mercury lamp PEK 112 by PEK, Inc., and 200 w quartz-iodine lamp by General Electric Co.) passed through a SPEX Minimate 22 cm monochromator manufactured by a SPEX Industries, Inc. The light was chopped at a frequency of 450 HZ with Keithley Model 8403-450 light chopper. A block

diagram of the luminescence apparatus is shown in Figure 3. The sample was rotated slightly off of a 45° angle to minimize reflection of the exciting light into the detection system. A diagram of the sample orientation with respect to both the incident light and the detection system for absorption and emission is shown in Figure 2. As mentioned above the emission spectra were analyzed with a Jarrel-Ash one-meter monochromator and detected with an RCA C31034 photomultiplier tube at 800 V DC at room temperature. The output from this phototube was conditioned by a Keithley Model 840 lock-in amplifier. The detected luminescence intensity was displayed against wavelength on a Model 2D-2 X-Y recorder by F. L. Moseley Co. Absolute calibration of the exciting light and the detection system were accomplished with a quartz-iodine standard lamp having calibration traceable to the National Bureau of Standards. The response factor of luminescence detection system determined from the calibration and the spectral irradiance of PEK X-75 Xenon short arc lamp are shown in Figures 4 and 5.

For all low temperature optical measurements either a Sulfrian cryostat or a Displex helium refrigerator Model CS-202 by Air Products and Chemicals, Inc., were used. These units were equipped with a rotatable tail section with quartz windows. By balancing the heat input from a small electric heater immersed in the Sulfrian cryostat against the removal of heat by the cold liquid, sample temperatures between 4.2 and 300°K could be obtained. With the Displex helium refrigerator, temperature between 12°K and room temperature could be obtained and held accurately for long periods of time. The temperature in both sample units were measured with a thermocouple consisting of number 36 gauge gold: 0.7 at. % iron versus chromel P wire.

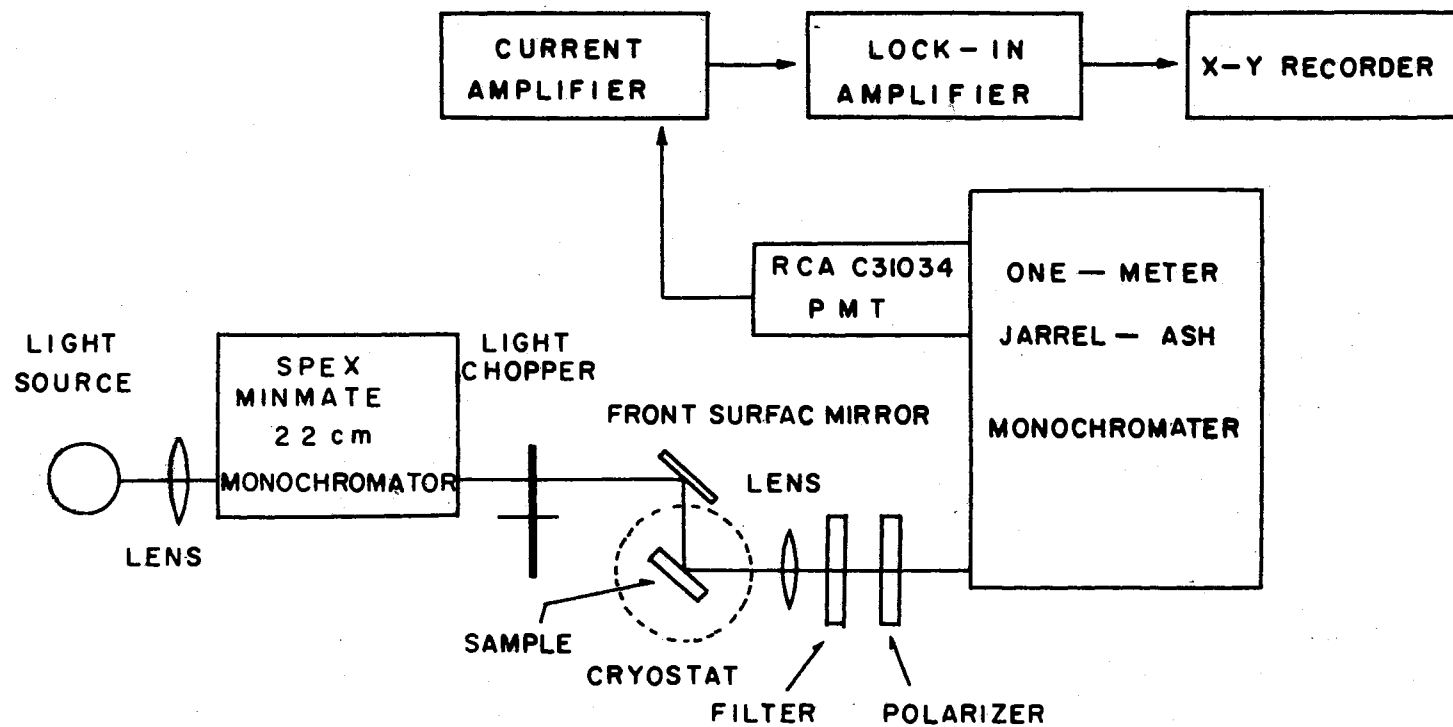


Figure 3. Block Diagram of Luminescence Apparatus

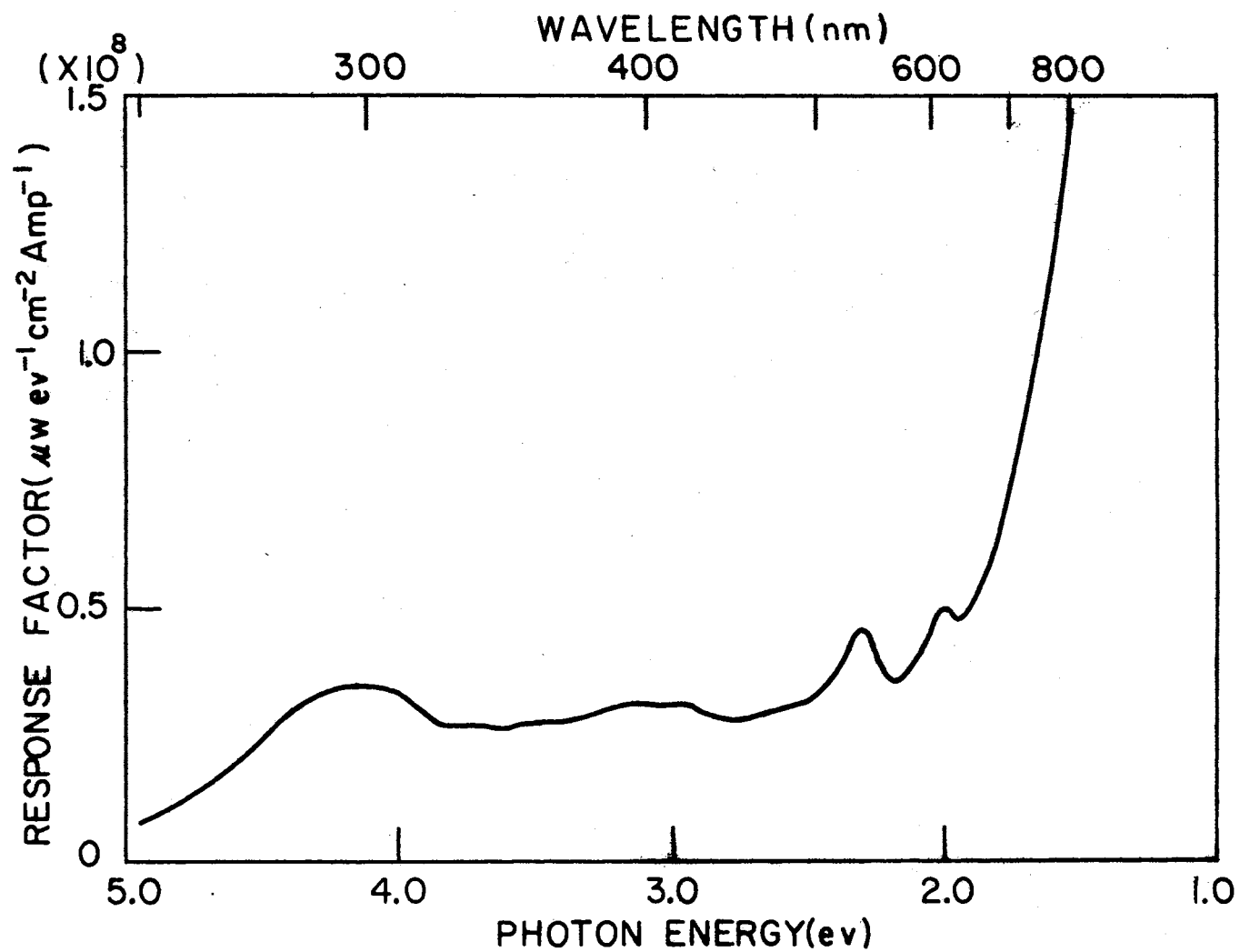


Figure 4. Response of Luminescence Detection System as a Function of Photon Energy

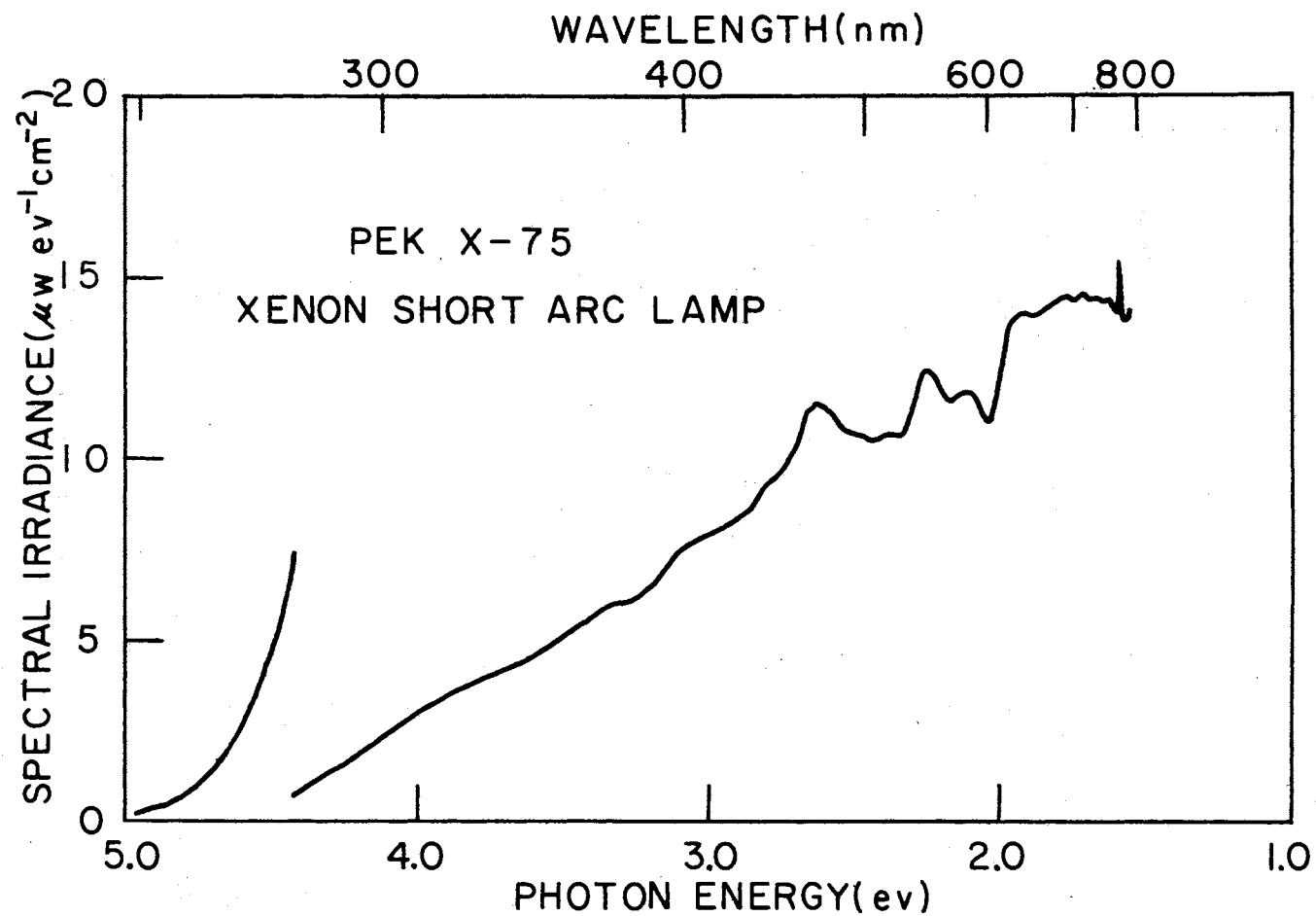


Figure 5. Spectral Irradiance of PEK-75 Xenon Short Arc Lamp as a Function of Photon Energy

The optical excitation spectrum for a luminescence band could be taken with the same apparatus described above with SPEX Minimate 22 cm monochromator driven by a synchronous motor drive. In all cases, care was taken to insure that the natural line widths of the absorption or emission were greater than the instrument resolution. Luminescence bands which consisted of two different lifetimes could be easily resolved by phasing the lock-in amplifier. Corning glass filter with optical sharp cut off were used to eliminate higher orders of the exciting light from the monochromator output.

Most of the radiative lifetime measurements were made on a nanosecond decay time fluorescence measuring system manufactured by ORTEC, Inc., and series 1100 analyzer system by Nuclear Data, Inc. A phase sensitive lock-in amplifier was also used to measure a radiative lifetime of one emission band.

Two types of annealing experiments were utilized. In the case of a continuous anneal, an immersion heater was used to slowly warm the sample while the Cary 14 spectrophotometer or luminescence apparatus monitored the absorption or luminescence for the bands in question. For an isochronal anneal, an optical spectrum was originally recorded at 77°K; then an immersion heater was used to quickly warm the sample to the desired temperature which was maintained for ten minutes. The sample was then quenched to 77°K and an optical spectrum recorded. Above ambient temperature, a small furnace capable of holding the sample temperature constant at temperatures up to 1300°K was used to heat the sample to desired temperature. After 10 minutes at temperature, the sample was removed and quenched on a brass block at 300°K. The optical spectrum was then recorded.

CHAPTER IV

OPTICAL ABSORPTION AND EMISSION

FROM DEFECTS IN KMgF_3

Color Center Absorption in KMgF_3

The absorption spectrum at 15°K for a KMgF_3 sample electron irradiated at 300°K is shown in Figure 6. According to Hall and Leggeat⁽²⁹⁾, and Riley and Sibley^(27,31) the bands at 275, 445, and 395 nm are due to the F , F_2 , F_3 centers, respectively. The 340 nm band which was observed only at low temperature for a sample irradiated at below LNT was also identified as due to the V_k centers. Additional bands at 570, 360, and 500 nm have been observed at room temperature. Several other weak bands at 477, 220, and 340 have also been recorded at low temperature. Among these bands the 477 nm band when measured at 10°K has a zero-phonon line on the low energy side of the broad band.

A study of the temperature dependence of the band width at half-maximum and the peak position of the 570 nm absorption band was undertaken. A Gaussian plot for the 570 nm band is shown in Figure 7. In Figure 8, the full width at half-maximum, $W_{1/2}$, and the peak position, ϵ_{max}^A , obtained from the Gaussian graphs are plotted versus $T^{1/2}$ for the 570 nm absorption band. Figure 9 portrays $\coth^{-1}(W(T)/W(0))^2$ versus $1/T$. These data are necessary to determine the parameters needed in construction of a configuration coordinate diagram for the center. A

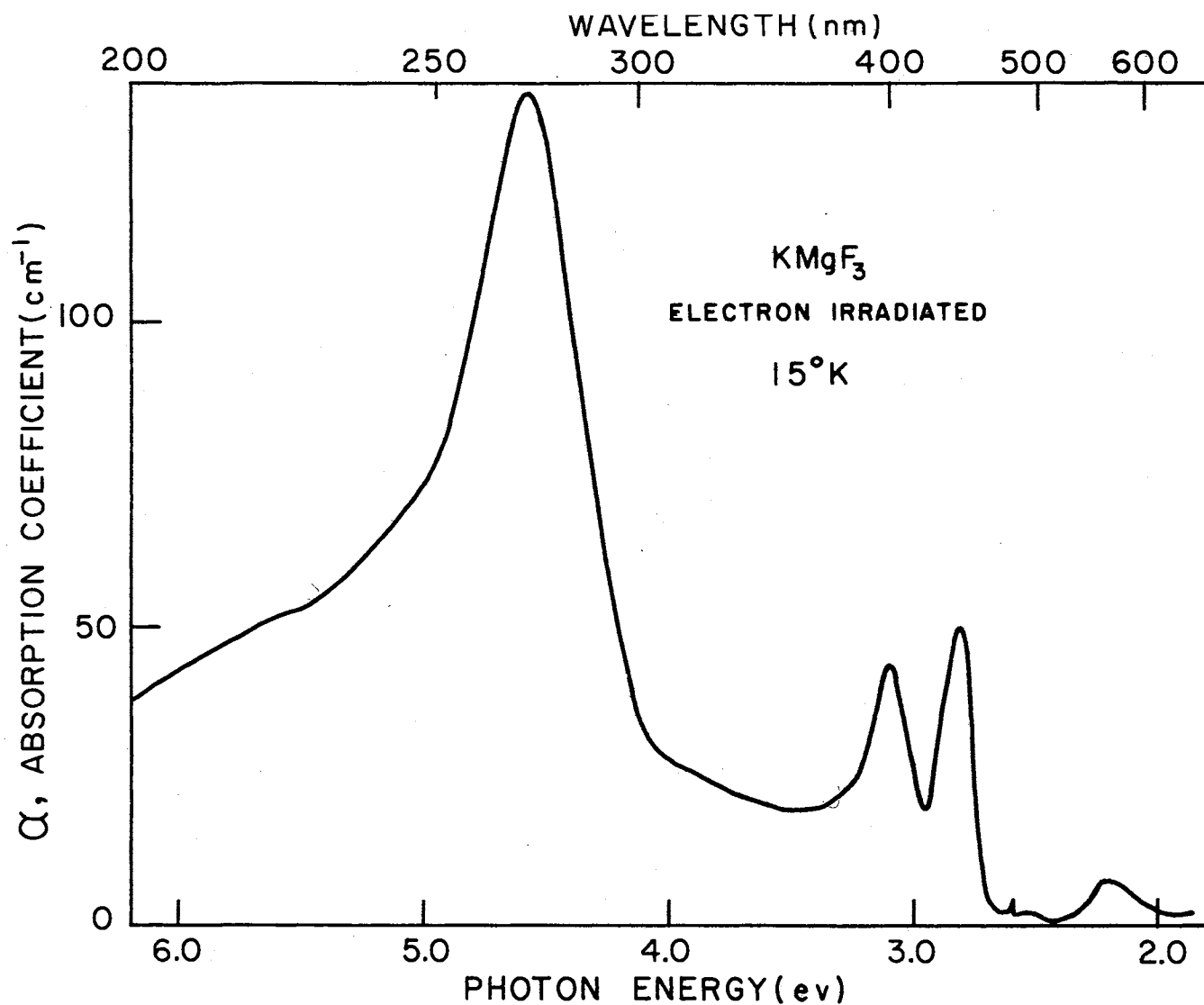


Figure 6. Absorption Spectrum of KMgF_3 at 15°K Following an Electron Irradiation at 300°K

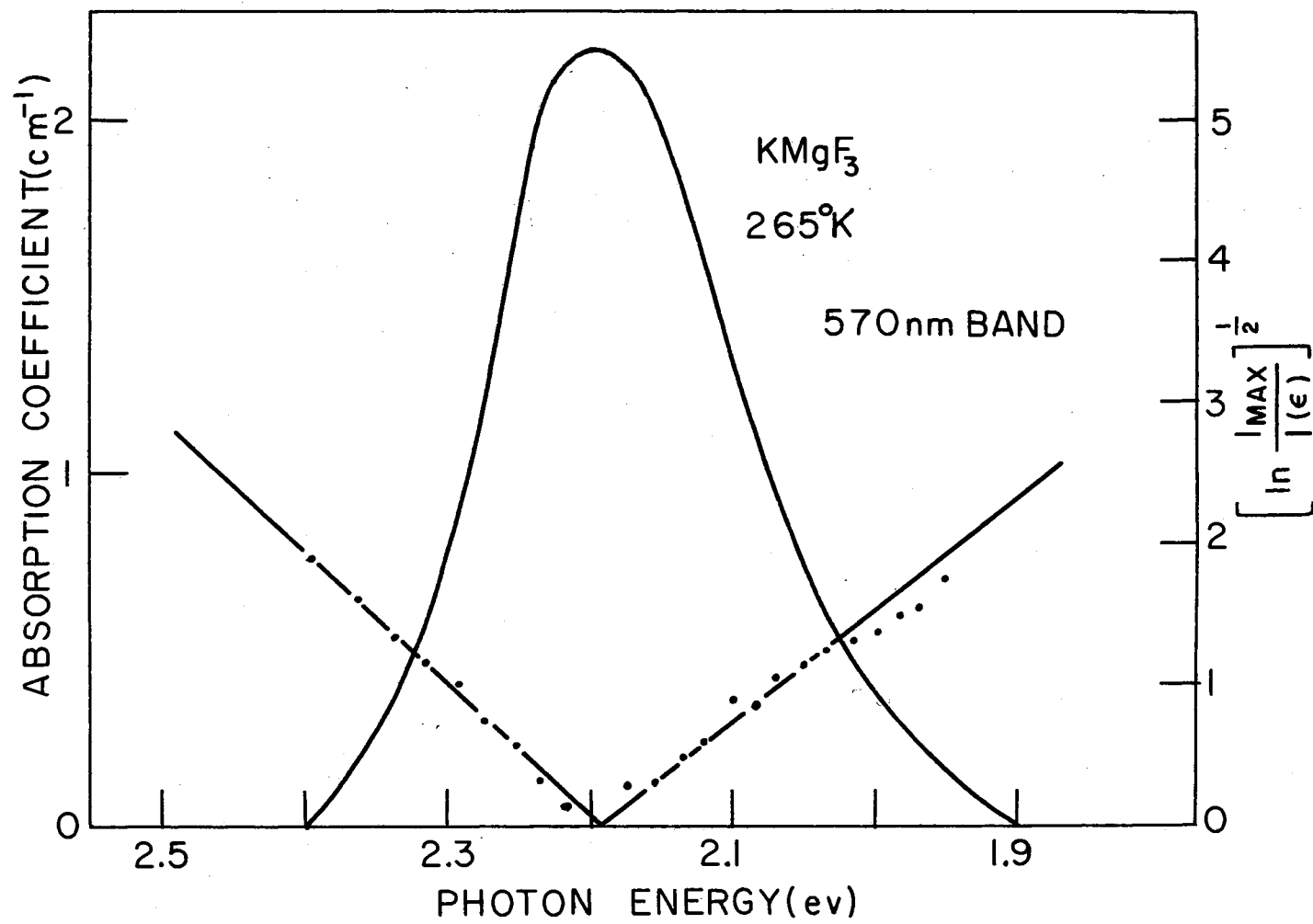


Figure 7. Gaussian Plot for 570 nm Absorption Band in KMgF_3

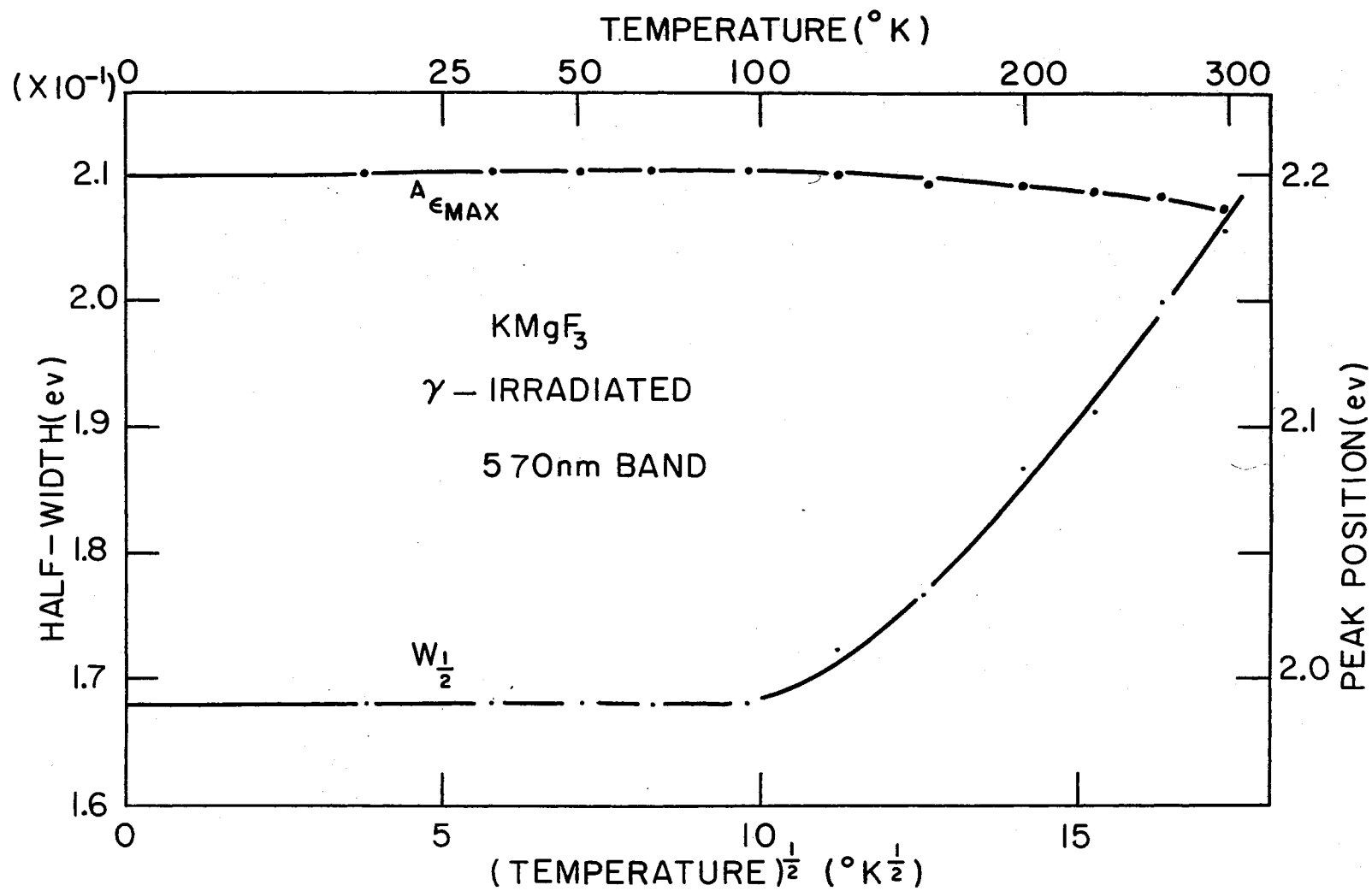


Figure 8. Temperature Dependence of $W_{1/2}$ and ϵ_{\max}^A for 570 nm Absorption Band in KMgF_3

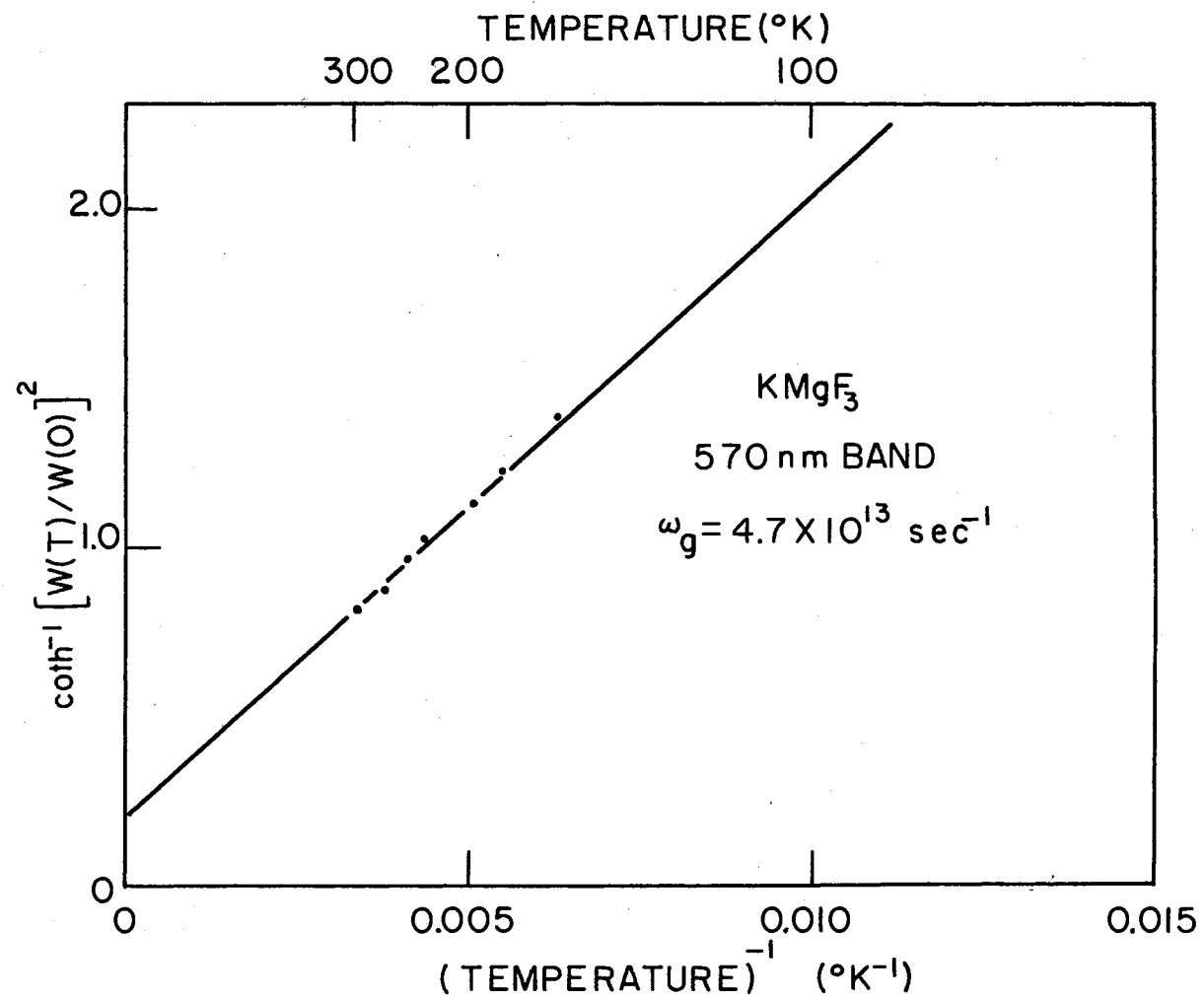


Figure 9. Temperature Dependence of Half-Width of 570 nm Absorption Band in KMgF₃

value of $\omega_g = 4.7 \times 10^{13} \text{ sec}^{-1}$ can be determined from the slope of the line and Equation (83). A value of $S \approx 5.3$ is obtained. A zero-phonon line corresponding to the 570 nm absorption band has not yet been observed; however, there is a possibility to observe the zero-phonon line with a high resolution monochromator.

In order to find the relation among π_1 , π_2 , and σ of F_2 centers which have been already discussed in Chapter II, a polarized bleaching experiment was performed. The results are shown in Figure 10. In the top panel of this figure, the two curves labeled $[1\bar{1}0]$ and $[110]$ are the $[1\bar{1}0]$ and $[110]$ spectra taken after the crystal was bleached at 300°K with $[110]$ 254 nm light. The term $[110]$ light is used to refer to light propagating in the $[001]$ direction with the electric vector parallel to a $[110]$ direction. As discussed in Equation (60) the center panel of this figure shows the anisotropic absorption A_{110} and the lower panel shows the anisotropic absorption A_{100} following a $[010]$ 254 nm light optical bleach. Since both A_{110} and A_{100} are non-zero, the center giving rise to the absorption band at 445 nm is a $\langle 110 \rangle$ -type center and thus most likely the F_2 center. There is another transition at 282 nm with transition moment perpendicular to that of the 445 nm absorption band. From the analysis of an anisotropic absorption due to oriented defects using Table I, the results for a $\langle 110 \rangle$ -type center are

$$A_{110} = (n_1 - n_2) (\sigma - \pi_1),$$

and

(86)

$$A_{100} = (n_5 + n_6 - n_3 - n_4) \left(\frac{1}{2} \sigma + \frac{1}{2} \pi_1 - \pi_2 \right).$$

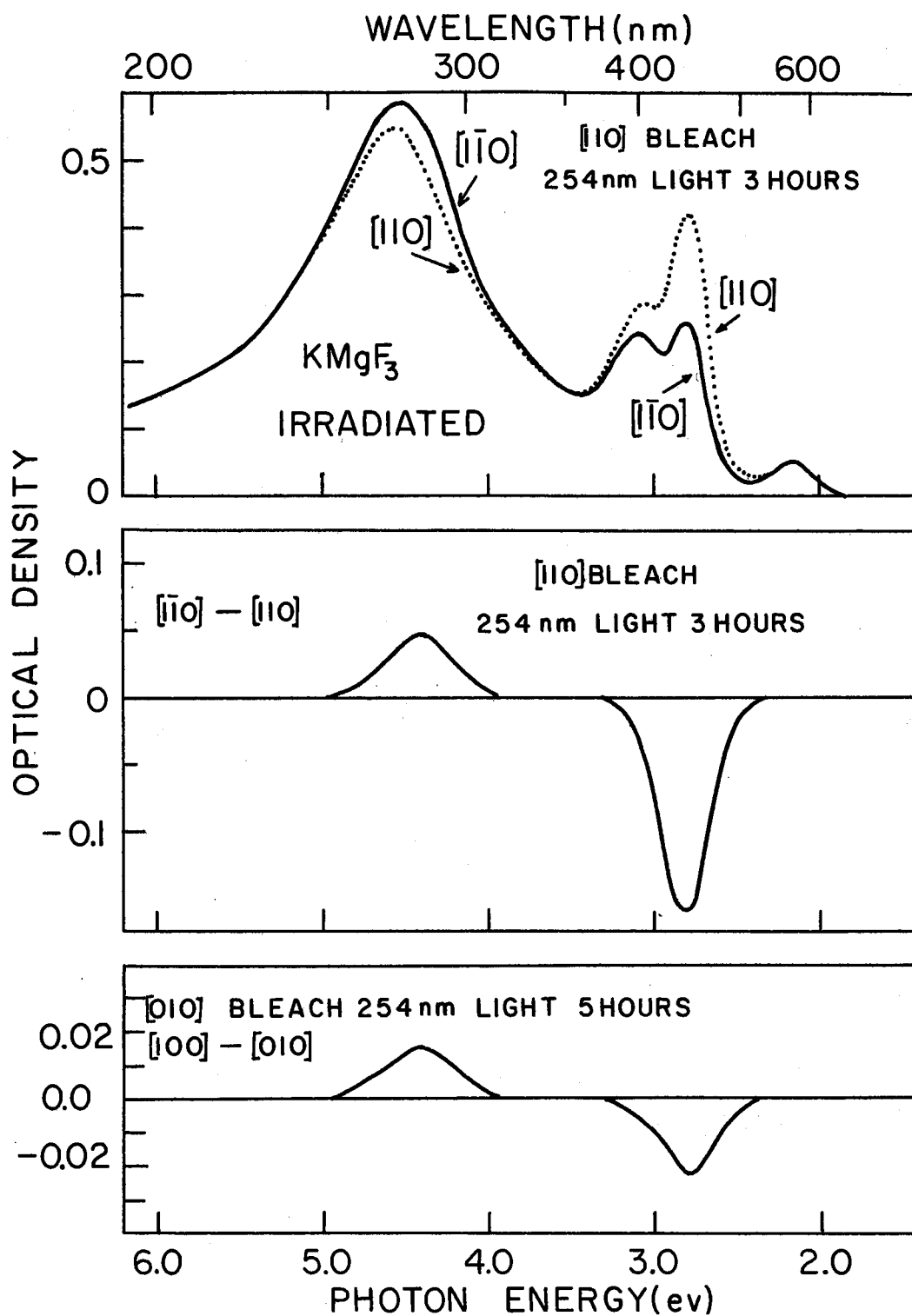


Figure 10. Anisotropic Absorption in KMgF_3 as a Function of Photon Energy Following an 254 nm Optical Orientation

Using these equations and the polarized absorption data, the relations $\pi_1 = 0.29\sigma$ and $\pi_2 = 0.48\sigma$ are obtained from the polarized absorption data. It should be noted that both A_{110} and A_{100} have opposite signs in the 445 and 282 nm region. If the absorption band at 445 nm results from a σ type dipole transition, then it is necessary to assume that the 282 nm absorption band results from a π_1 and π_2 transitions.

It was found that only light with wavelength corresponding to the π electric dipole transition is efficient at reorienting centers. This observation is further verified by attempts at bleaching not in the 282 nm region (where the absorption is due to π transitions) but in the 445 nm band itself. In this case, no reorientation of centers was observed. The distribution of defects shown in Table IV, which was calculated from polarized absorption measurements and Table I for the different polarizations of bleaching light, suggests that F_2 centers reorient by 60° jump, e.g., a defect with a $[110]$ \hat{r}_1 orientation can only jump to \hat{r}_3 , \hat{r}_4 , \hat{r}_5 , and \hat{r}_6 orientations. The results of isochronal annealing of color centers in KMgF_3 up to 800°K are shown in Figure 11. The F band has definite annealing stages at 450°K and 600°K , whereas the F_2 band has an annealing stage at 580°K . The F_3 center concentration increases in the range from 300 to 450°K and has definite annealing stages at 530 and 630°K . The 570 nm band and F_2 band show almost the same annealing characteristics. This result, the annealing character for low temperature irradiated sample up to 300°K ⁽²⁷⁾, and the mechanism of F -aggregate center formation suggested by Farge et al.⁽⁸⁶⁾ and Schneider⁽⁸⁷⁾, suggests that the 570 nm absorption band is possibly due to the F_2^+ centers. However, considerable work must yet be done before such an assignment can be made. An ultraviolet bleach at LNT produced new bands

TABLE IV
OBSERVED AND PREDICTED ABSORPTION COEFFICIENTS FROM ORIENTED F_2 CENTERS

Abs. coeff.	[1 $\bar{1}$ 0] Bleach		[110] Bleach	
	Predicted abs. from luminescence	Obs. abs. coeff.	Predicted abs. from luminescence	Obs. abs. coeff.
α_{110}	3.30 $\sigma\bar{n}$	5.2	4.01 $\sigma\bar{n}$	5.9
$\alpha_{1\bar{1}0}$	3.88 $\sigma\bar{n}$	7.0	3.21 $\sigma\bar{n}$	4.3
α_{K2}	3.71 $\sigma\bar{n}$	6.4	3.40 $\sigma\bar{n}$	3.9
$\alpha_{K2'}$	3.59 $\sigma\bar{n}$	6.1	3.22 $\sigma\bar{n}$	3.8
$\alpha_{110}/\alpha_{1\bar{1}0}$	0.87	0.74	1.25	1.37
$\alpha_{K2}/\alpha_{K2'}$	1.03	1.05	1.05	1.03

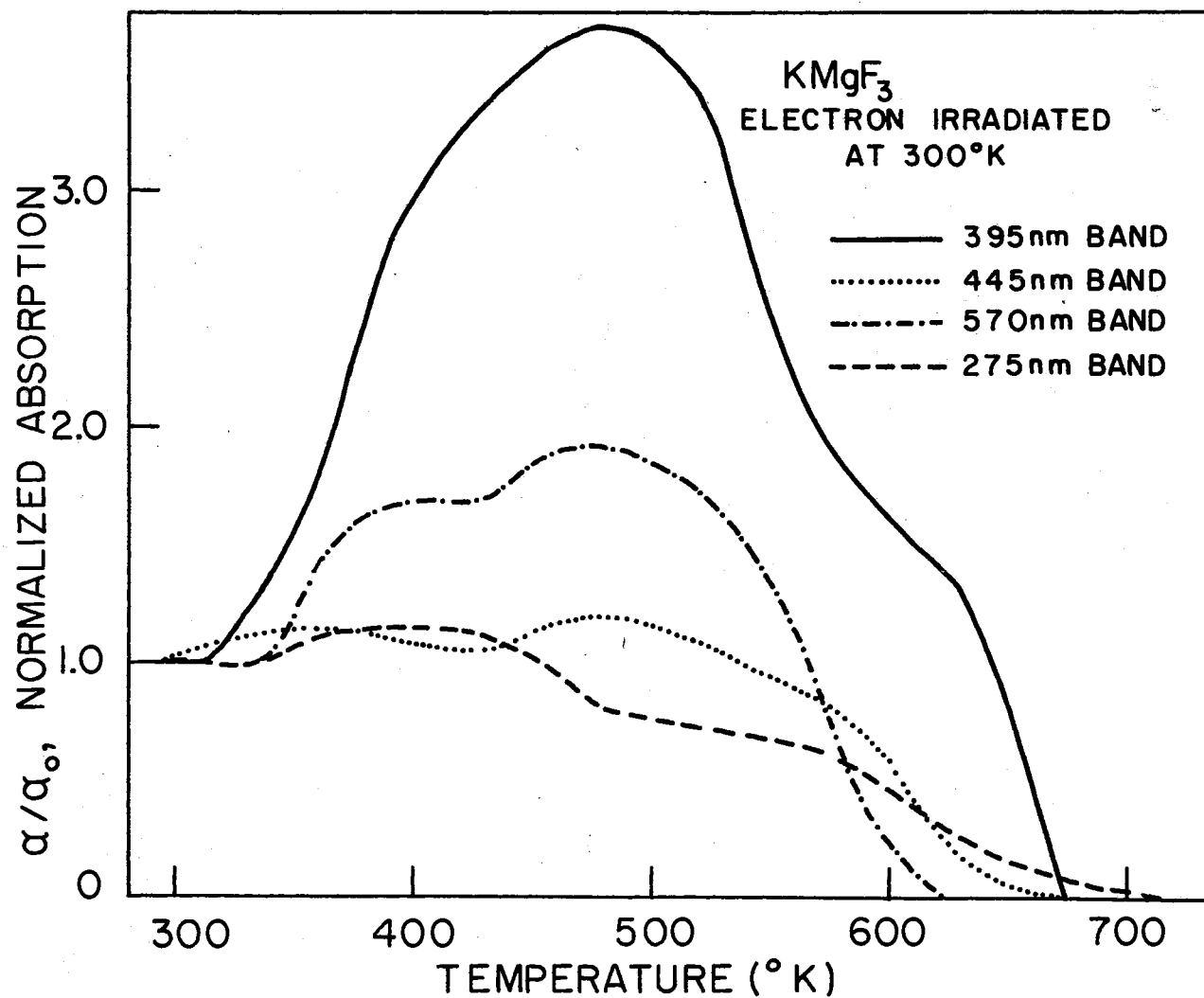


Figure 11. Isochronal Annealing Curves for 395 (F_3), 445 (F_2), 275 (F) and 570 nm Absorption Bands in KMgF_3

at 220 nm and a broad band at 340 nm in the irradiated KMgF_3 . These bands are shown in Figure 12. Annealing characteristics of these bands are shown in Figure 13. When the 220 and 340 nm bands disappear the F_2 band grows in while the F_3 band shows no change at all. Considering the production mechanism and the annealing character of these bands, the 340 nm band may be due to F^- centers (F' centers) and 220 nm band due to F^+ (α) centers. However, the 220 nm band is probably too close to the F band and too far away from the absorption edge of KMgF_3 crystals to be an F^+ (α) band. The data are not sufficient to make a definite assignment at this time.

The optical absorption spectrum taken immediately after γ -irradiation shows very small concentration of F_3 centers. By optical bleaching in the F or F_2 band regions one can increase the concentration of F_3 centers. Short γ -irradiation destroys almost all F_3 centers which were already presented in KMgF_3 crystal and convert them into the F and F_2 centers.

Color Center Emission in KMgF_3

When a sample of KMgF_3 is irradiated with 2.0 Mev electrons or ^{60}Co γ -rays at room temperature and is then excited with light of appropriate wavelengths various emission bands at 410, 590, 465, and 750 nm are observed. The temperature dependence of 590 and 465 nm emission bands have been published⁽⁸⁸⁾.

590 nm Emission

In order to find the color center responsible for 590 nm emission three experiments were performed. First, the emission intensity of 590

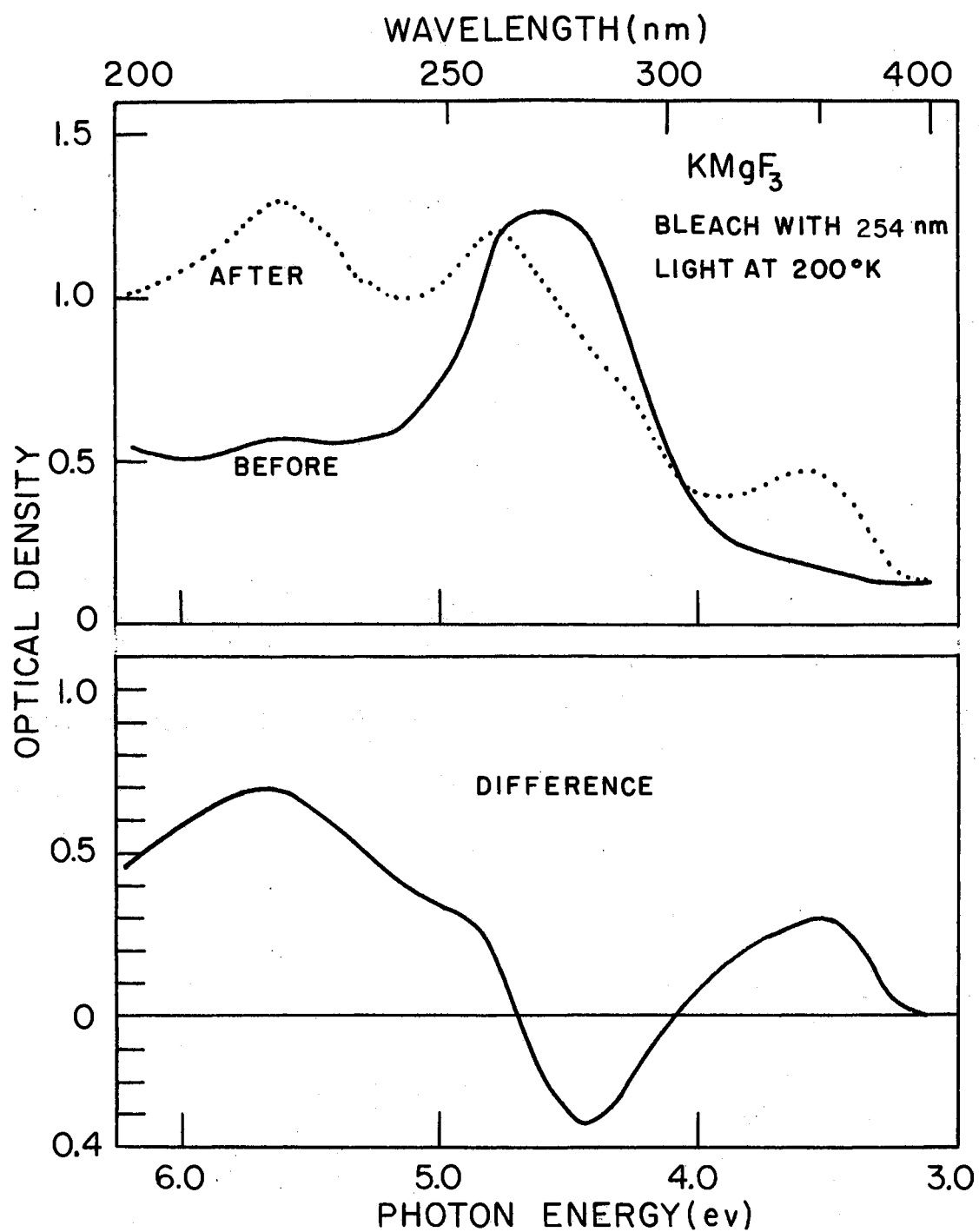


Figure 12. Absorption Spectrum in KMgF_3 Following a 254 nm Bleaching at 200°K

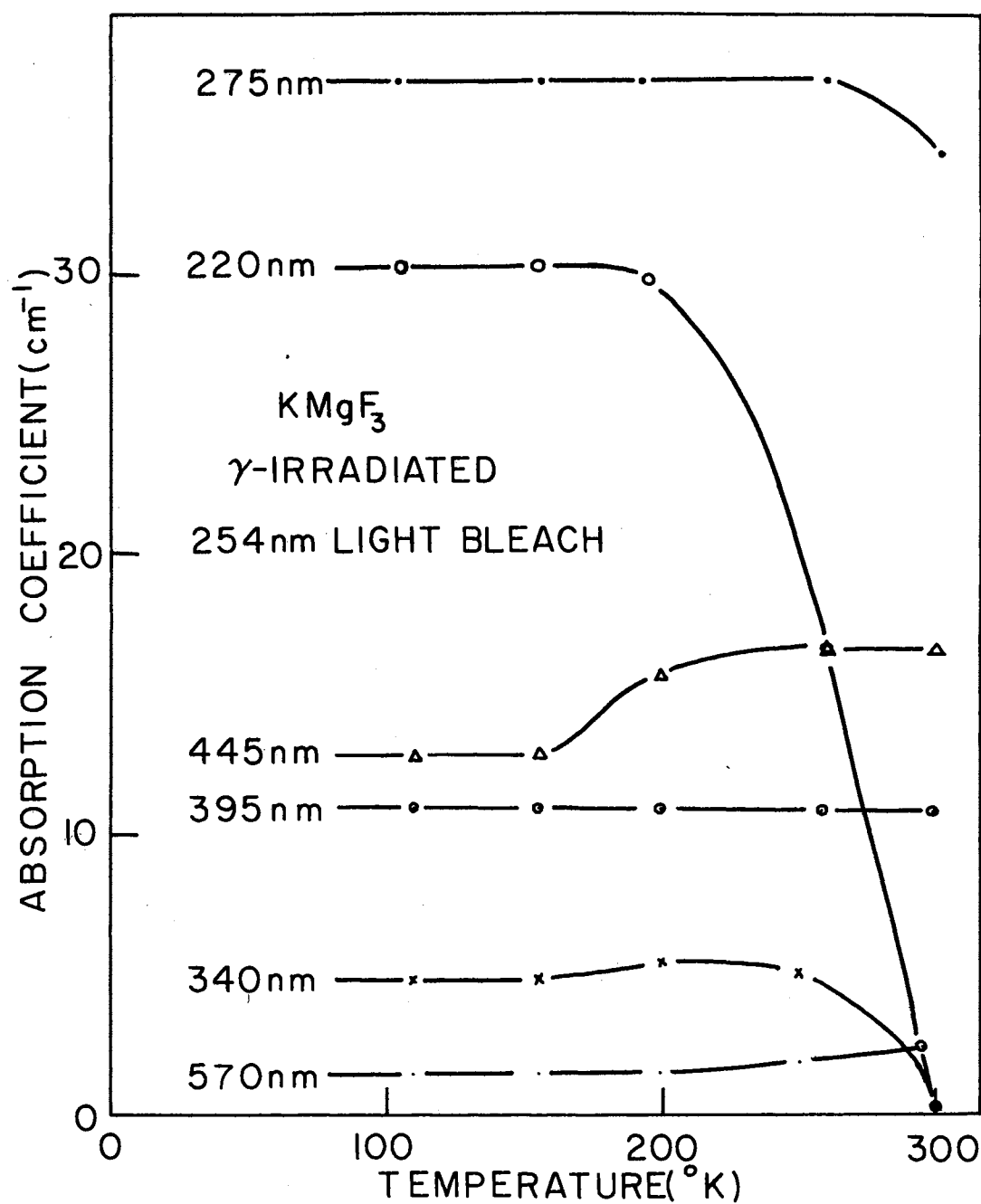


Figure 13. Annealing Curves for 220 and 340 nm Band in KMgF_3

nm band was measured as a function of the absorption coefficients at the peak of each optical absorption band. The F_2 band was the only band which had a straight-line relationship with the emission intensity of 590 nm band. The results are illustrated in Figure 14. This suggests that the 590 nm band is due to F_2 centers. The second study dealt with orienting F_2 centers with polarized 254 nm light and then observing the emission to find the band or bands that were polarized. In Table V, the observed polarized luminescence values are analyzed by the relations for the σ - σ case in Table II and the defect distributions, present after polarized bleaching, are determined.

TABLE V

EMISSION INTENSITY RATIOS FOR SAMPLES BLEACHED WITH POLARIZED LIGHT
AND THE DEFECT DISTRIBUTIONS DETERMINED FROM THE RATIOS

Emission Intensity Ratios (590 nm)	Polarization of Bleaching Light			
	$[1\bar{1}0]$	$[100]$	$[110]$	Random
I_{12}/I_{11}	0.252	0.186	0.12	0.34
I_{21}/I_{22}	0.673	1.06	1.20	1.20
I_{22}/I_{11}	0.427	0.22	0.122	0.25
Defect Distributions	$\bar{n} = \frac{1}{6} \sum_{i=1}^6 n_i$			
n_1	$0.94 \bar{n}$	$1.36 \bar{n}$	$1.98 \bar{n}$	\bar{n}
n_2	$1.75 \bar{n}$	$1.15 \bar{n}$	$0.87 \bar{n}$	\bar{n}
$n_3 + n_6$	$1.77 \bar{n}$	$1.93 \bar{n}$	$1.75 \bar{n}$	$2\bar{n}$
$n_4 + n_5$	$1.54 \bar{n}$	$1.55 \bar{n}$	$1.40 \bar{n}$	$2\bar{n}$

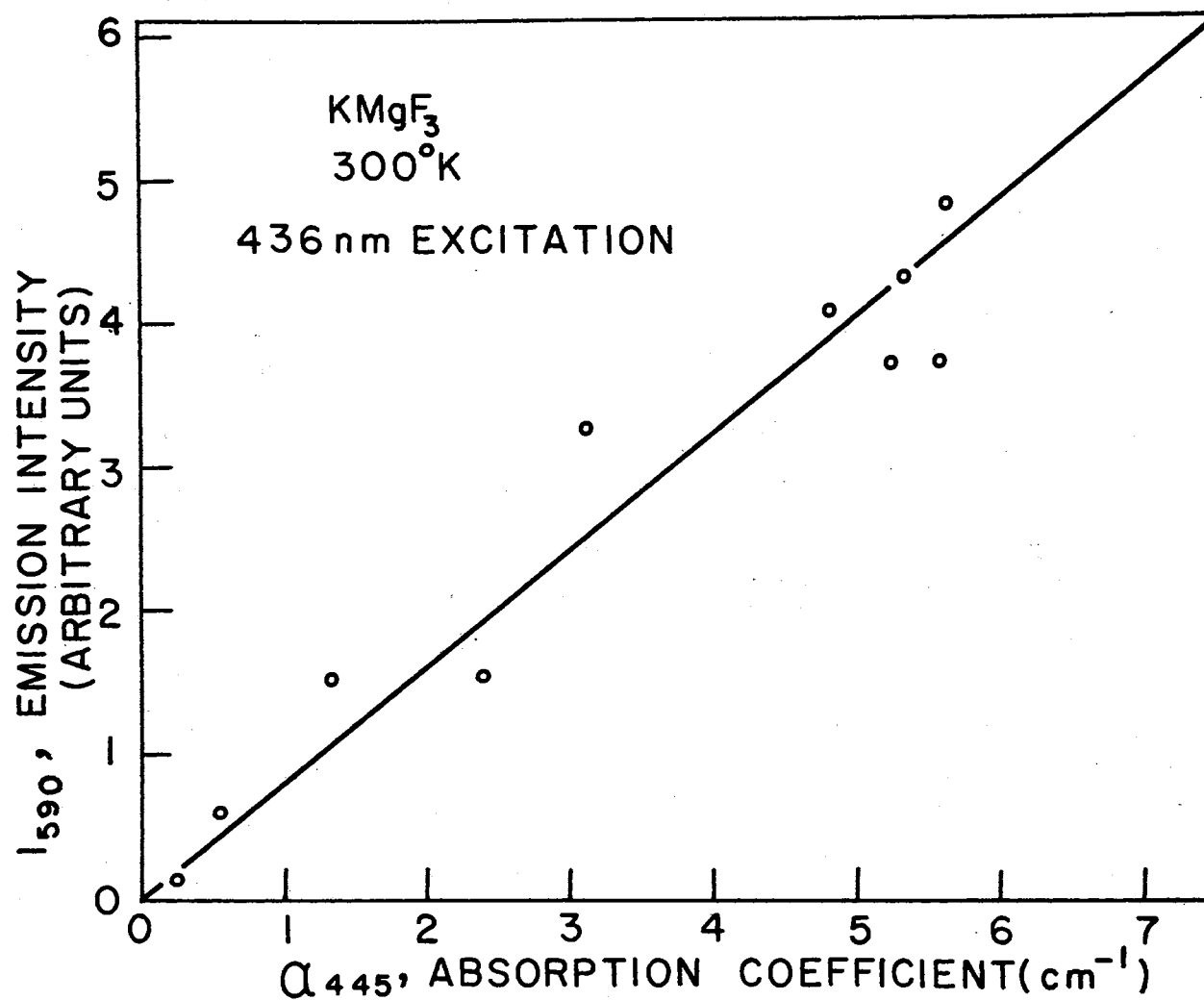


Figure 14. Plot of the Emission Intensity at 590 nm Due to 436 nm Light Excitation Versus the Absorption Coefficient at 445 nm

Using these values and the relations $\pi_1 = 0.29\sigma$ and $\pi_2 = 0.48\sigma$ which were obtained from the polarized absorption measurements, the agreement between the emission and absorption measurements can be evaluated. This is shown in Table IV and the agreement appears to be very good. This experimental results again suggests that the 590 nm emission band is due to F_2 centers. The third study dealt with the excitation spectrum of 590 nm emission band. When, with the sample at room temperature, the detecting monochromator is set at 590 nm and the excitation wavelength is varied, the excitation spectrum shown in Figure 15 is obtained. In the excitation spectrum one finds two bands at 445 and 282 nm. The peak positions of the excitation spectrum match very nicely with the peak positions of the anisotropic absorption spectrum in Figure 10. The 445 nm band corresponds to a σ transition of an F_2 center whereas the 282 nm band is due to a π transition of F_2 center. Figure 16 shows the excitation spectrum at 15°K for the 590 nm emission band. Inset shows the 590 nm emission band. All the excitation spectra were calibrated with the light sources which were used for excitations. Using the excitation spectrum technique one can separate π transition of F_2 center which was hidden under the F band. These results again indicate that the emission band at 590 nm is due to F_2 centers.

465 nm Emission

Studies similar to those described above for the 590 nm emission band were carried out for the 465 nm emission band. Figure 17 indicates a definite relationship between the emission intensity at 465 nm and the absorption coefficient of the 395 nm absorption band which is due to F_3 centers. Moreover, after the F_3 centers are oriented by a polarized

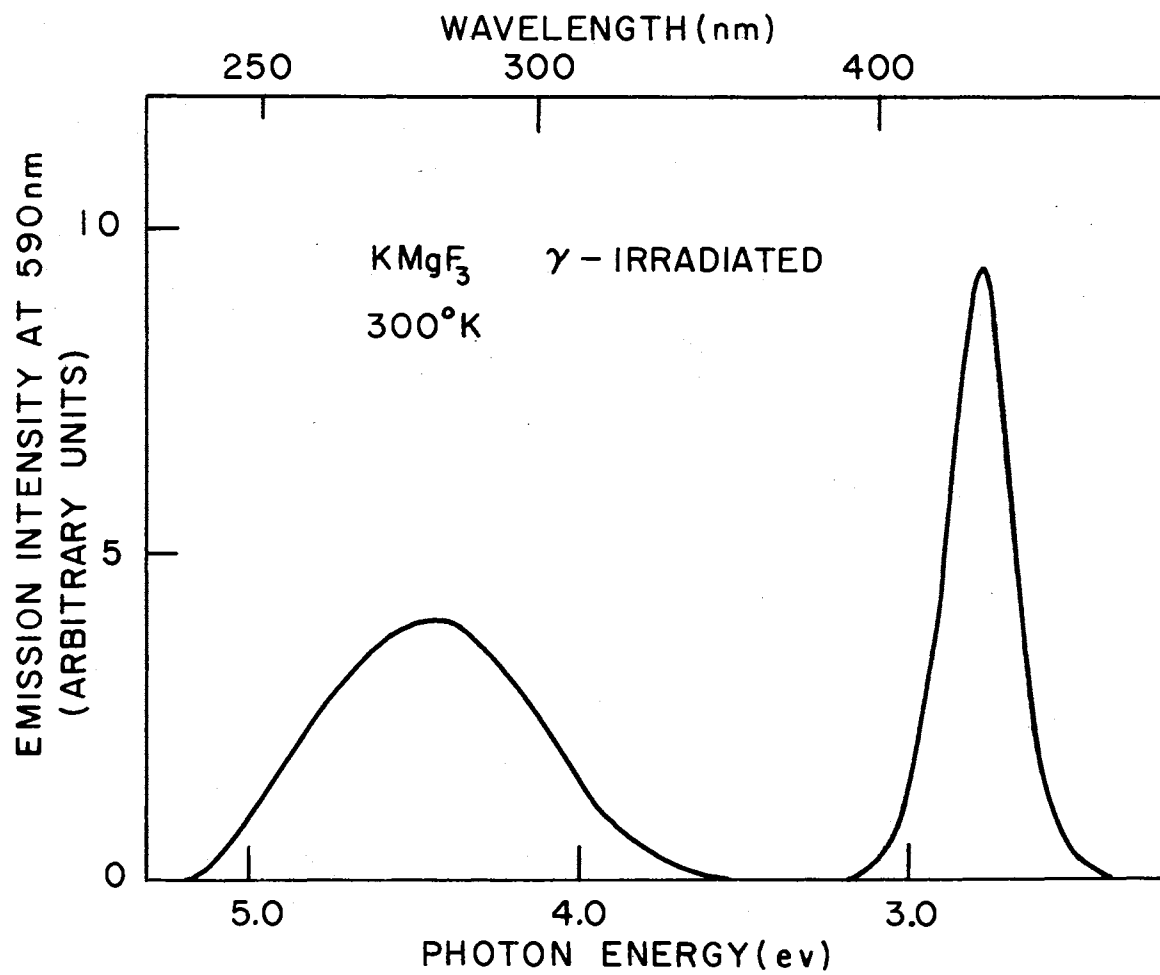


Figure 15. Excitation Spectrum for 590 nm (F_2) Emission Band in KMgF_3 at 300°K

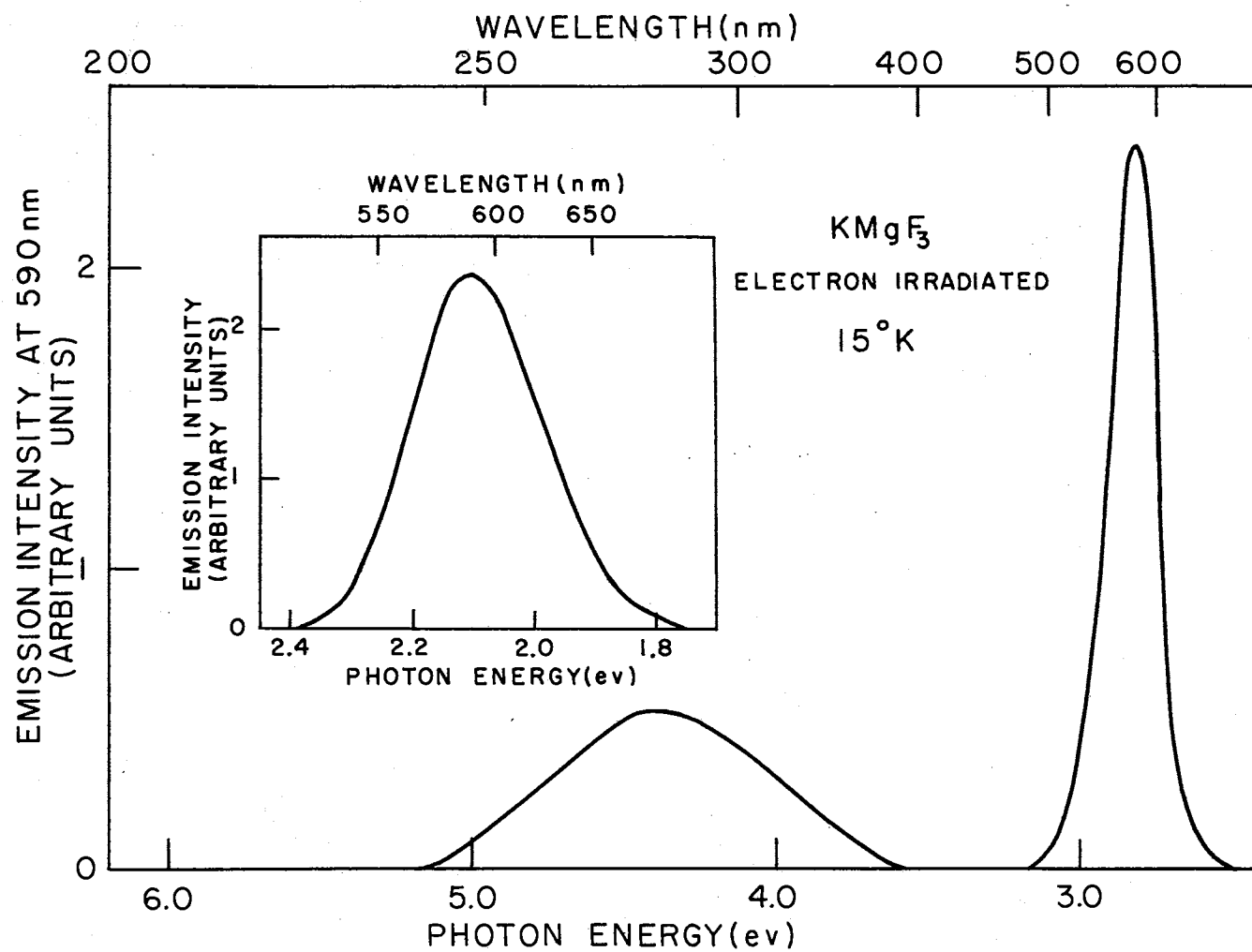


Figure 16. Excitation Spectrum and 590 nm (F_2) Emission Band in KMgF_3 at 15°K

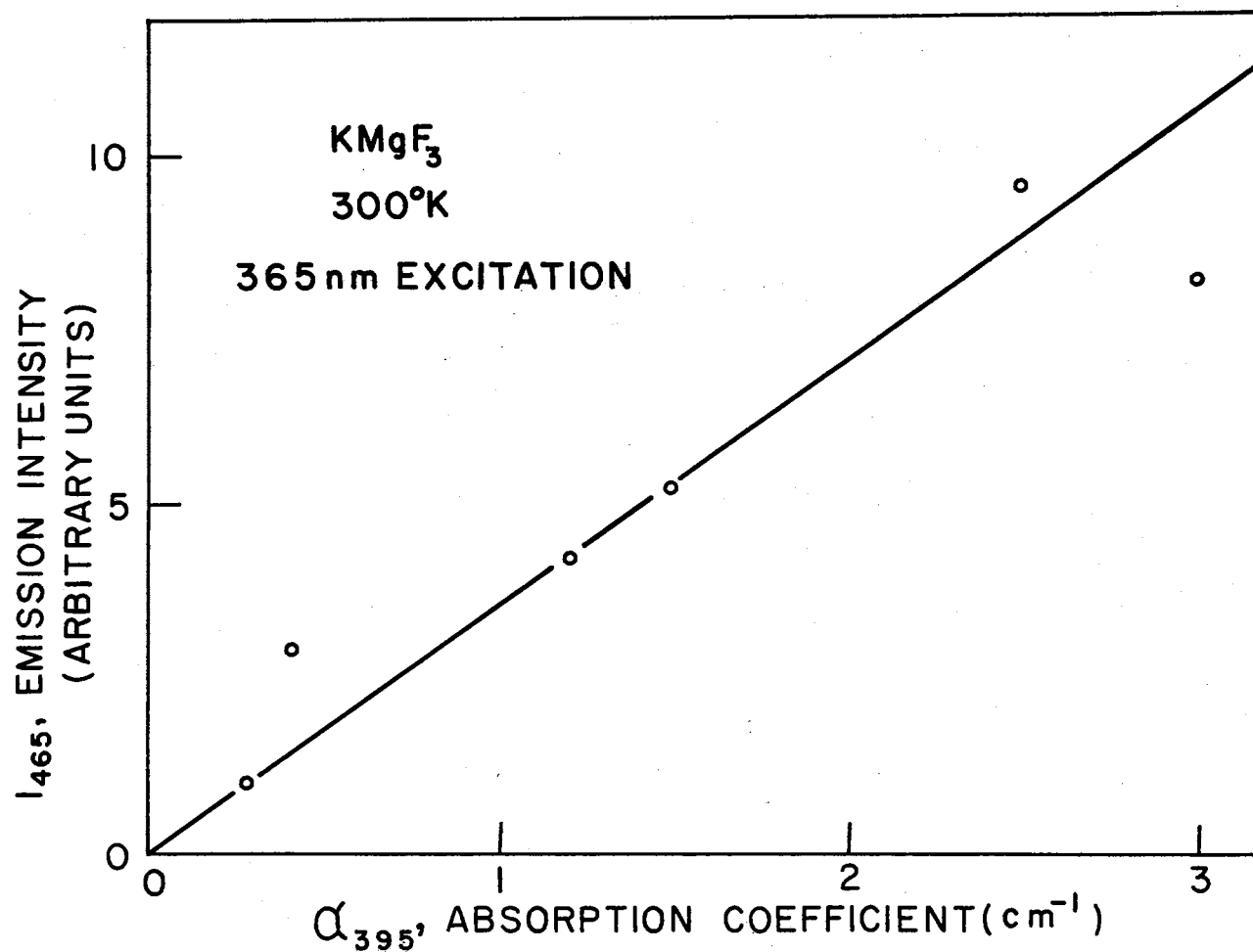


Figure 17. Emission Intensity at 465 nm Due to 365 nm Light Excitation as a Function of the Absorption Coefficient at 395 nm

bleach the emission at 465 nm is also polarized. These two results suggests that the 465 nm emission band is due to the F_3 centers. For final confirmation we employed the excitation spectrum technique, where the detecting monochromator is set at 465 nm and the excitation wavelength is varied. The excitation spectrum at room temperature shown in Figure 18 is obtained. Figure 19 portrays the excitation spectrum at 15°K. Inset shows the 465 nm emission band. In the excitation spectra two bands are found at 395 and 250 nm, and these bands are well matched with the anisotropic absorption data for F_3 center shown in reference 31. These excitation spectra also indicate that the 395 nm band corresponds to a σ or π_1 transition of F_3 centers while the 250 nm band is a π_2 transition of the F_3 centers. All the excitation spectra were calibrated with light sources which were used for excitations. By using the excitation spectrum technique one could separate the π_2 transition of the F_3 center which was hidden under the F band.

750 nm Emission

In preceding sections it was speculated that the 570 nm absorption band could be due to F_2^+ centers. So far, it has not been possible to orient centers responsible for the 570 nm absorption band by polarized bleaching techniques. The origin of 570 nm absorption band is still unclear. In order to illustrate that the 750 nm emission band is connected with 570 nm absorption band two experiments were performed. First, the emission intensity of the band was measured as a function of the absorption coefficient at the peak of the 570 nm absorption band. The results are illustrated in Figure 20 and the straight-line relationship suggests that the 750 nm emission band is due to the centers which

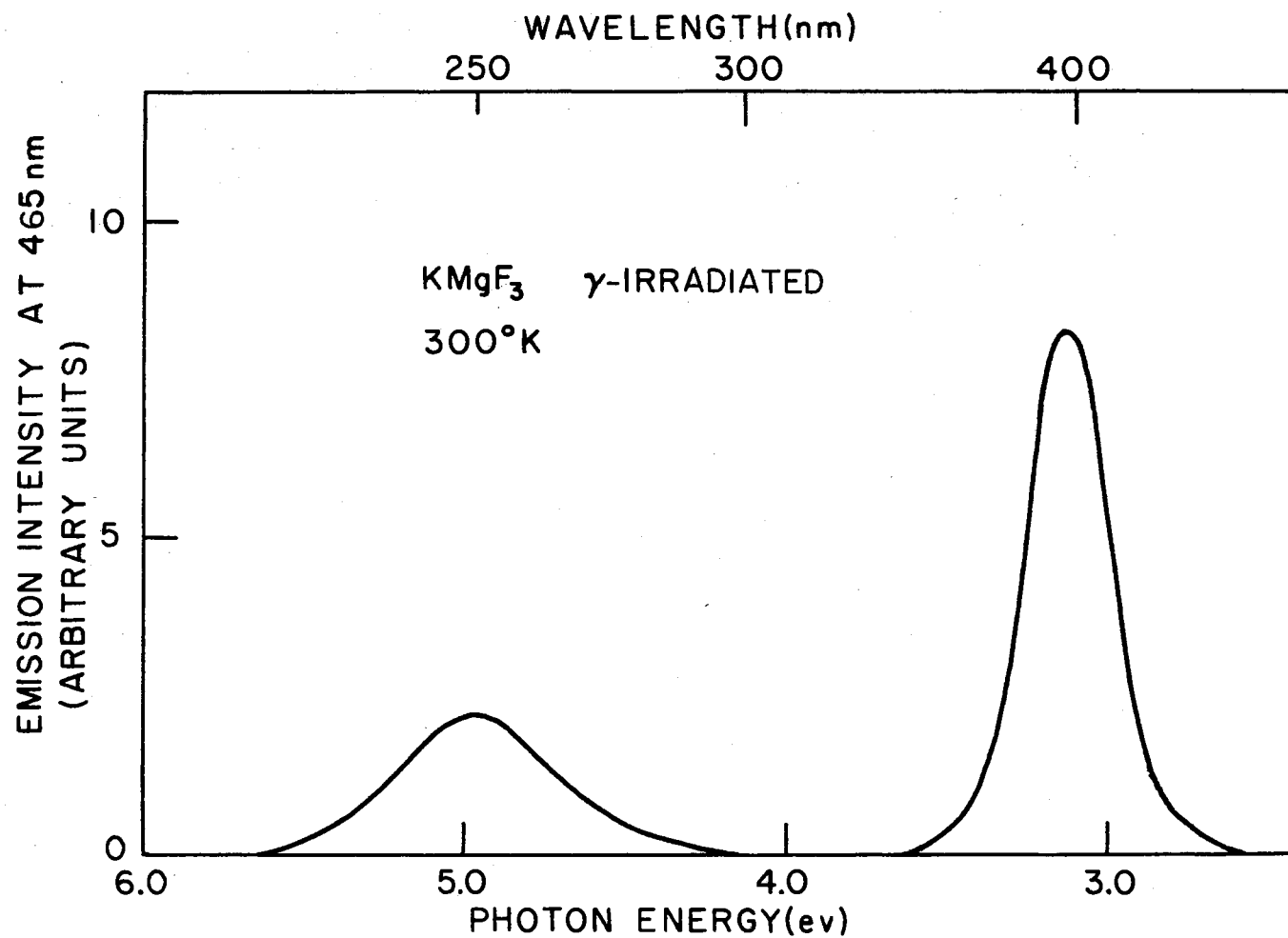


Figure 18. Excitation Spectrum for 465 nm (F_3) Emission Band in KMgF_3 at 300°K

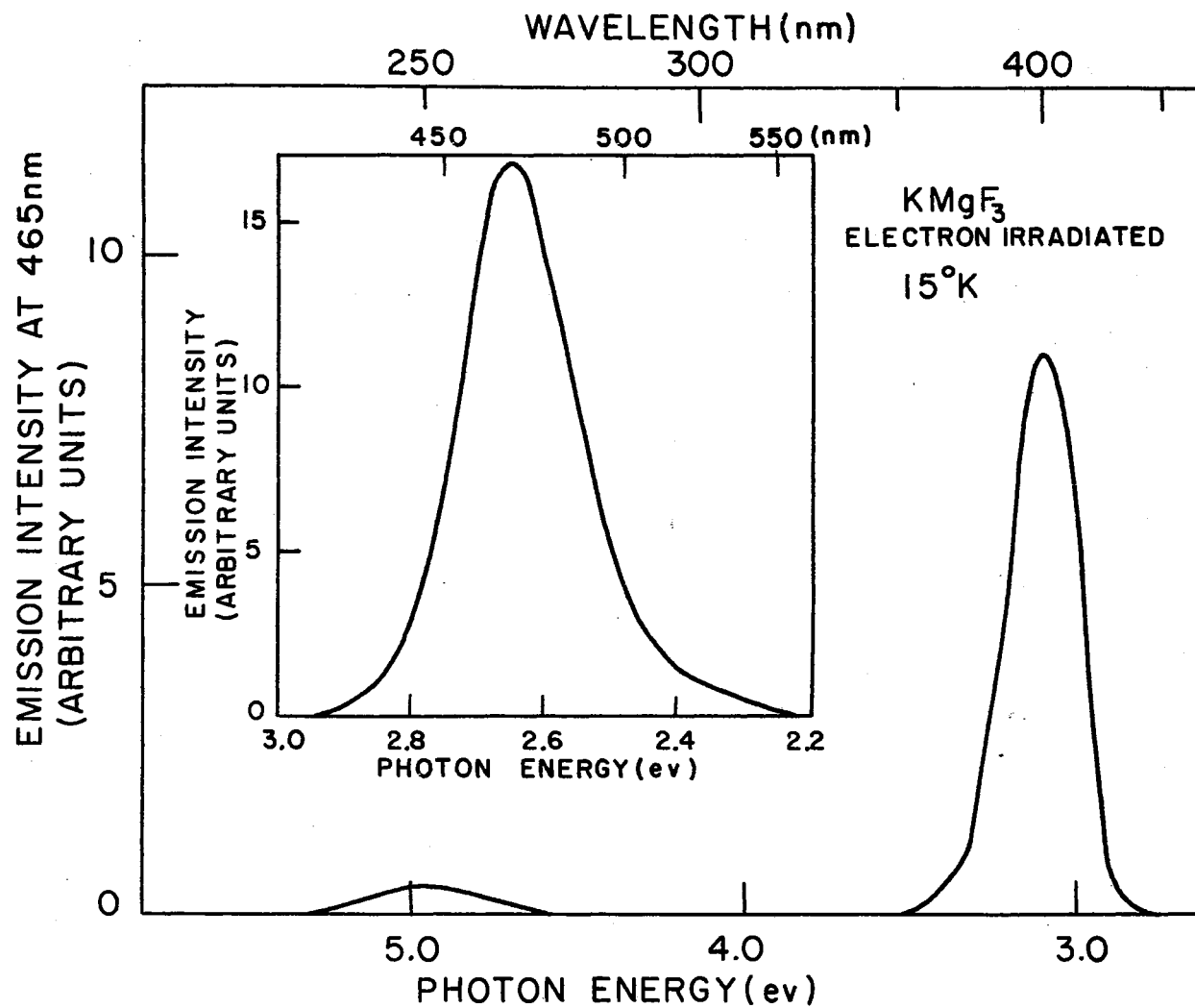


Figure 19. Excitation Spectrum and 465 nm (F_3) Emission Band in $KMgF_3$ at 15°K

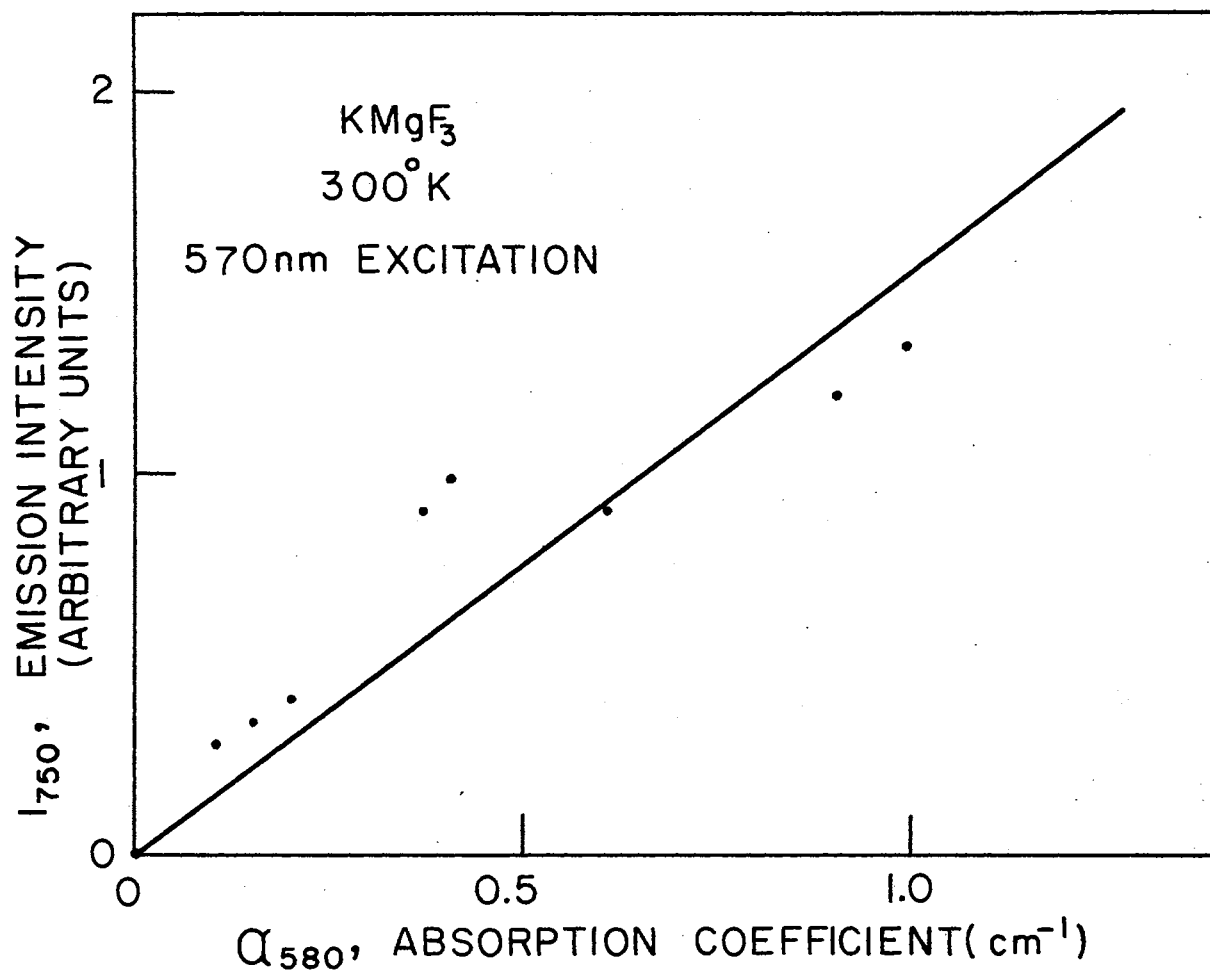


Figure 20. Plot of the Emission Intensity at 750 nm Due to 580 nm Light Excitation Versus the Absorption Coefficient at 570 nm

absorb light at 570 nm. The second study dealt with the excitation spectrum of 750 nm emission band. The excitation spectrum for 750 nm band is shown in Figure 21. Inset shows the 750 nm emission band. In the excitation spectrum we find a band at 570 nm. Gaussian plot for the 750 nm emission band at 300°K is portrayed in Figure 22. The variation with temperature of the half-width and the peak position ϵ_{\max}^E for the 750 nm emission band is shown in Figure 23. Figure 24 shows a plot of $\coth^{-1} (W(T)/W(0))^2$ versus $1/T$. A value of the frequency of the dominant interacting phonon mode of $\omega_e = 3.67 \times 10^{13} \text{ sec}^{-1}$ is obtained from the slope of the line in Figure 24 and Equation (78). A value of $S \approx 10.5$ is obtained. A zero-phonon line corresponding to the 750 nm emission band has not been observed because of large S value.

Other Emission Bands

When a sample of irradiated KMgF_3 is excited with light of wavelengths of 270 or 570 nm two emission bands are observed. 270 nm excitation yields an 410 nm emission while 570 nm excitation gives a 650 nm emission band. The origins of these bands are not yet known. The excitation spectrum and emission spectrum of the 410 nm band are shown in Figure 25. The 410 nm emission band has a significant phonon structure. Figure 26 shows the 465, 590, and 750 nm emission bands excited by light of wavelengths 395, 445, and 570.

Absorption in $\text{KMgF}_3\text{:Mn}$ Crystal

The absorption spectrum of $\text{KMgF}_3\text{:Mn}$ (1.4 at. %) which was electron irradiated at 80°K is shown in Figure 27. Before electron irradiation no noticeable absorption bands in the range of 200 - 800 nm could be ob-

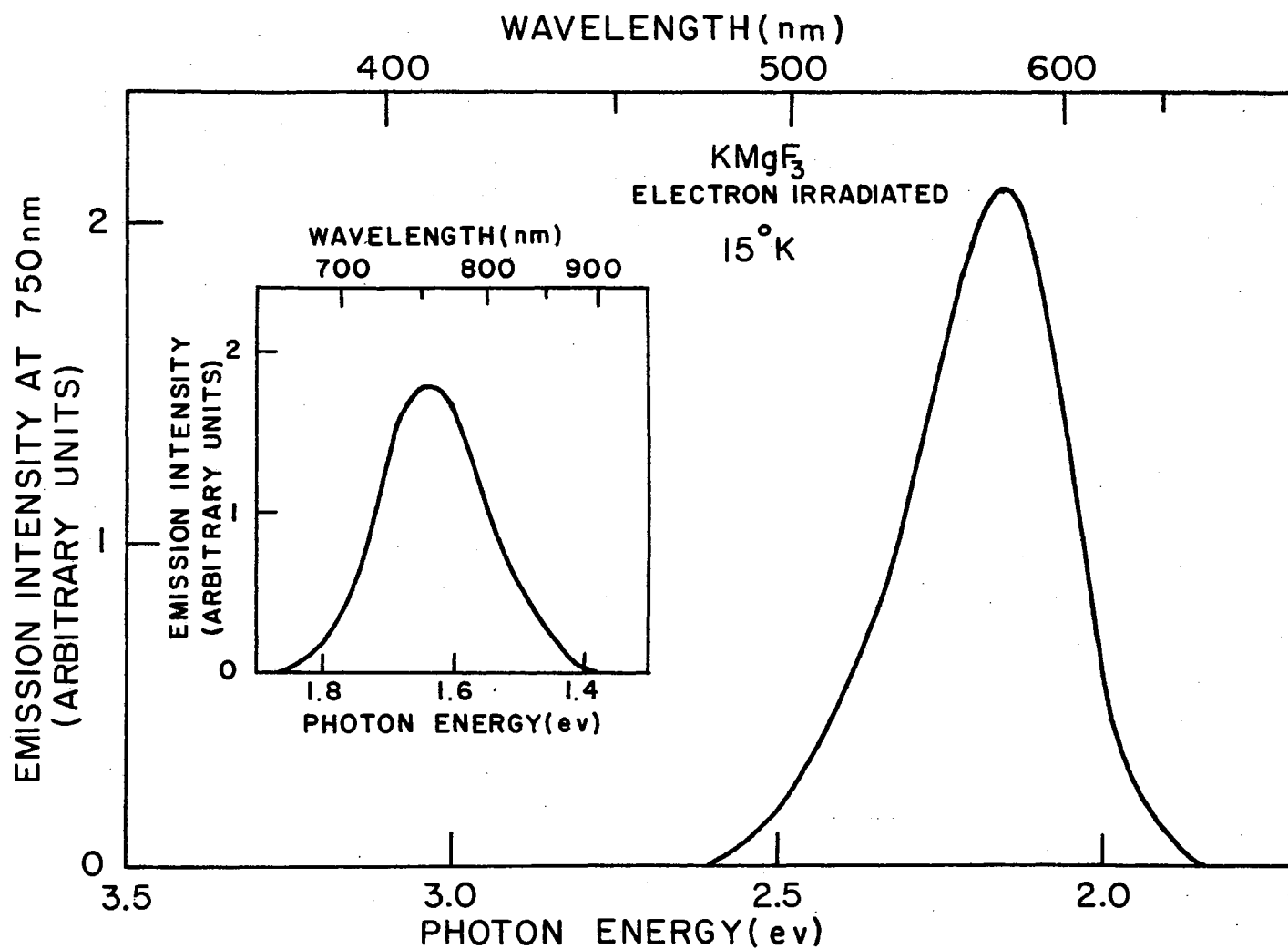


Figure 21. Excitation Spectrum and 750 nm Emission Band in KMgF_3 at 15°K

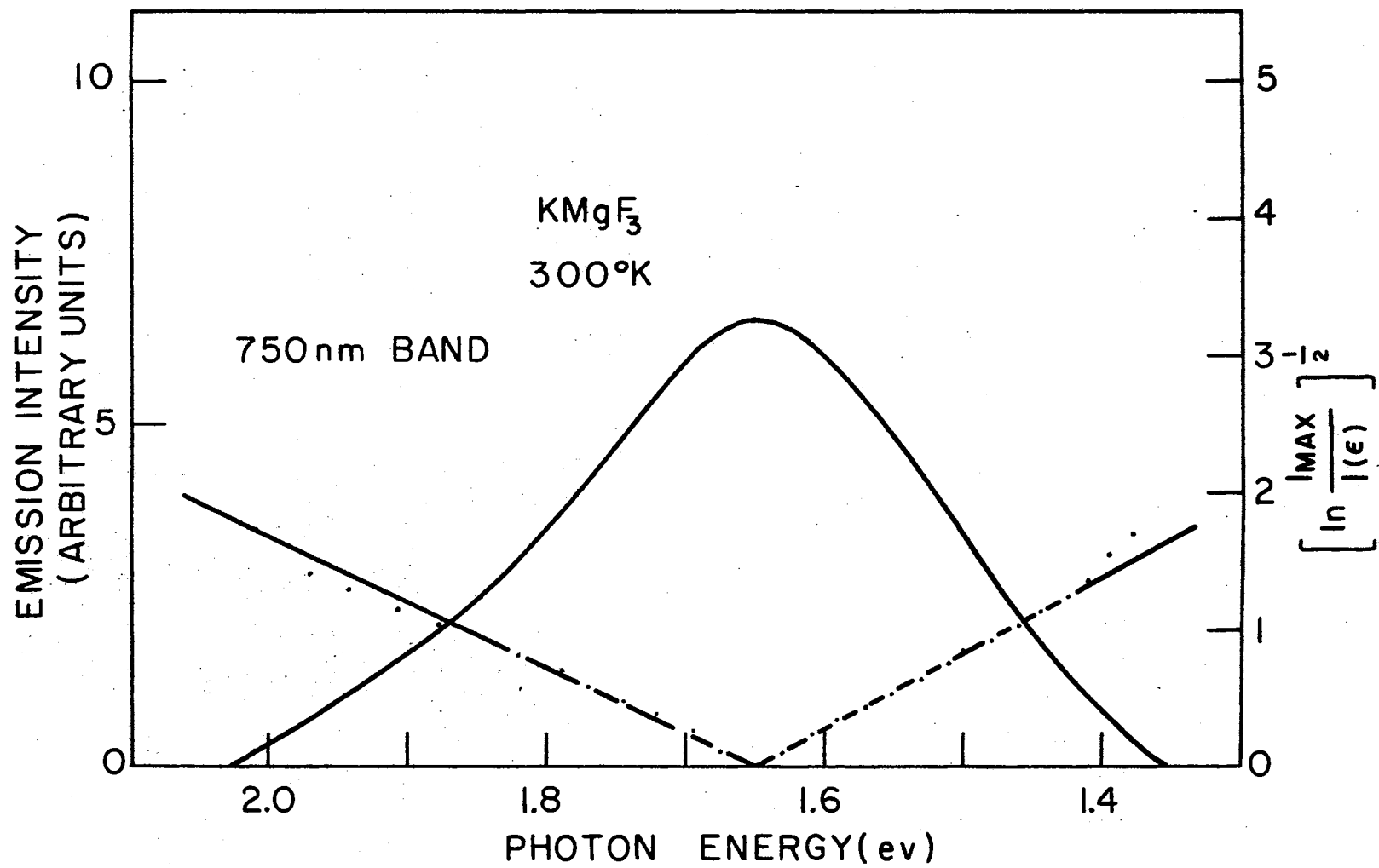


Figure 22. Gaussian Plot for 750 nm Emission Band in KMgF_3

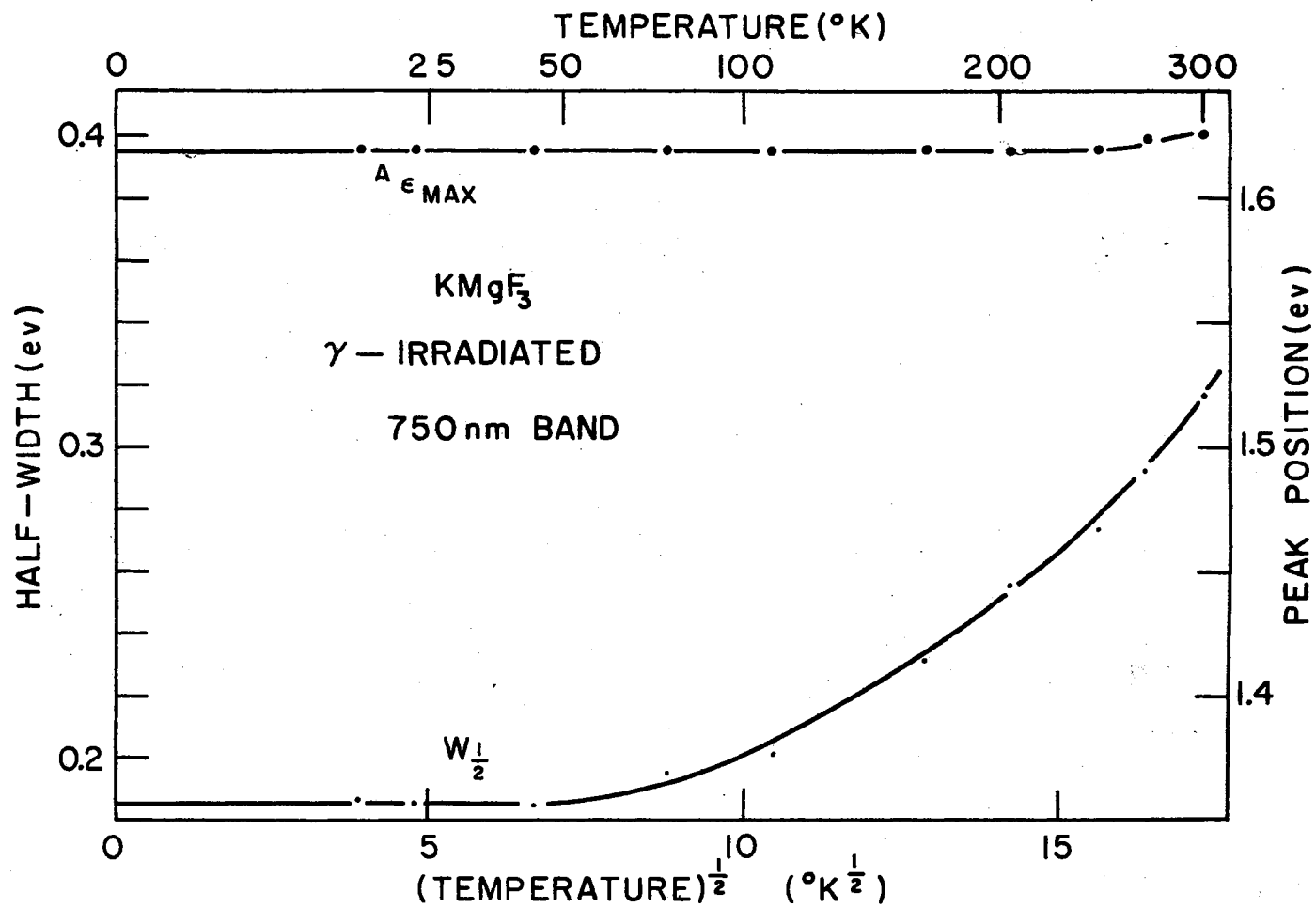


Figure 23. Temperature Dependence of $W_{1/2}$ and ϵ_{max}^A for 750 nm Emission Band in KMgF_3

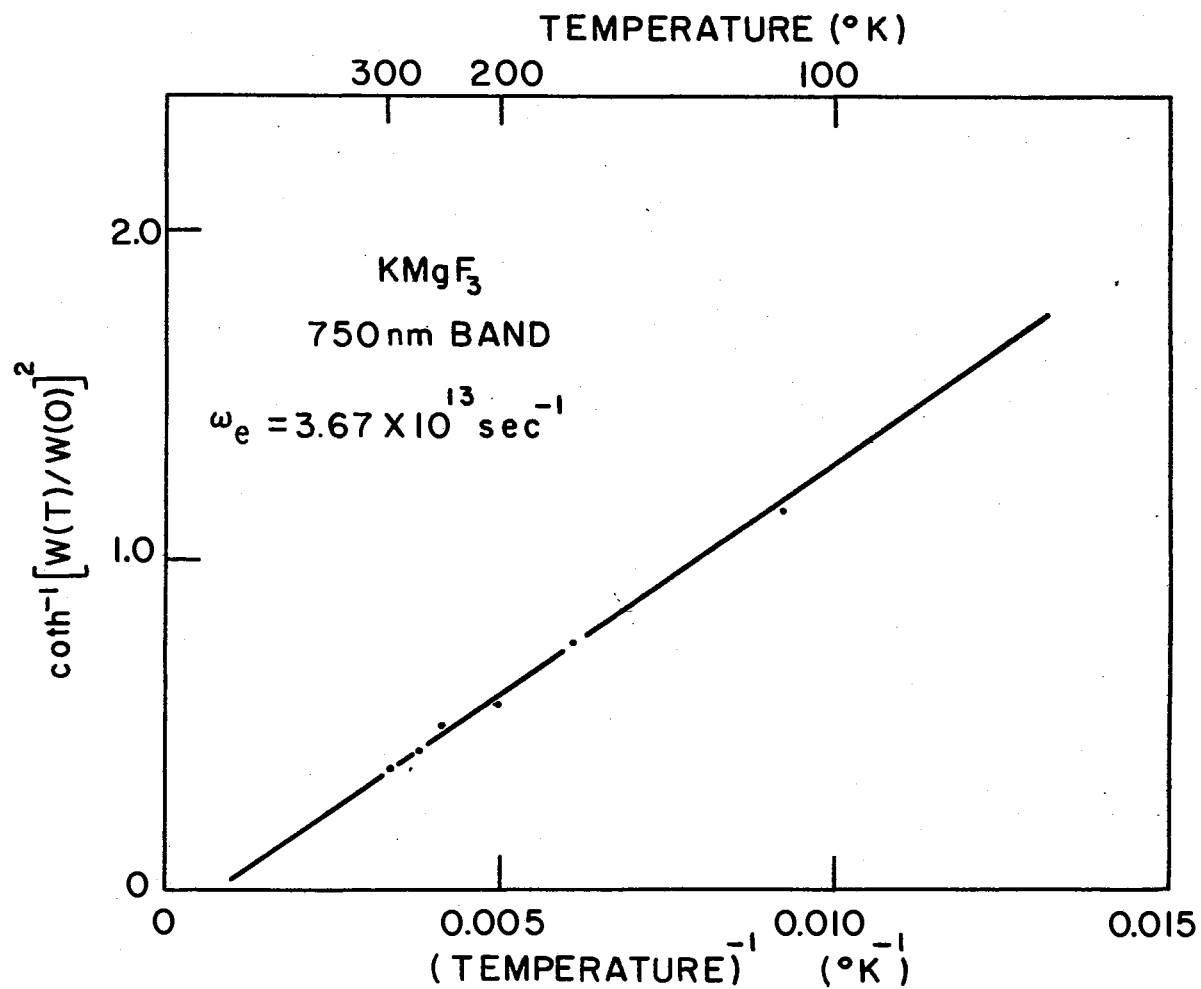


Figure 24. Temperature Dependence of Half-Width of 750 nm Emission Band in KMgF₃

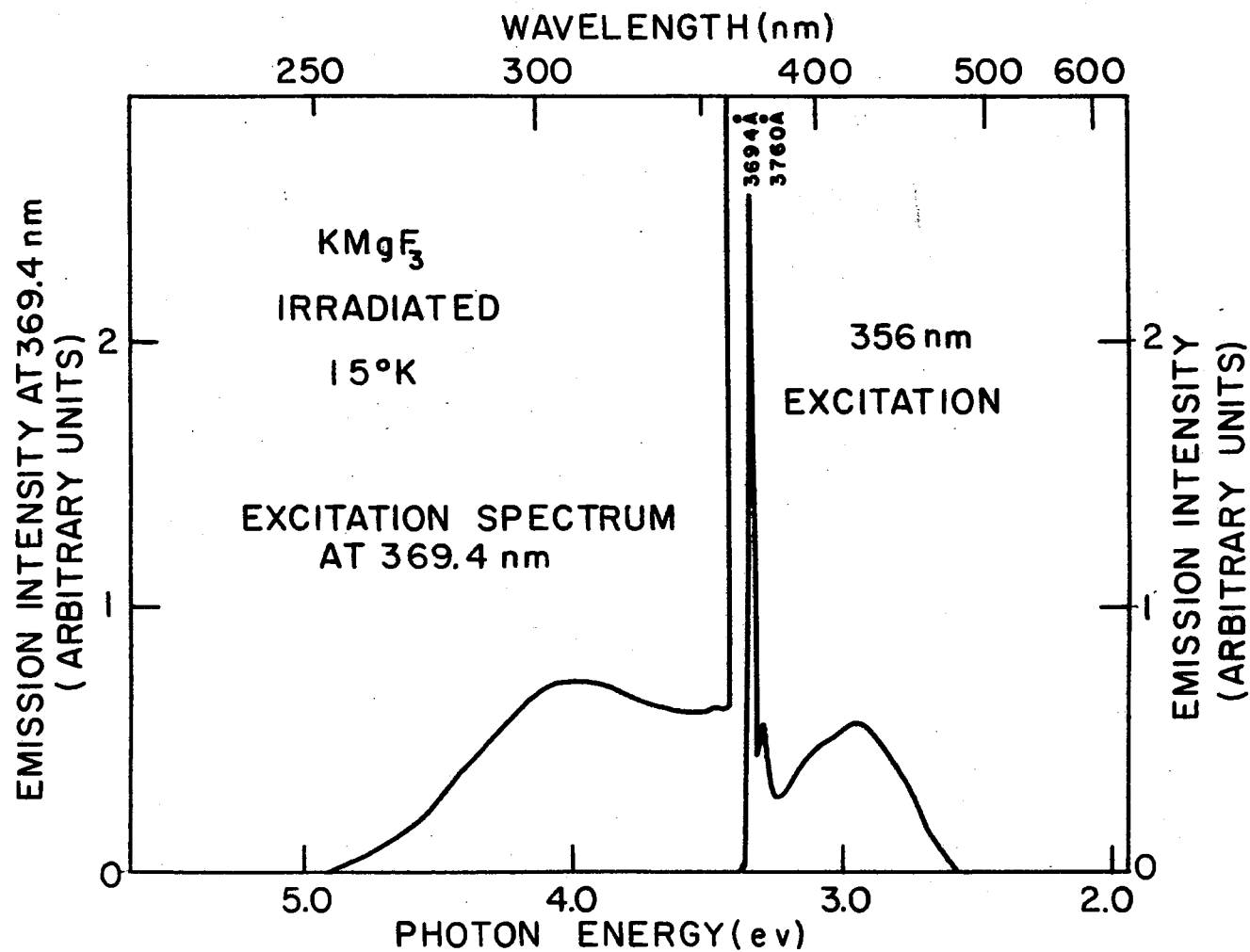


Figure 25. Excitation Spectrum and 410 nm Emission Band in KMgF_3 at 15°K

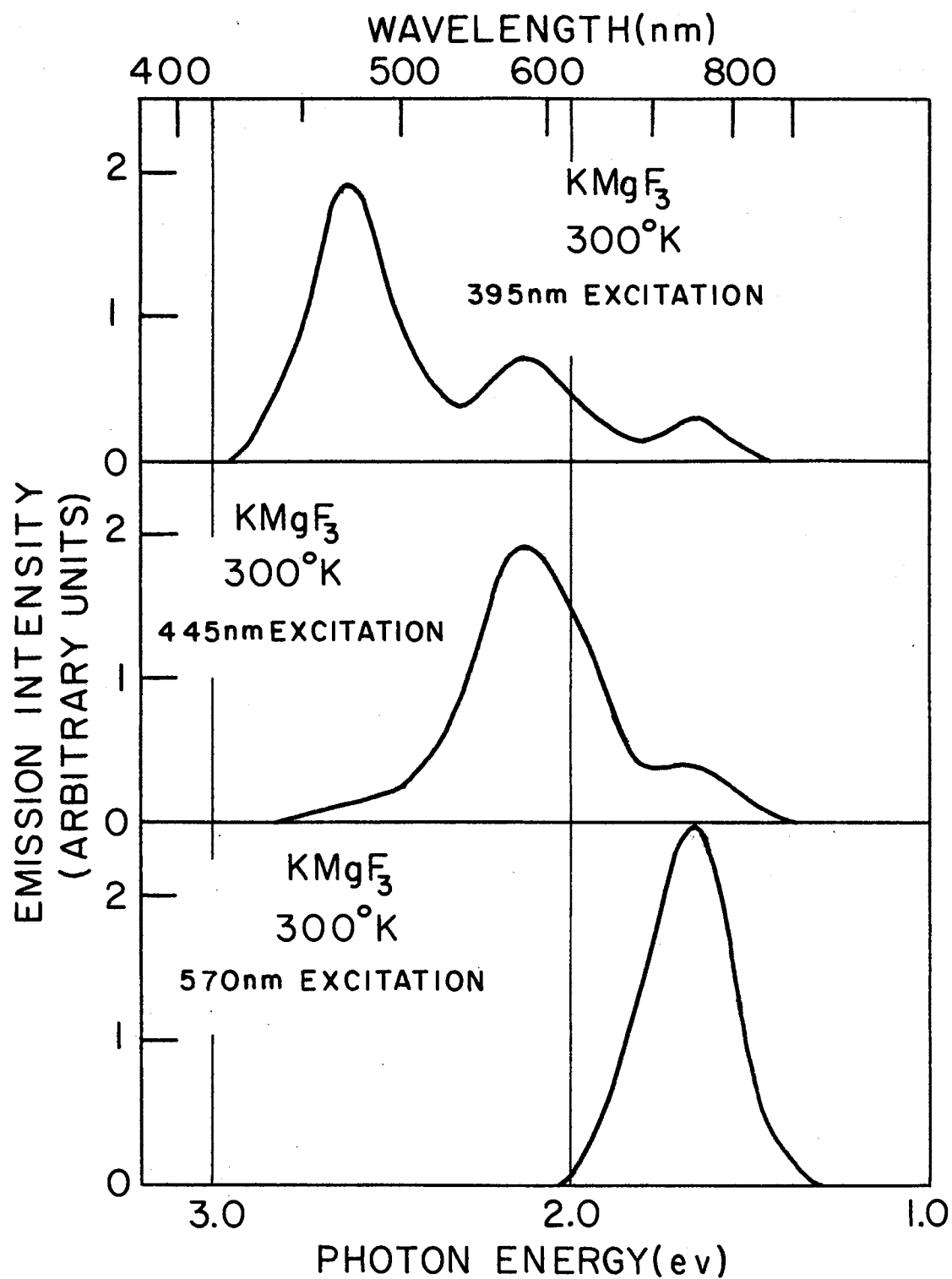


Figure 26. 465, 590, and 750 nm Emission Bands Excited by Light of Wavelength 395, 445, and 570 nm at 300°K

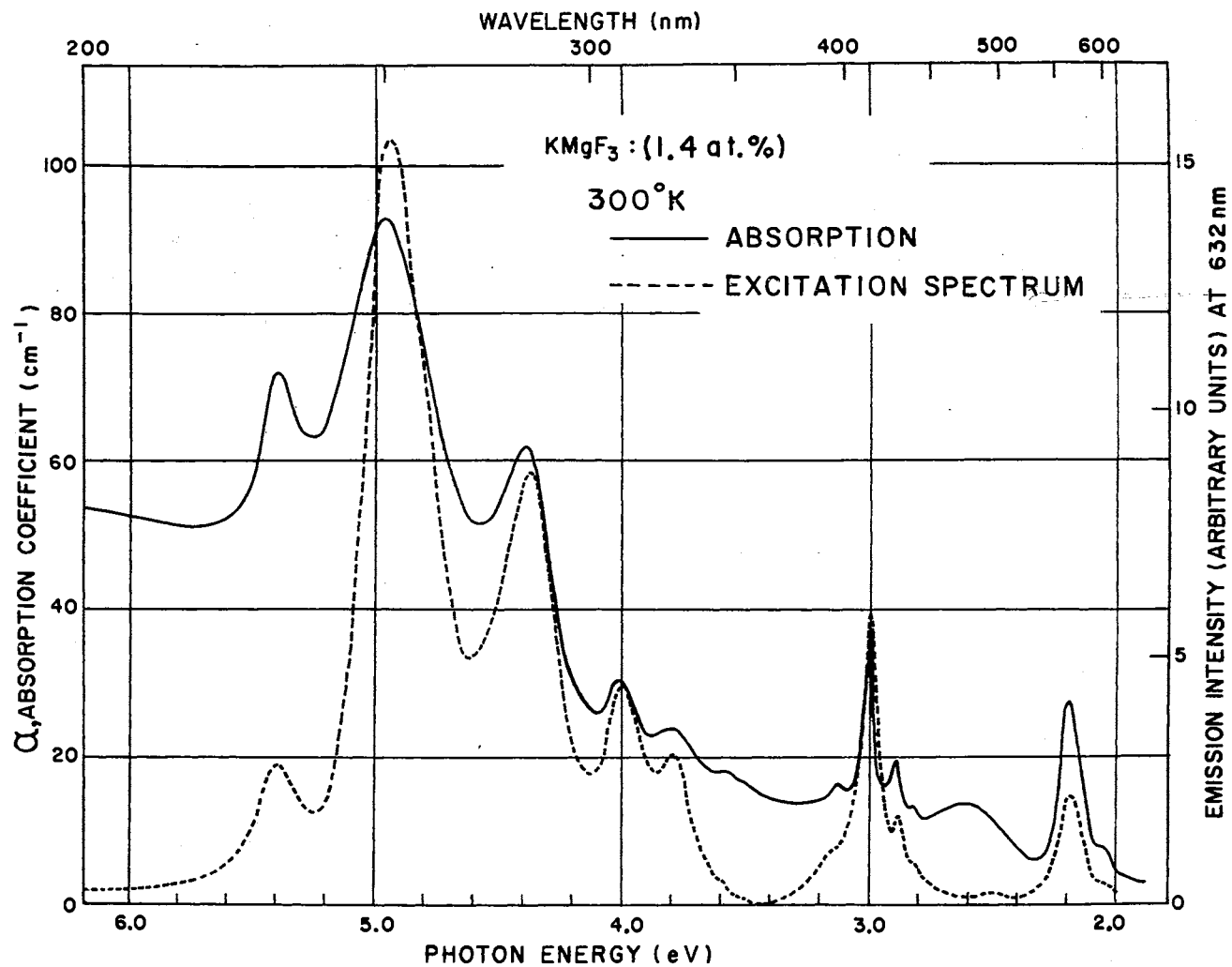


Figure 27. Absorption Spectrum and Excitation Spectrum of KMgF₃:Mn (1.4 at. %) at 300°K Following an Electron Irradiation at 80°K

served. KMgF_3 crystals containing various amounts of Mn^{2+} (0.04 - 91.2 at. %) after electron irradiation at 80°K show similar spectra and the absorption coefficients are apparently related to the concentration of Mn^{2+} ion pairs (\sim square of concentration of Mn^{2+}). The concentrations of Mn-ion pairs were calculated from the probability of having double clusters in a system containing single type of impurity under the assumption of a random distribution^(89,90). A comparison of these spectra with the ones obtained for KMnF_3 ⁽³⁵⁾, RbMnF_3 ⁽³⁶⁾, NaMnF_3 ⁽³⁷⁾, and MnF_2 ⁽³⁸⁾ reveals that the absorption bands can be attributed to Mn^{2+} ions in KMgF_3 crystals. The absorption spectrum of KMnF_3 at 300°K is shown in Figure 28. Vehse and Sibley⁽³⁰⁾ proposed that these absorption bands in $\text{KMgF}_3\text{:Mn}$ arise from a defect involving an F center trapped between adjacent Mn impurity ions, i.e., the observed optical absorption bands are assigned to Mn-pair 3d electron transitions perturbed by the presence of the F center between two Mn^{2+} ions. We designate this defect by the symbol Mn-F-Mn. The optical absorption of irradiated $\text{KMgF}_3\text{:Mn}$ (1.4 at. %) after a room temperature optical bleach with the electric vector of the 254 nm incident light along the [100] direction is illustrated in Figure 29. The difference curve for absorption with light polarized along [010] and [100] directions is also shown in Figure 29. And there was no anisotropic absorption after bleach with [110] polarized light. These results suggest that the major dipole axis of this center is along $\langle 100 \rangle$.

At low temperature, the side bands seen in Figure 30 at 394, 427, 435 and 597 nm near the major absorption bands at 410 and 565 nm have decreased appreciably in the absorption spectra. The temperature dependence of these side bands are shown in Figure 31. The energy differ-

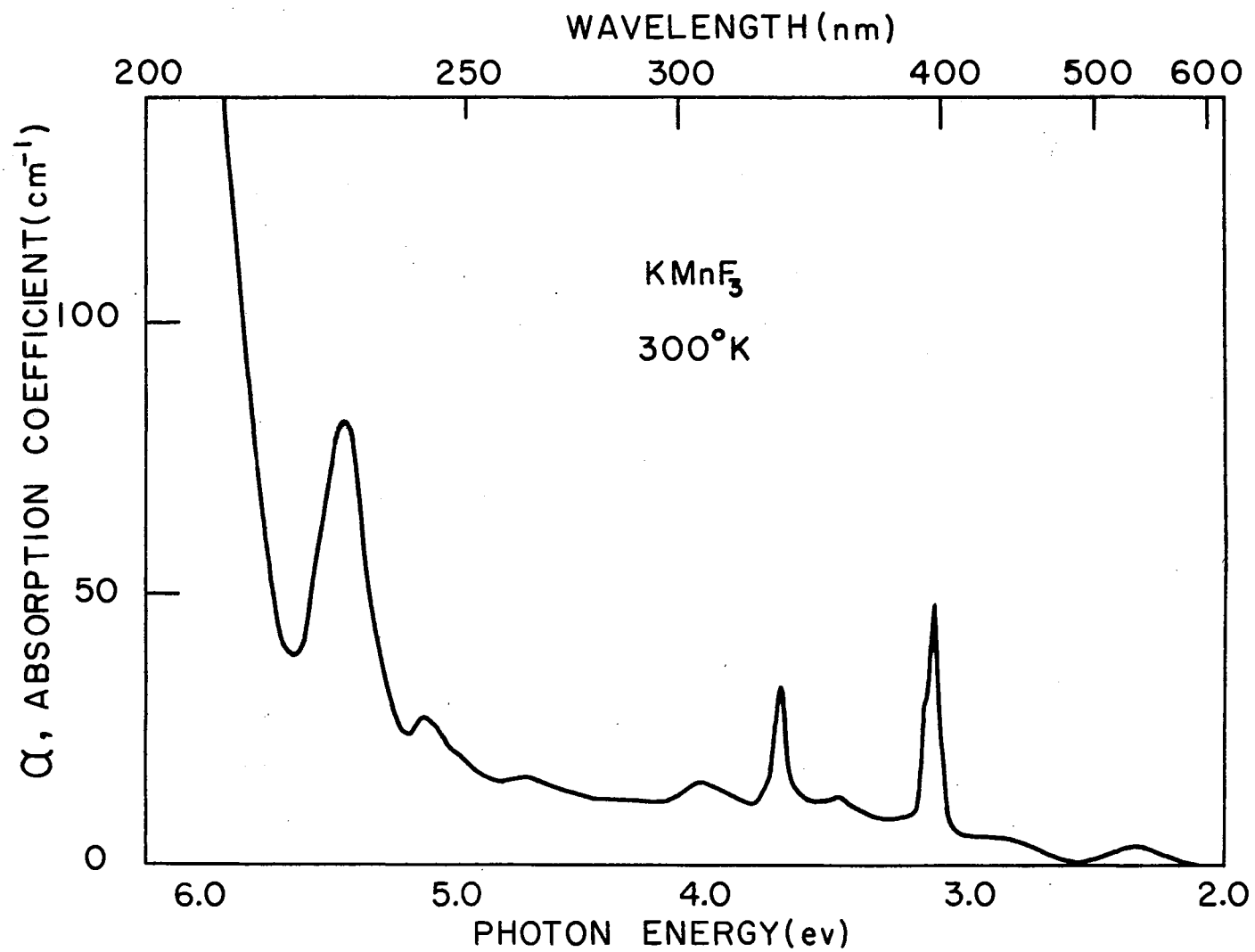


Figure 28. Absorption Spectrum of KMnF_3 at 300°K

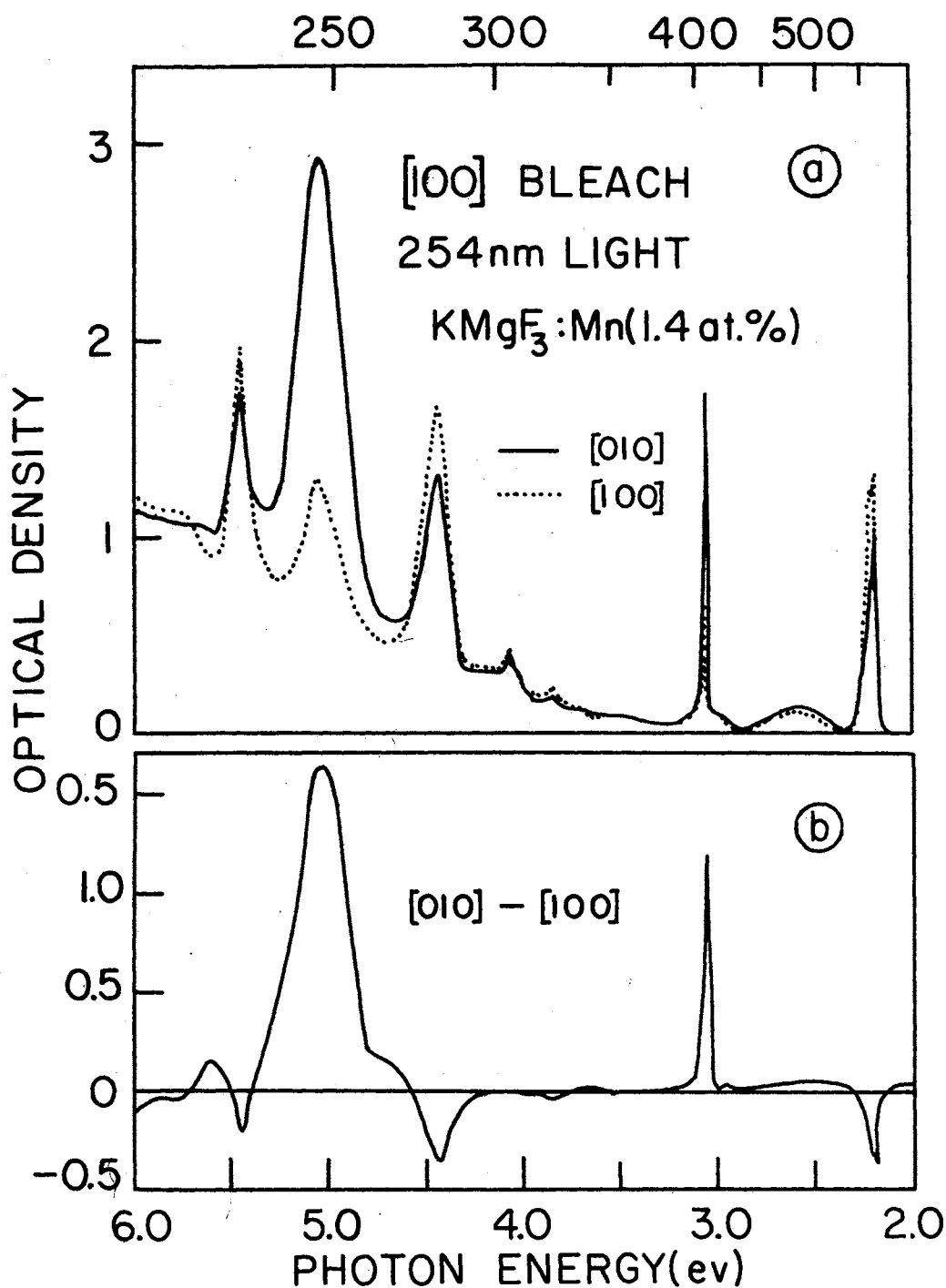


Figure 29. (a) Effect of a Room Temperature [100] Polarized Bleach on an Electron Irradiated KMgF₃:Mn (1.4 at. %) Crystal. Measuring Light Polarized Along [010] (—) and Along [100] (.....). (b) Anisotropic Absorption Curve From (a)

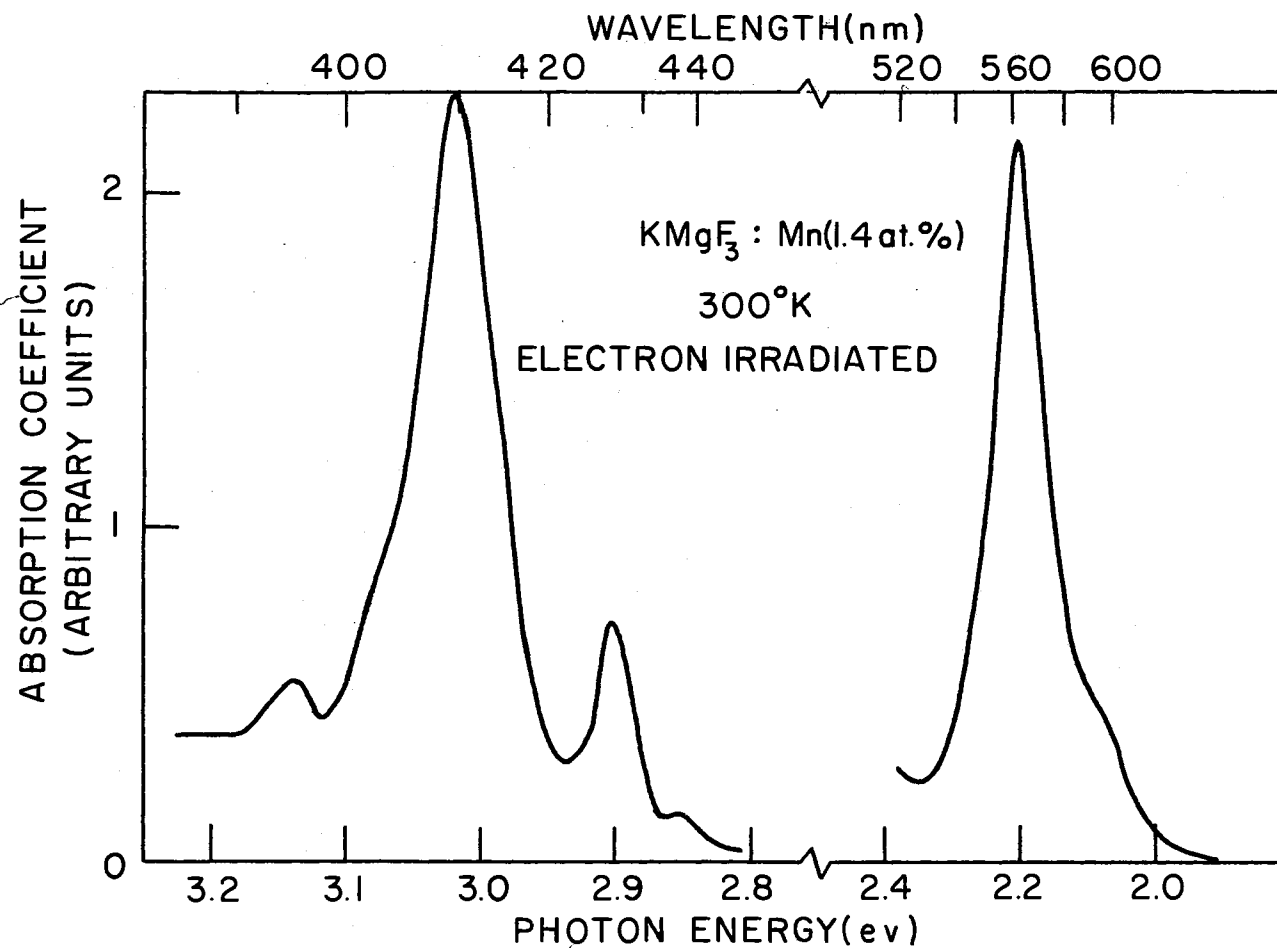


Figure 30. Side Bands at 394, 427, 435, and 597 nm Near the Major Absorption Bands at 410 and 565 nm at 300°K

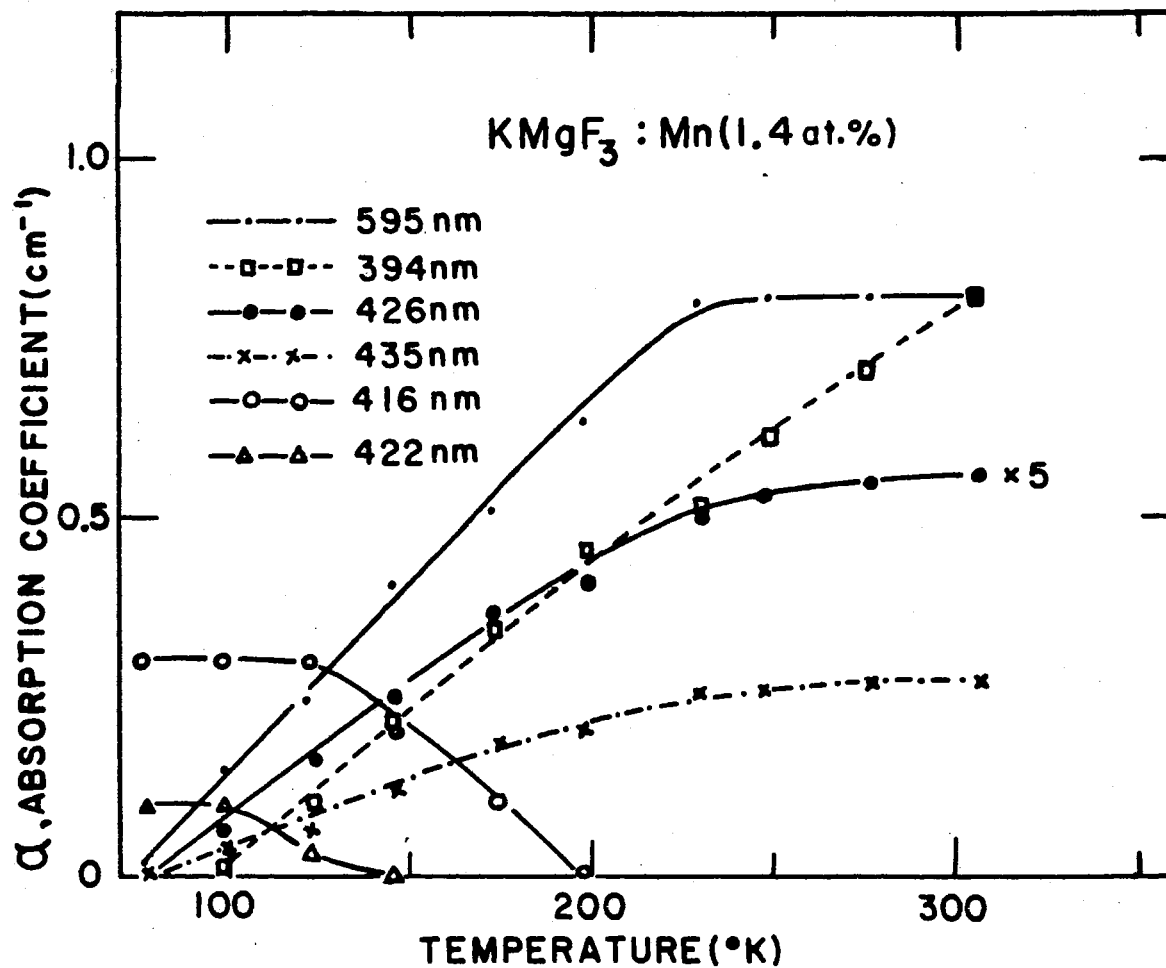


Figure 31. Temperature Dependence of Small Bands Near the Major Absorption Bands at 410 and 565 nm in an Electron Irradiated $\text{KMgF}_3:\text{Mn}$ (1.4 at. %)

ence between the major bands and the side bands appear to be about 970 cm^{-1} and 1400 cm^{-1} . If we assume that the first vibronic side band is hidden in the main absorption band, then this corresponds to an energy difference of 470 cm^{-1} for the lattice mode involved. A series of very narrow lines are also observed at low temperature on both the 410 and 565 nm absorption bands. The series of lines around 565 nm band are regularly spaced with energy differences of about 20 cm^{-1} ($2.5 \times 10^{-3} \text{ eV}$). The lines near the 410 nm band are essentially equally spaced as shown in Table VI. Observed oscillator strengths and peak positions for each bands are listed in Table VII. Figure 32 shows the absorption spectrum of 0.4 and 0.04 at. % Mn-doped KMgF_3 which were electron irradiated at 80°K . There are no F-aggregate center bands in Figure 32. Optical bleaching of $\text{KMgF}_3:\text{Mn}$ (0.04 at. %) in the F band region at room temperature converts the F centers to F_2 and higher-aggregate centers. A very weak conversion of F centers to F-aggregate centers was observed in $\text{KMgF}_3:\text{Mn}$ (0.4 at. %), but none for the $\text{KMgF}_3:\text{Mn}$ (1.4 at. %). This means that for the KMgF_3 with high concentration of Mn, the conversion of F centers to F-aggregate centers was suppressed by conversion to Mn-F-Mn defects. This is consistent with the probability of Mn^{2+} pair production in KMgF_3 , since the probability of Mn-pair production is roughly proportional to the square of the concentration of Mn ions in KMgF_3 crystal^(89,90) and the concentration of Mn^{2+} pairs exceeds the F center concentration in an irradiated $\text{KMgF}_3:\text{Mn}$ (1.4 at. %). Table VII illustrates the absorption energies for the various Mn^{2+} transitions in KMnF_3 , $\text{KMgF}_3:\text{Mn}$, and an irradiated $\text{KMgF}_3:\text{Mn}$. It should be noted that the oscillator strengths we calculate for the KMnF_3 transitions are within reasonable (25%) agreement with those of Ferguson et al.

TABLE VI
THE SPACING OF THE LINES BOTH IN EMISSION AND ABSORPTION AT LHeT

677 nm Emission			410 Absorption			565 nm Absorption		
Peak Position		Spacing	Peak Position		Spacing	Peak Position		Spacing
cm^{-1}	(nm)	cm^{-1}	cm^{-1}	(nm)	cm^{-1}	cm^{-1}	(nm)	cm^{-1}
15,576	(642.0)		23,408	(427.2)		17,565	(569.30)	
		120			132			17.6
15,456	(647.0)		23,540	(424.8)		17,583	(568.73)	
		165			129			18.0
15,291	(654.0)		23,669	(422.5)		17,601	(568.15)	
		116			118			17.0
15,175	(659.0)		23,789	(420.4)		17,618	(567.60)	
		171			131			17.1
15,004	(666.5)		23,917	(418.1)		17,635	(567.05)	
		112			149			17.2
14,892	(671.5)		24,067	(415.5)		17,652	(566.50)	
		132			117			17.1
14,760	(677.5)		24,184	(413.5)		17,669	(565.95)	

TABLE VII

ASSIGNMENT OF Mn^{2+} TRANSITIONS IN $\text{KMgF}_3:\text{KMnF}_3$ AND AN ELECTRON IRRADIATED $\text{KMgF}_3:\text{Mn}$

Assignment (O_h) $6A_{1g}$	KMnF_3 77°K			$\text{KMnF}_3:\text{Mg}$ (9.8-at.%) 77°K			$\text{KMnF}_3:\text{Mg}$ (71-at.%) 77°K			$\text{KMgF}_3:\text{Mn}$ (1.4-at.%) e-irradiated 77°K			Assignment (C_{4v}) $6A_1 +$
	nm	(cm^{-1})	(10^{-7})	nm	(cm^{-1})	(10^{-7})	nm	(cm^{-1})	(10^{-7})	nm	(cm^{-1})	(10^{-7})	
$4T_{1g} (^4G)$	554.0 539.0 527.0	(18,051) (18,553) (18,975)	3.3	532.0	(18,797)	3.5				565.0 563.0	(17,699) (17,762)	3.7×10^5	$4A_2 + 4E$
$4T_{2g} (^4G)$	445.0 435.0 428.0	(22,472) (22,989) (23,645)		435.0	(22,989)					480.0 440.0	(20,833) (22,727)		$4B_2 + 4E$
$4E_g (^4G)$	397.0 394.0	(25,189) (25,381)		397.0 394.0	(25,189) (25,381)	11.6	398.0 396.0	(25,126) (25,253)	7.1	422.5 416.2 406.0	(23,669) (24,027) (24,631)	8.0×10^4	$4A_1 + 4B_1$
$4A_{1g} (^4G)$	390.5 387.5	(25,608) (25,806)	8.9	391.0 387.5	(25,575) (25,806)		391.5	(25,543)		404.0	(24,752)		$4A_1$
$4T_{2g} (^4D)$	359.0 356.0 352.5	(27,855) (28,090) (28,369)		359.0 356.0 353.0	(27,855) (28,090) (28,329)					352.0 344.0	(28,409) (29,070)		$4B_2 + 4E$
$4E_g (^4D)$	332.0 327.0	(30,120) (30,581)	7.1	331.5 327.0	(30,166) (30,581)	9.9	332.0 327.0	(30,120) (30,581)	8.7	332.0 323.0	(30,120) (30,960)		$4A_1 + 4B_1$
$4T_{1g} (^4P)$	307.0 303.0 269.0 265.0	(32,573) (33,003) (37,175) (37,736)		307.0 303.0 267.0	(32,573) (33,003) (37,453)					307.0 293.0 280.0	(32,573) (34,130) (35,714)		$4A_2 + 4E$
$4A_{2g} (^4F)$	242.0	(41,322)		242.0	(41,322)					258.3	(38,715)		$4B_1$
$4T_{1g} (^4F)$	238.0	(42,017)								246.0	(40,650)		$4A_2 + 4E$
$4T_{2g} (^4F)$	229.0	(43,668)		229.0	(43,668)		231.0	(43,290)		228.0	(43,860)		$4B_2 + 4E$

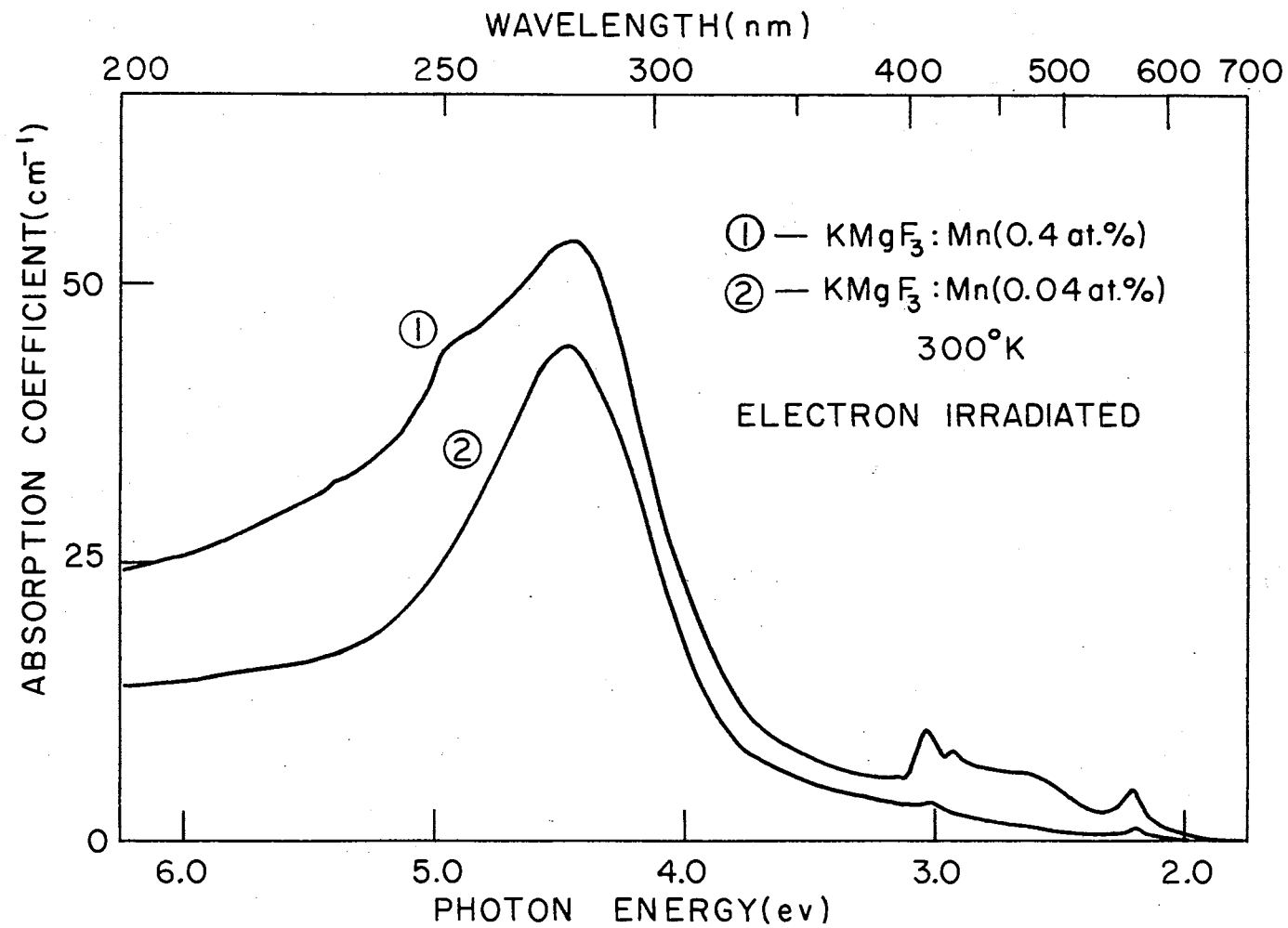


Figure 32. Absorption Spectra of 0.4 and 0.04 at. % Mn-Doped KMgF_3 Crystal Following an Electron Irradiation at 80°K

(35,45,46,58,59) and of Mehra and Venkateswarlu⁽³⁶⁾ for RbMnF_3 . To calculate the oscillator strengths for the transitions from $\text{Mn}-F-\text{Mn}$ defects we assumed that all the Mn-ion pairs have F centers between Mn-ion impurities. Since some of Mn pairs possibly do not have F centers between them the calculated oscillator strengths are the minimum oscillator strengths of $\text{Mn}-F-\text{Mn}$ defects. The oscillator strengths for the transitions from the $\text{Mn}-F-\text{Mn}$ defect are some 10^5 times as great as those in KMnF_3 . The bleaching characteristics of $\text{Mn}-F-\text{Mn}$ centers are shown in Figure 33 and indicates that all the absorption bands are due to the same type of defects. Figure 34 shows absorption spectrum of $\text{KMgF}_3:\text{Mn}$ (1.4 at. %) which was electron irradiated at 300°K . The absorption spectrum at 15°K of a 0.4 at. % Mn-doped sample which was electron irradiated at 300°K is shown in Figure 35.

In an attempt to find F_A -type centers in $\text{KMgF}_3:\text{Mn}$ we compared the absorption bands of pure KMgF_3 and $\text{KMgF}_3:\text{Mn}$ (0.04 at. %) after γ -irradiation at room temperature. The absorption bands measured immediately after irradiation show a small difference in $W_{1/2}$ of the F band. After bleaching with 254 nm light the difference in $W_{1/2}$ was much larger than before bleaching. Figure 36 shows the difference between absorption in UV region for KMgF_3 and $\text{KMgF}_3:\text{Mn}$ (0.04 at. %). Since we can not reorient this new band, it is difficult to say that the 250 nm band is due to F_A -type center. Before a definite assignment of the band more work is necessary.

Emission in $\text{KMgF}_3:\text{Mn}$ Crystals

When $\text{KMgF}_3:\text{Mn}$ crystals electron irradiated at 80°K are excited by light of wavelengths which correspond to one of the absorption bands,

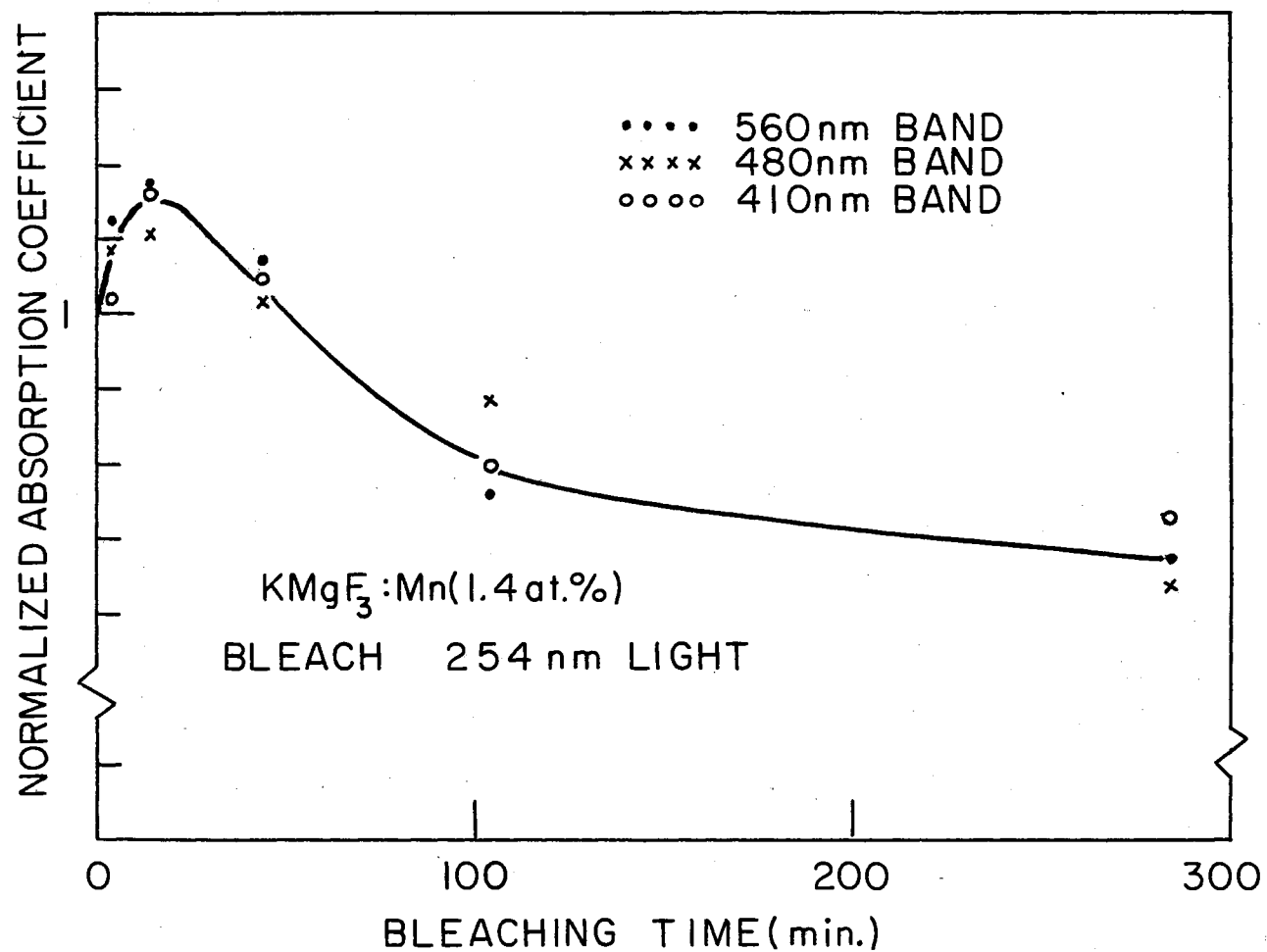


Figure 33. Optical Bleaching Curves of Absorption Bands in KMgF₃:Mn (1.4 at. %) Which was Electron Irradiation at 80°K

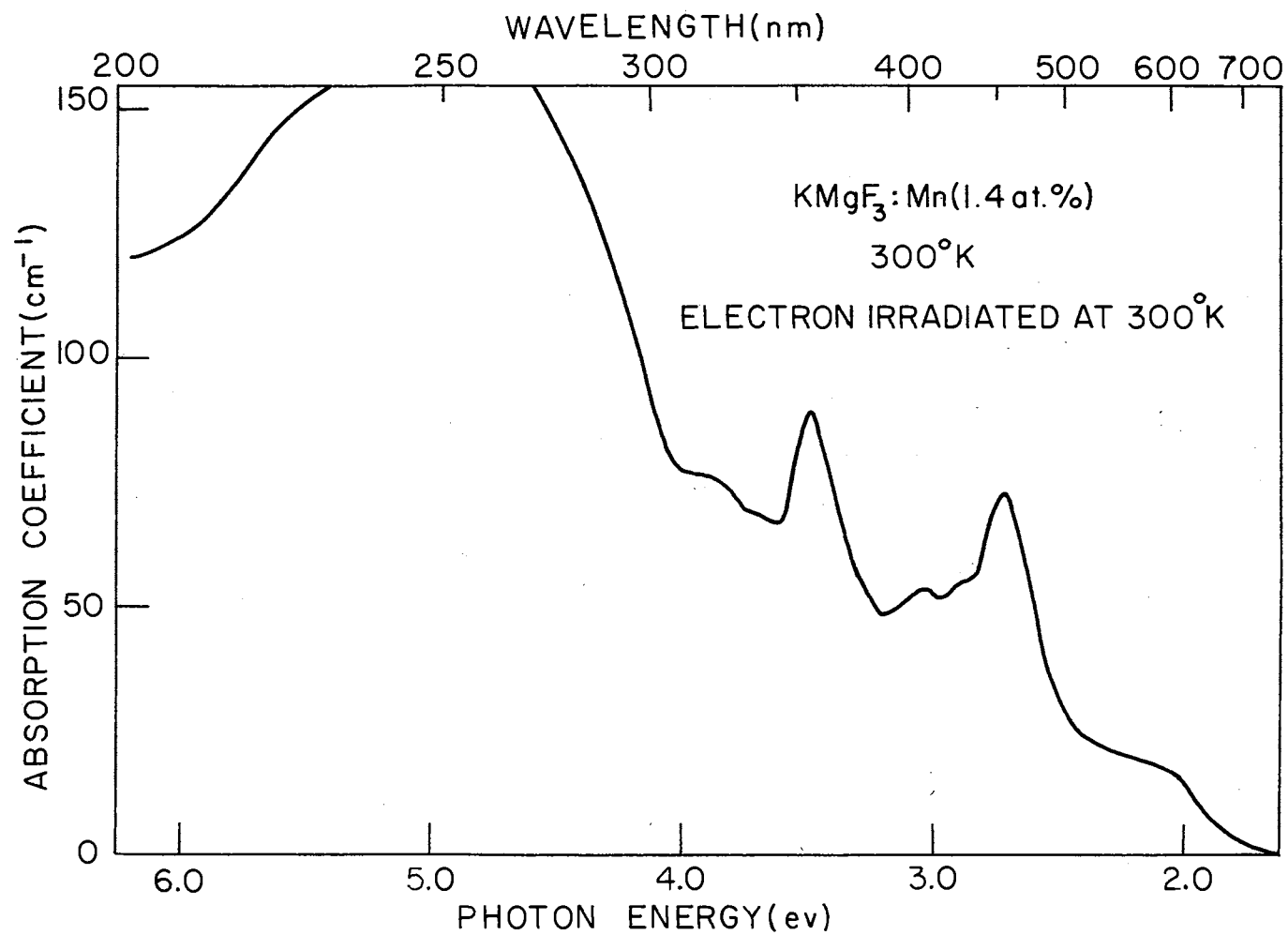


Figure 34. Absorption Spectrum of $\text{KMgF}_3:\text{Mn}$ (1.4 at. %) at 300°K Following an Electron Irradiation at 300°K

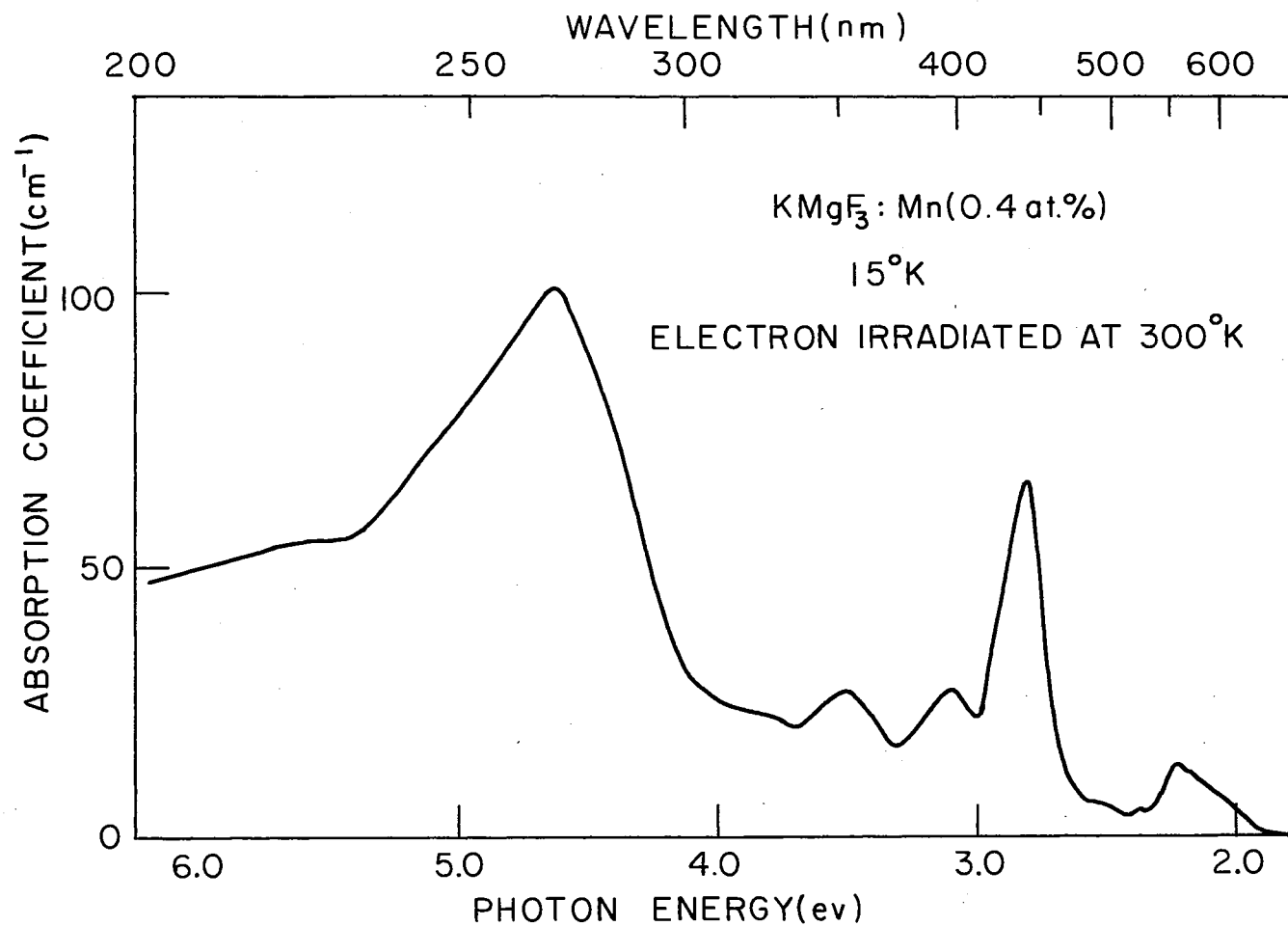


Figure 35. Absorption Spectrum at 15°K of $\text{KMgF}_3:\text{Mn}$ (1.4 at. %) Following an Electron Irradiation at 300°K

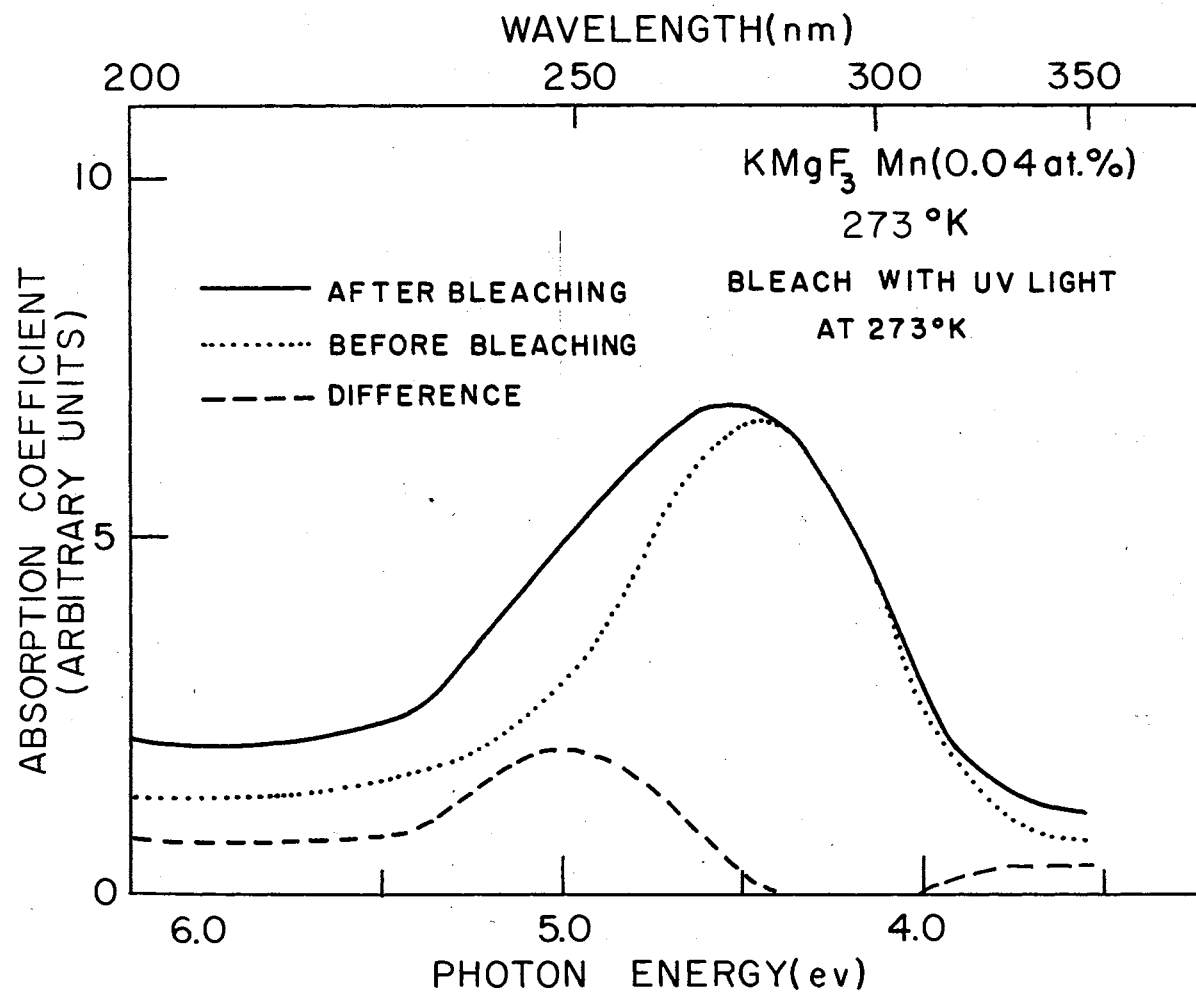


Figure 36. 250 nm Absorption Band in KMgF₃:Mn (0.04 at. %) at 273°K
After Bleach With UV Light at 273°K

the emission bands shown in Figure 37 are observed. At temperatures greater than about 170°K the band shown on the left side of the figure is dominant, whereas at low temperatures the bands portrayed on the right is seen. It is interesting that the 630 nm emission band moves to lower energy with decreasing temperature and that it is quenched at 170°K. The fine structure on the low temperature 677 nm band is evident up to about 80°K, and the lifetime of this emission is 4.8×10^{-4} seconds. This is much longer than the 16×10^{-6} seconds lifetime for the high temperature 630 nm band. When, with the sample at room temperature, the detecting monochromator is set at 630 nm and excitation wavelength is varied, the excitation spectrum shown in Figure 27 is obtained. It should be noted that much of the detail evident in the absorption spectrum is mirrored in the excitation spectrum. When the sample temperature is decreased to 77°K or below the absorption spectrum changes markedly and when the detecting monochromator is set at 677 nm, this change is also observed in the excitation spectrum. This is illustrated in Figure 38. At low temperature, the small bands seen in Figures 27, 30, and 38 at 394, 426, 435, and 595 nm near the major absorption bands at 410 and 565 nm have decreased appreciably in both the absorption and the excitation spectra. The temperature dependence of these small bands is shown in Figure 31. The low temperature emission at 677 nm exhibits fine structure as pictured in Figure 37. The narrow lines are separated by energy differences close to those observed for the 410 nm band as illustrated in Table VI. From Figure 37 we see another band at 720 nm. The excitation spectrum for 720 nm emission band is shown in Figure 39. The lifetime of this emission at 300°K is about 16×10^{-6} sec. The peak position and the intensity of the 720 nm band were very insensitive

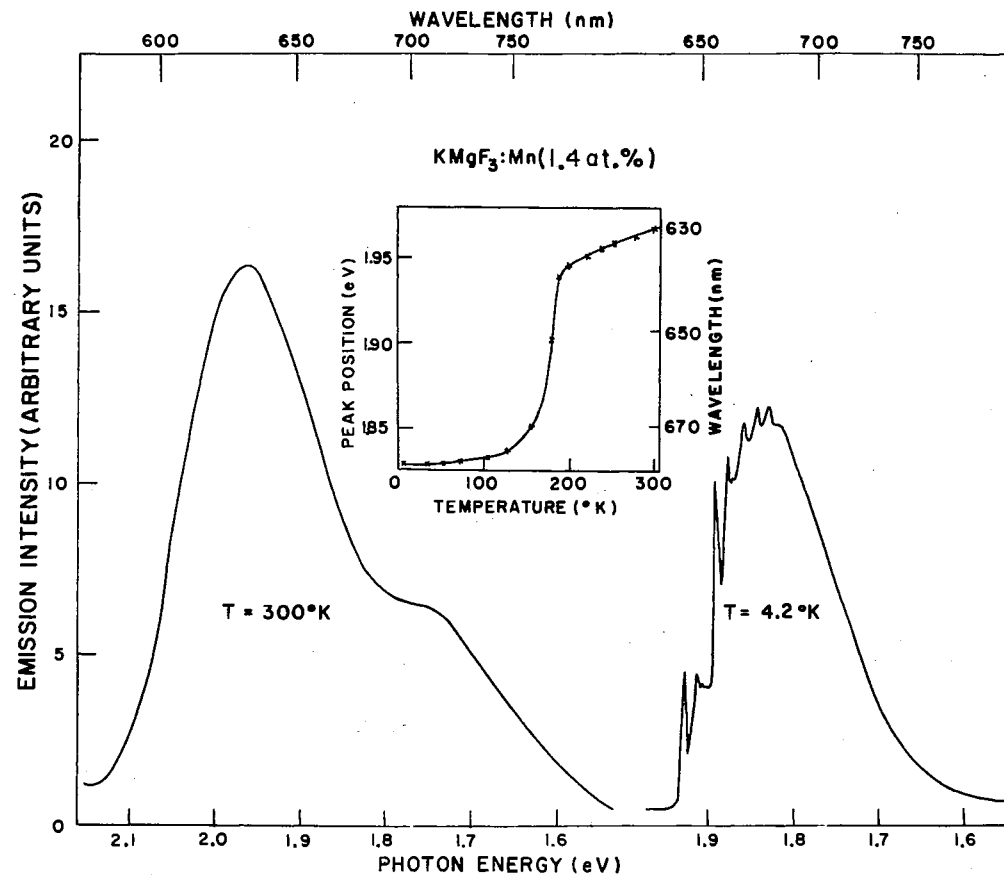


Figure 37. Emission Bands in an Electron Irradiated $\text{KMgF}_3:\text{Mn}$ (1.4 at. %). The left side of the figure is the emission band at 300°K and the right side of the figure is the emission band at 4.2°K . Inset shows the temperature dependence of the peak positions for the emission band in electron irradiated $\text{KMgF}_3:\text{Mn}$ (1.4 at. %)

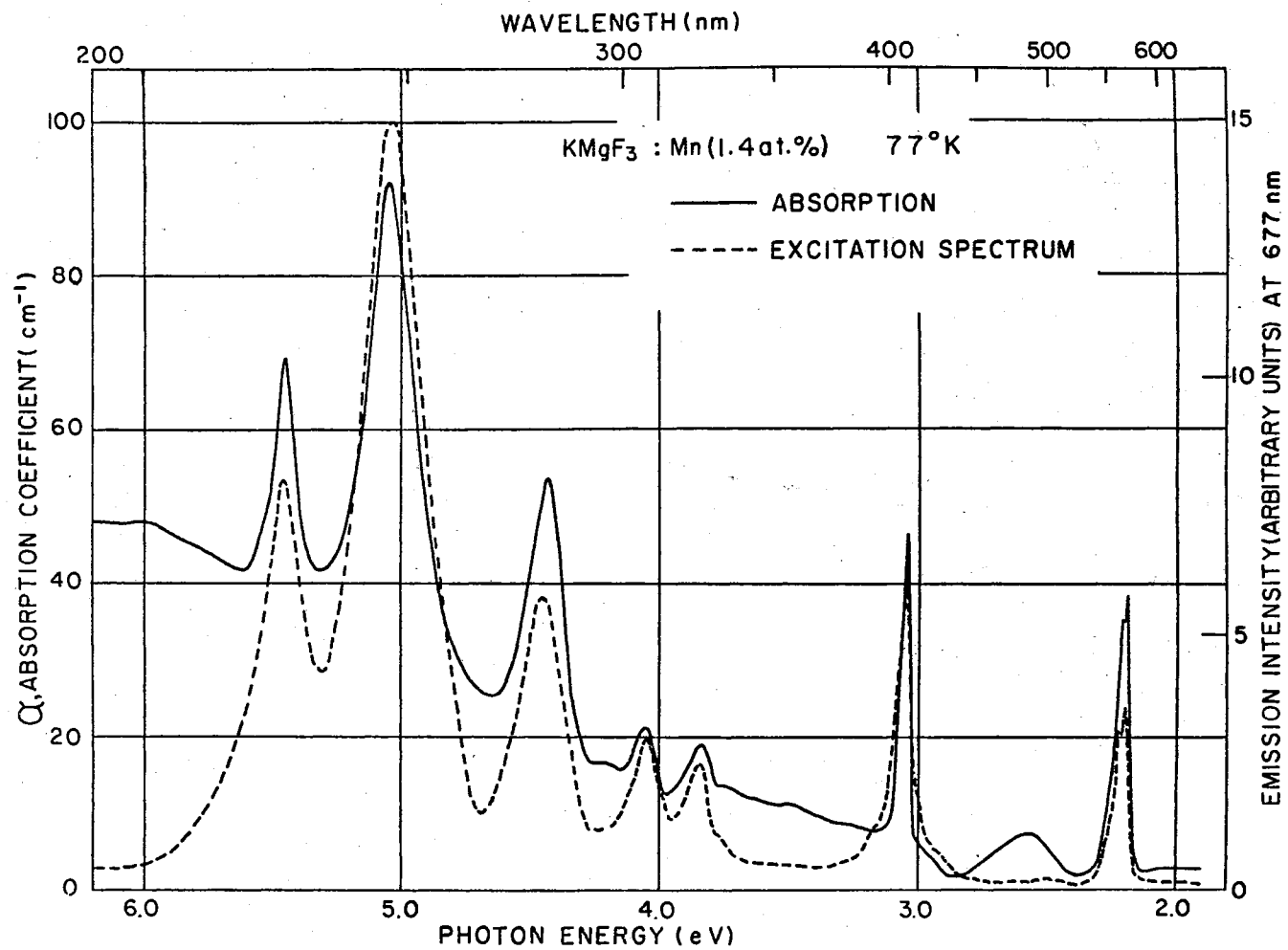


Figure 38. Absorption Spectrum and Excitation Spectrum for an Electron Irradiated KMgF₃:Mn (1.4 at. %) at 77°K

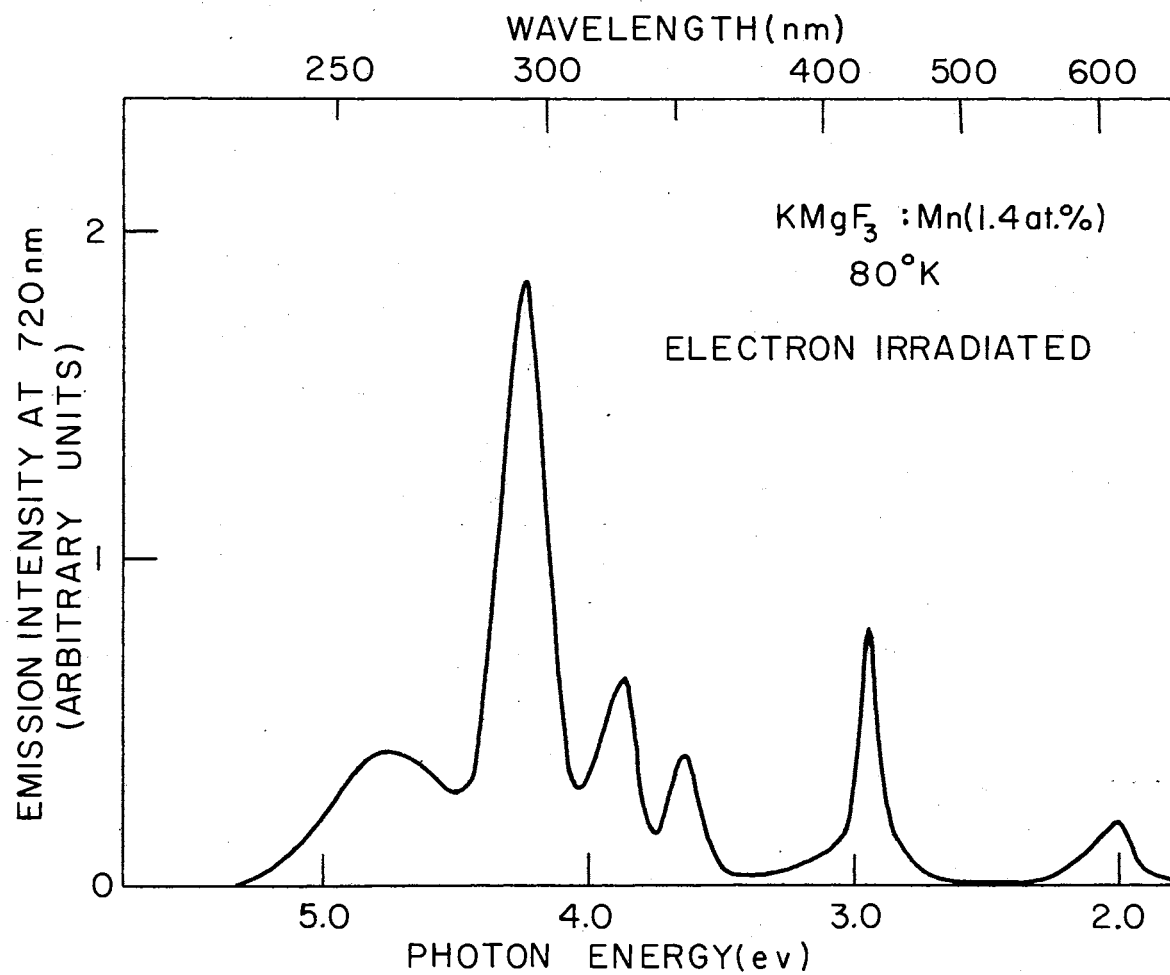


Figure 39. Excitation Spectrum for 720 nm Emission Band in an Irradiated $\text{KMgF}_3:\text{Mn}$ (1.4 at. %) at 80°K

to the temperature change. In $\text{KMgF}_3\text{:Mn}$ (0.04 at. %) it is possible to separate the 720 nm emission from the 750 nm emission band by changing the exciting light wavelength. These are shown in Figure 40.

$\text{KMgF}_3\text{:Mn}$ (0.4 at. %) which has been electron irradiated at 300°K shows quite different luminescence bands when compared with samples which have been electron irradiated at low temperature. The F, F_2 , F_3 , and 750 nm luminescence are observable in the room temperature irradiated $\text{KMgF}_3\text{:Mn}$ samples. Additional emission bands also are observed at 650, 360, and 720 nm. The 720 nm bands seen in both room temperature irradiated and 80°K irradiated sample have the same fine structure. The 650 nm band also has fine structure. The excitation spectra for the 650, 720, and 750 nm emission bands are shown in Figure 41. These 650 and 750 nm emissions have very short lifetimes (~ micro seconds) even at 15°K . Possibly the 720 and 650 nm emission bands arise from different types of Mn-color center or Mn-interstitial complexes. By comparison with absorption spectra it is found that absorption spectra in 300°K irradiated samples are not only F-aggregate bands but also complexes of bands which come from different defects. Figure 42 shows the luminescence from KMnF_3 at 15°K . The lifetime of this luminescence at 20°K was reported as 30 msec. (39)

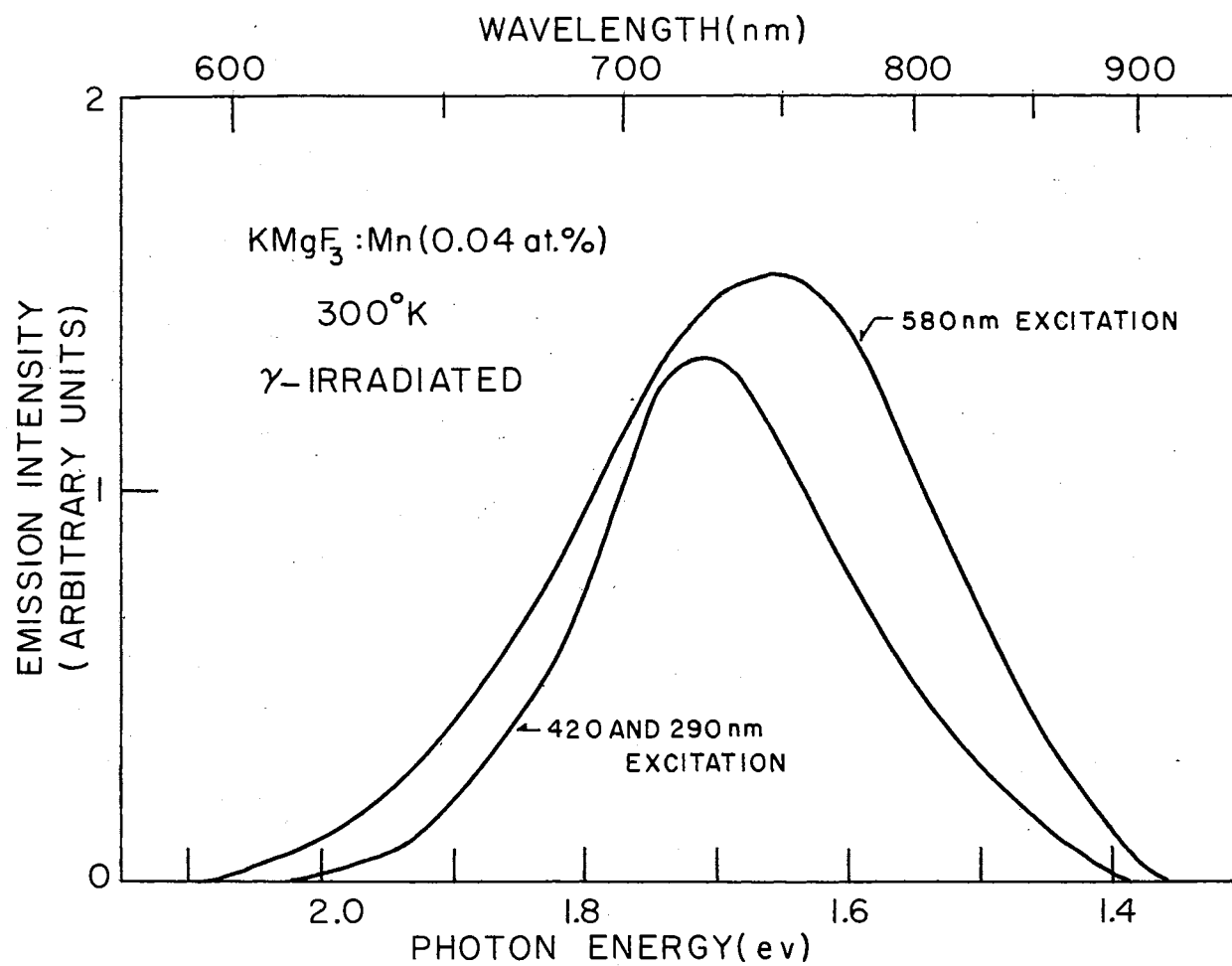


Figure 40. 720 and 750 nm Emission Bands at 300°K in an Electron Irradiated $\text{KMgF}_3:\text{Mn}$ (0.04 at. %)

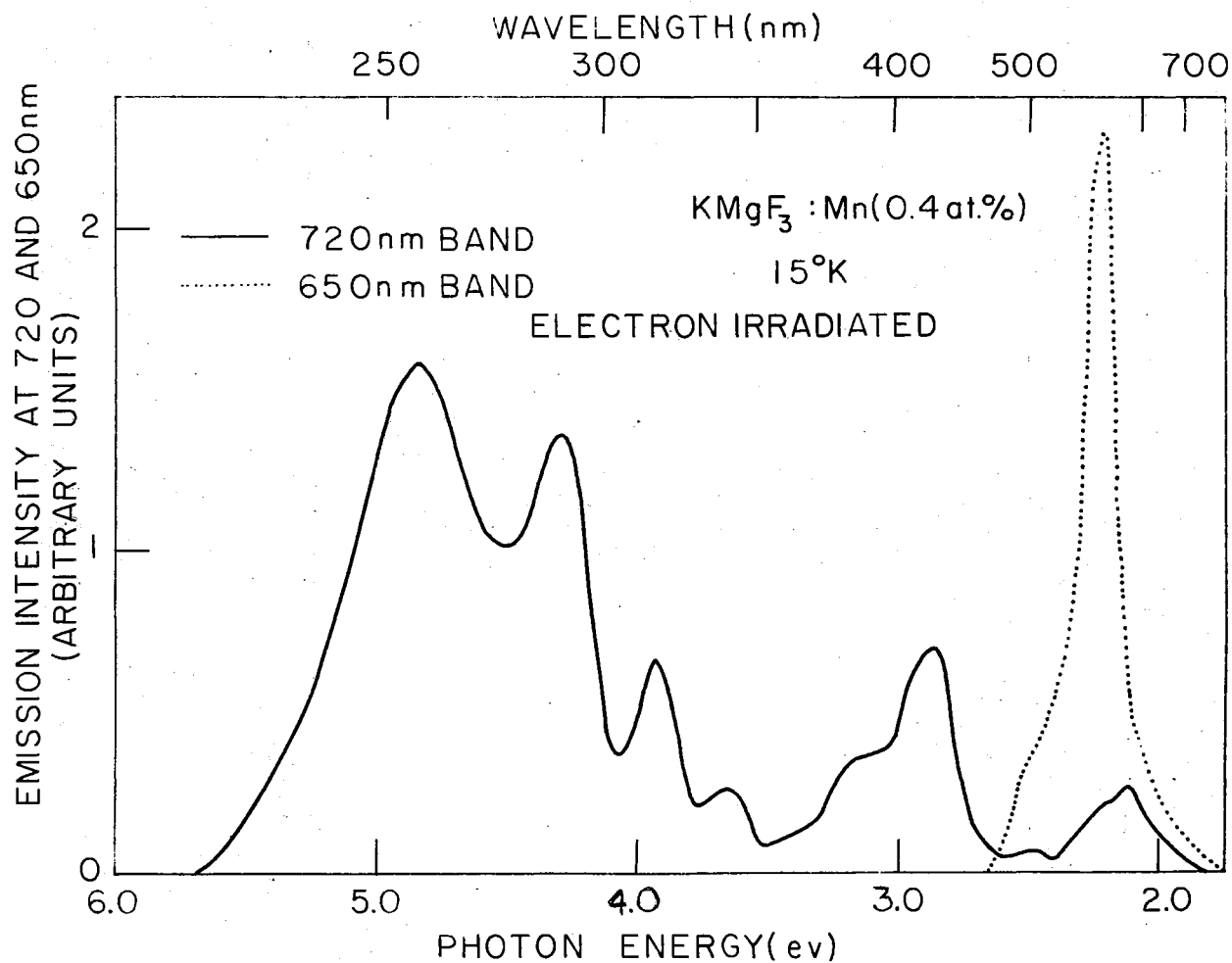


Figure 41. Excitation Spectrum of 720 and 650 nm Emission Band in KMgF₃:Mn (0.4 at. %) Following an Electron Irradiation at 300°K

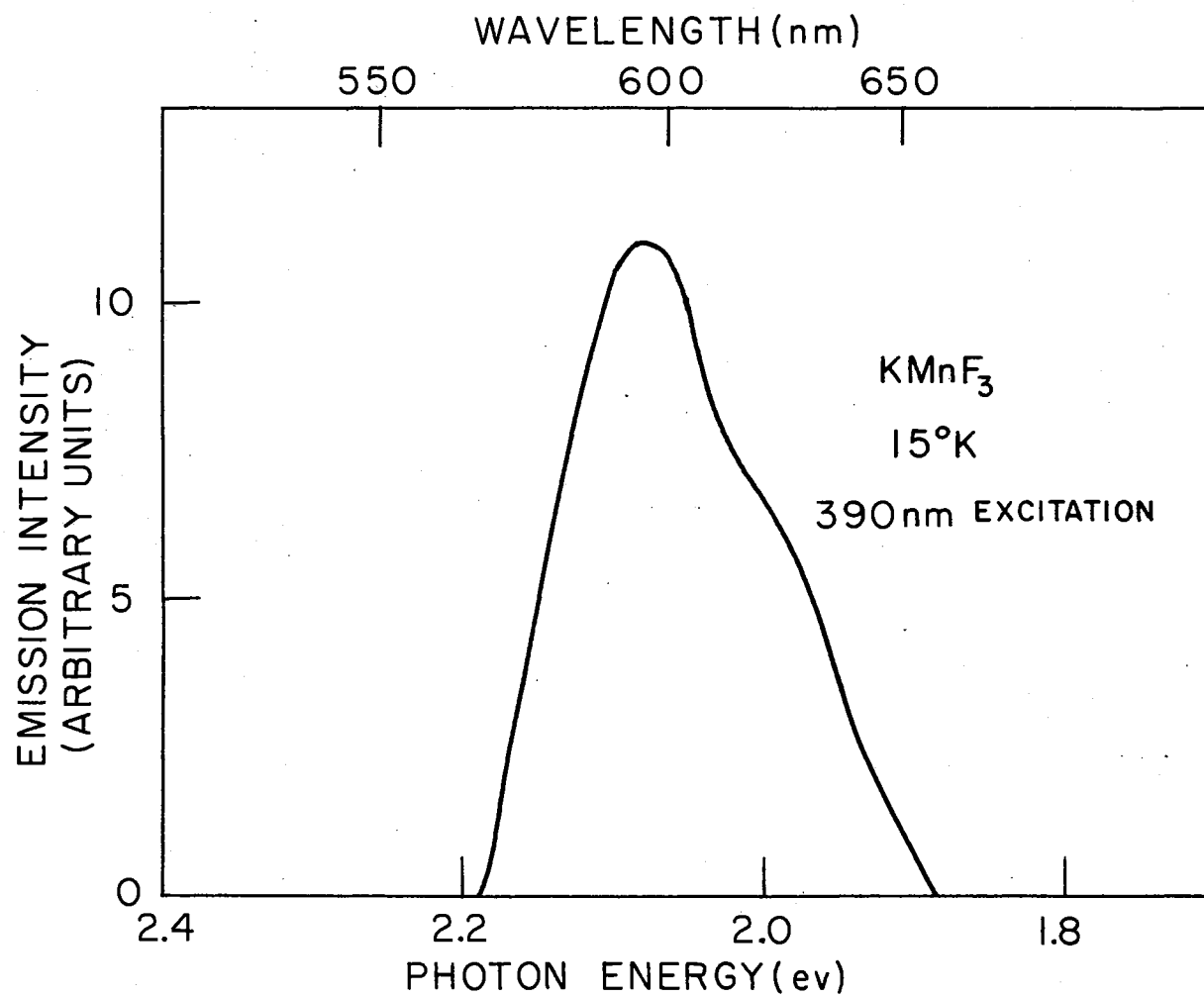


Figure 42. Emission Spectrum in KMnF_3 at 15°K

CHAPTER V

DISCUSSION

Riley et al.⁽⁸⁸⁾ pointed out that the phonon modes interacting most strongly with the excited state of F_2 and F_3 centers have an average frequency of $3.7 \times 10^{13} \text{ sec}^{-1}$ (197 cm^{-1}). Riley and Sibley⁽³¹⁾ reported that the phonon modes interacting most strongly with the ground state of F and F_2 centers also have an average frequency of $3.7 \times 10^{13} \text{ sec}^{-1}$ (197 cm^{-1}). Our results in this investigation indicate that an average frequency of $4.18 \times 10^{13} \text{ sec}^{-1}$ (223 cm^{-1}) is active in interacting with the excited and the ground states of the centers responsible for 570 nm absorption and 750 nm emission bands. Within the simple theory where $\omega_e = \omega_g$, one can predict the Stokes shift for luminescence bands due to F_2 , F_3 , and the center responsible for 570 nm absorption band since one can determine the Huang-Rhys factor from Equation (84). The Huang-Rhys factors are 13.7 for the F_3 emission, 17.9 for the F_2 emission, and 10.5 for the emission from the center responsible for 570 nm absorption band. The high S number for these defects indicates that zero-phonon lines will not be observable⁽⁹⁾ for these bands. This precludes the construction of relatively accurate configuration coordinate diagrams since zero-phonon lines are necessary for an unambiguous interpretation. However, such diagrams can still be constructed from the information given above and Equations (84a) and (84b). Figure 43 shows the configuration coordinate diagram for the center responsible for 570 nm absorp-

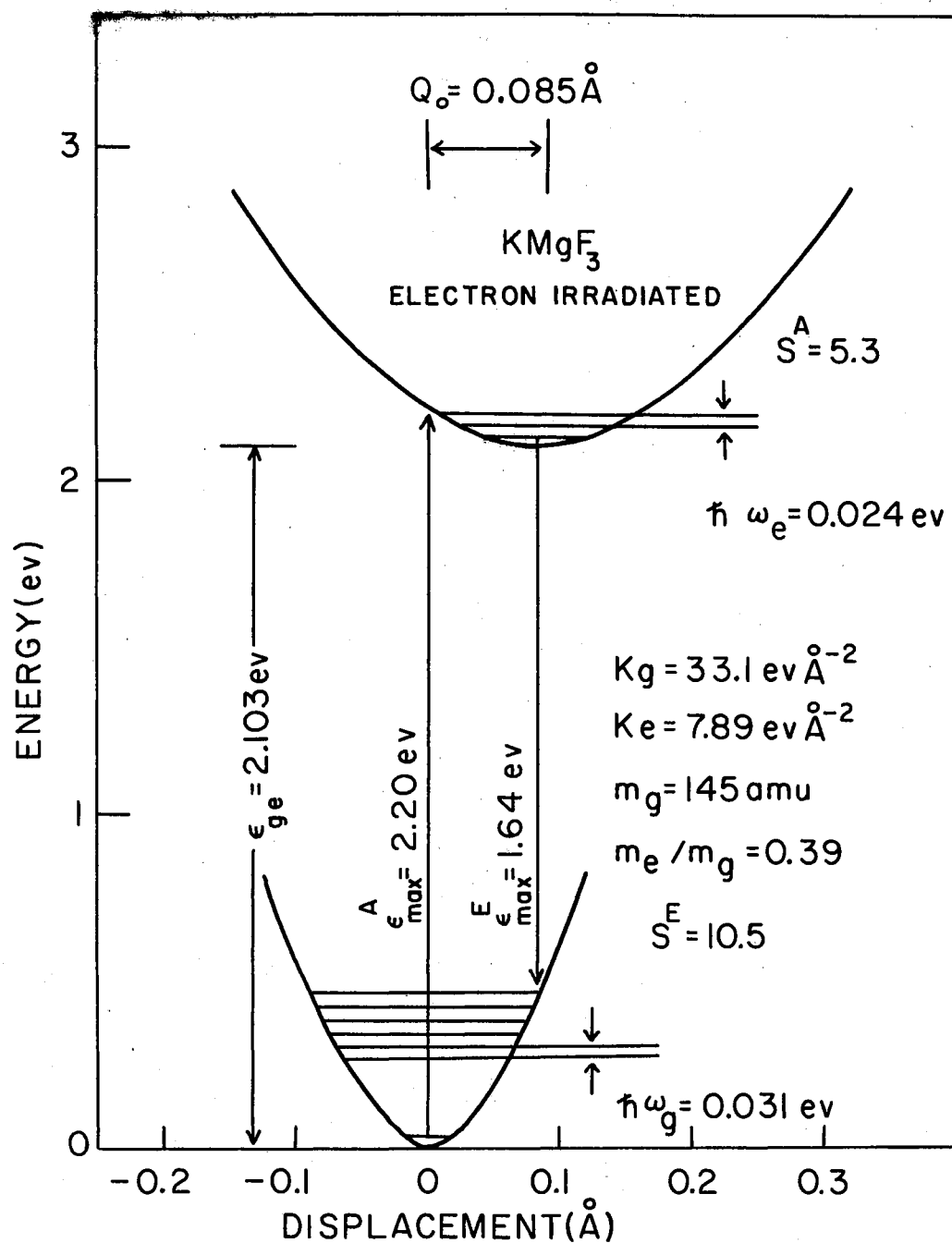


Figure 43. Configuration Coordinate Diagram for the Center Responsible for 570 nm Absorption Band and 750 nm Emission Band in KMgF_3

tion band in KMgF_3 .

As mentioned earlier only light having a wavelength in the region corresponding to the π electric dipole transition of the F_2 center is efficient at reorienting centers. The distribution of defects shown in Table IV for the different polarizations of bleaching light suggests that F_2 centers reorient by 60° jump rather than 90° jump. There is good agreement between the absorption coefficient ratios predicted from the polarized luminescence measurements and those values actually observed, as given in Table V. This indicates that the 590 emission is due to F_2 centers and that it is primarily a σ - σ transition. Turner, et al.⁽⁹¹⁾, Dreyfus⁽⁹²⁾ and Schneider⁽⁹³⁾ have investigated the orientation of F_A centers and F_2 centers, respectively. Schneider found that F_2 centers reorient indirectly by absorbing light, forming F_2^+ centers which then absorb light and rotate. When the reoriented F_2^+ centers capture electrons, then reoriented F_2 centers are produced. F_2^+ centers have not yet been observed in KMgF_3 ; however, our data are not inconsistent with his interpretation.

From a comparison with the absorption spectra data for LiF ^(9,94-96) which has lattice constant of 4.017 \AA ,⁽⁹⁷⁾ it is tempting to attribute the 477 nm zero-phonon line to F_3^+ centers, but before such an assignment can be made polarized bleaching or stress splitting experiments must be done.

From the preceding chapter we know that 395 nm (F_3 center absorption peak) excitation is followed by 465 nm emission, 445 nm (F_2 center absorption peak) excitation is followed by 590 nm emission, and 570 nm excitation is followed by 750 nm emission. Since the 465 and 590 nm emission can be absorbed by the defects responsible for the 445 nm and

570 nm absorption bands there is a strong possibility for cascade type energy transfer⁽⁶⁵⁾ in an irradiated KMgF_3 crystal. Figure 26 shows the 465, 590, and 750 nm emissions excited by light of wavelengths 395, 445, and 570 nm. The top panel in Figure 26 shows that 590 nm emission can be excited either by 445 or 395 nm light, while 750 nm emission can be excited by 570 nm as well as 445 and 395 nm light. Figures 15, 18, and 21 show the excitation spectra for the 465, 590, and 750 nm emission bands. These figures also suggest that there is most likely cascade type energy transfer among the color centers in KMgF_3 . Energy absorbed by F_3 centers may be transferred to F_2 centers and the center responsible for 570 nm absorption band, while energy absorbed by F_2 centers may be transferred to the center responsible to 570 nm absorption band. To clarify the energy transfer mechanism, the lifetime measurements have to be done.

The optical transitions from substitutional Mn^{2+} impurities in KMgF_3 are strongly forbidden by both spin and parity selection rules. The crystal field states have even parity because of the inversion symmetry of the Mn^{2+} ion sites and the spin has to be changed by $\Delta S = \pm 1$ in a single ion excitation since the Mn^{2+} ion has a sextet ground state and quartet excited states. When 3d ion impurity pairs are present some of the forbiddenness is lifted because of the exchange interactions so that the oscillator strengths of the transitions are several orders of magnitude greater^(35,41,42,45,46,58,59). There are three possible ways of lifting the selection rules: (1) The odd parity lattice mode perturbs the symmetry of Mn^{2+} ion site. In this case a temperature dependent oscillator strength is expected⁽⁵¹⁾. (2) The exchange interaction between two Mn^{2+} ions lifts the spin forbiddenness, and (3) both (1) and

(2) occur at the same time and lift both spin and parity forbiddenness. If an F center can be trapped between an impurity pair (Mn-F-Mn) a further increase in the oscillator strength should be observable since the local symmetry changes from O_h to C_{4v} and there should be greater wave function overlap. Table VII illustrates the absorption energies for the various Mn^{2+} transitions in $KMnF_3$, $KMgF_3:Mn$, and an irradiated $KMgF_3:Mn$. The assignments of the transitions which have been made previously are also shown as are the oscillator strengths, f . It should be noted that the oscillator strengths for the transition from the Mn-F center complex (Mn-F-Mn) in an irradiated $KMgF_3:Mn$ are some 10^5 times as great as those in $KMnF_3$. Sell and Stokowski⁽⁶¹⁾ have reported that they observed in MnF_2 a small increase in oscillator strength of the Mn^{2+} transition induced by Ca impurities. The optical transitions in the irradiated crystals are shifted to lower energy due to the presence of the F centers, but it can be seen from the Table VII that in the higher levels, e.g., 4D and 4F , the transitions occur at essentially the same position as they do for the unirradiated specimens. Since the transitions in $KMnF_3$ have previously been assigned^(41,42), our task is to identify, if possible, the energy levels for these defect transitions. Fortunately, since the polarization, σ or π , for several energy levels is known the task is not too complicated. Figure 44 shows the Örgel diagram for $3d^5$ configuration in O_h crystal field^(38,50). As can be seen from Table VII when the local symmetry of a defect is changed from O_h to C_{4v} the $^6A_{1g} \rightarrow ^4T_{1g}$ transition becomes $^6A_1 \rightarrow ^4A_2 + ^4E$.⁽⁹⁸⁾ In the C_{4v} symmetry group the A_1 element is along the major axis of the Mn-F-Mn defect and is equivalent to a σ transition. The E symmetry element is equivalent to a π transition. The data shown in Figure 29 and the discussion in

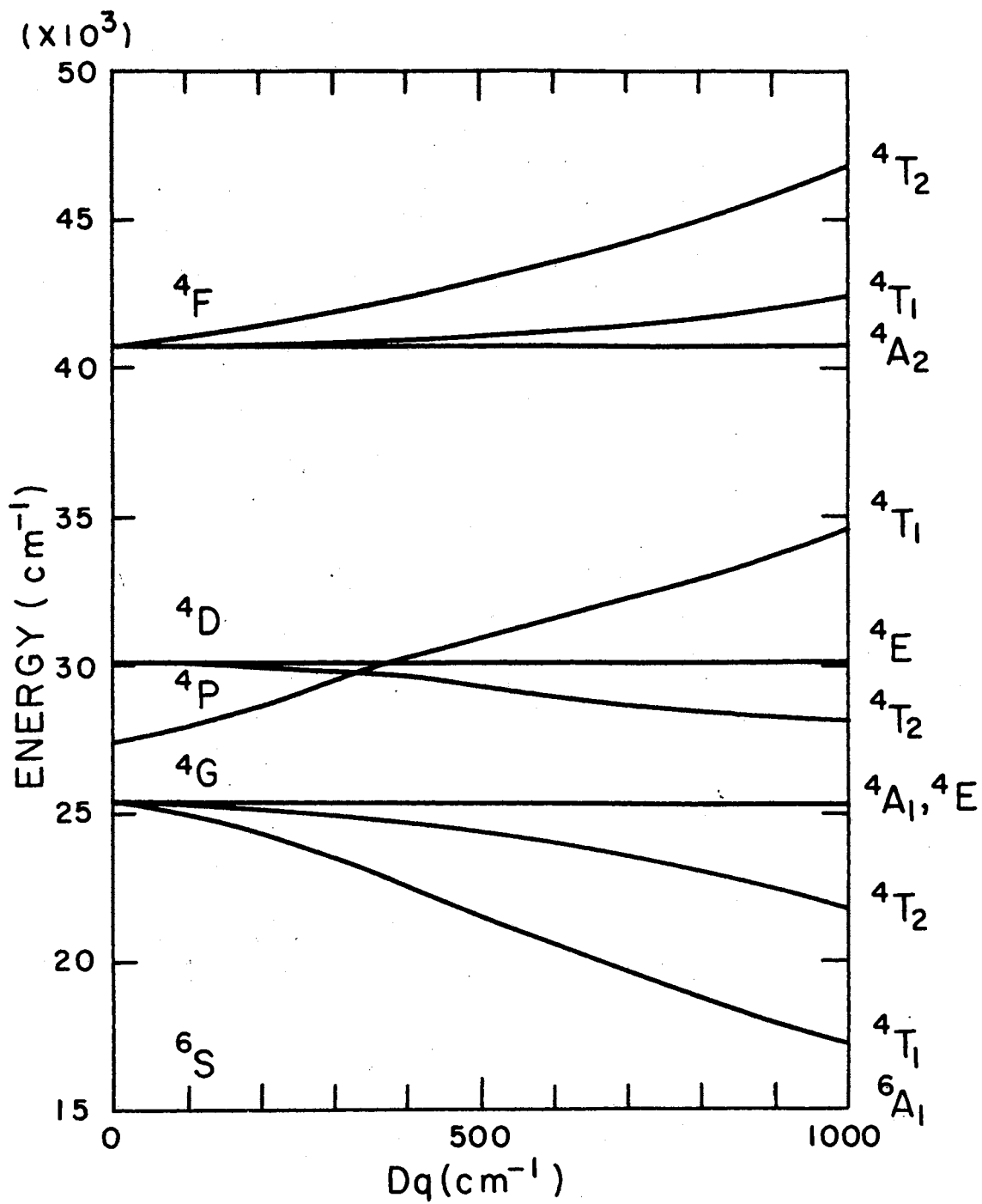


Figure 44. Orgel Diagram for $3d^5$ Configuration

reference 30 enable us to make the symmetry assignments for the transitions shown in Table VII. The F center absorption occurs at about 270 nm and could affect our assignment for the 246 nm transition. The optical bleaching process might form polarized F_A centers which would contribute to the absorption in this region.

It is well known that forbidden electronic transitions can become allowed through vibronic transitions^(65,98). This is particularly true for the Mn^{2+} ions in $KMgF_3$ since the transitions are so strongly forbidden. In the perovskite lattice there are three possible T_{1u} and one possible T_{2u} lattice modes^(99,100). The vibrational frequencies of the three T_{1u} and one T_{2u} modes have been given as⁽¹⁰⁰⁾; $\nu_1 = 478 \text{ cm}^{-1}$ (MgF stretch), $\nu_2 = 300 \text{ cm}^{-1}$ (FMgF bend), $\nu_3 = 156 \text{ cm}^{-1}$ (K-MgF₂ stretch) and $\nu_4 = 330 \text{ cm}^{-1}$. When the symmetry is changed from O_h to C_{4v} due to the presence of the F center then the T_{1u} modes are transformed to $A_1 + E$. This suggests that vibronic transitions should occur in this system. Figure 31 indicates that some of the observed transitions are indeed temperature dependent and may be classified as vibronic. The energy differences between the main peak and those of the vibronic peaks are such as to indicate that the most strongly interacting mode is ν_1 vibrational mode with the first harmonic hidden under the main peak. This assignment is reasonable since it is the MgF stretch mode and would interact most strongly with the Mn-F-Mn defect. The value of ν_3 is close to the $3.7 \times 10^{13} \text{ sec}^{-1}$ (197 cm^{-1}) vibrational frequency from the color center data^(27,31,88). These data also support the assignments made above. From the above assignments we can describe the vibrational side bands as follows:

$$\begin{aligned}
 435 \text{ nm} &= 24.39 \times 10^3 \text{ cm}^{-1} - 3 h \nu_1, \\
 426 \text{ nm} &= 24.39 \times 10^3 \text{ cm}^{-1} - 2 h \nu_1, \\
 410 \text{ nm} &= 24.39 \times 10^3 \text{ cm}^{-1}, \\
 \text{and} \quad 394 \text{ nm} &= 24.39 \times 10^3 \text{ cm}^{-1} + 2 h \nu_1.
 \end{aligned}$$

The side band at 595 nm also shows strong temperature dependence as in Figure 34 and may be described as

$$\begin{aligned}
 565 \text{ nm} &= 17.69 \times 10^3 \text{ cm}^{-1}, \\
 \text{and} \quad 597 \text{ nm} &= 17.69 \times 10^3 \text{ cm}^{-1} - 2 h \nu_1.
 \end{aligned}$$

The lines at 416 and 422 nm which are illustrated in Figure 31 increase with decreasing temperature are most likely zero-phonon or phonon assisted transitions. However, we have not yet attempted to identify the centers responsible for these lines by stress splitting or other techniques.

The luminescence spectrum portrayed in Figure 37 and the excitation spectra shown in Figures 27 and 38 are especially interesting. First, we consider the room temperature emission band that occurs at 630 nm. Klasens et al.⁽⁴⁰⁾ have shown that Mn^{2+} emission in perovskite and rutile materials depends on the divalent cation to fluorine distance in the material. For example, they point out that one should expect Mn^{2+} in KMgF_3 to emit at around 600 nm whereas Mn^{2+} in CsCaF_3 should emit at around 548 nm. The smaller the cation to fluorine distance the larger the emission wavelength. This behavior explains the observation, pictured in the inset of Figure 37, that the emission wavelength increases with decreasing temperature for the 630 nm band.

The low temperature 677 nm emission is shifted to longer wavelength

with respect to the high temperature 630 nm emission and has a much longer lifetime. The later observation suggests that the high temperature transition is an allowed one, whereas the low temperature emission is partially forbidden. The temperature dependence of the luminescence shown in Figure 37 indicates that there is sufficient thermal energy available at high temperature to populate the higher energy allowed transition level and at low temperature the electrons populate primarily forbidden transition levels. The temperature dependence of the luminescence lifetime at 677 nm is shown in Figure 45. The luminescence lifetime of ${}^4A_2 \rightarrow {}^6A_1$ transition (667 nm emission) at 4.2°K is 4.8×10^{-4} sec and that of ${}^4E \rightarrow {}^6A_1$ transition (630 nm emission) at 300°K is 16×10^{-6} sec. From these data we can analyze for the electron populations in the following manner: Let $I({}^4A_2)$ and $I({}^4E)$ represent the integrated intensities of the ${}^4A_2 \rightarrow {}^6A_1$ and ${}^4E \rightarrow {}^6A_1$ transitions, respectively.

$$\frac{I({}^4E; 300^\circ\text{K})}{I({}^4A_2; 4.2^\circ\text{K})} = \frac{n({}^4E; 300^\circ\text{K})/\tau({}^4E; 300^\circ\text{K})}{n({}^4A_2; 4.2^\circ\text{K})/\tau({}^4A_2; 4.2^\circ\text{K})} \quad (87)$$

where n refers to the population of the indicated level and τ is the measured radiative lifetime. The luminescence spectra are obtained by exciting the sample with 590 nm light which has a bandwidth of 10 nm.

The areas under the absorption spectra at 4.2°K and 300°K were the same in this wavelength region. From these data one can assume $n({}^4E; 4.2^\circ\text{K}) \approx 0$ and $n({}^4A_2; 4.2^\circ\text{K}) \approx n({}^4A_2; 300^\circ\text{K}) + n({}^4E; 300^\circ\text{K})$. From the equilibrium populations of a system with two levels,

$$\frac{n({}^4E; 300^\circ\text{K})}{n({}^4A_2; 300^\circ\text{K})} = 2 e^{-\Delta/300k} \quad (88)$$

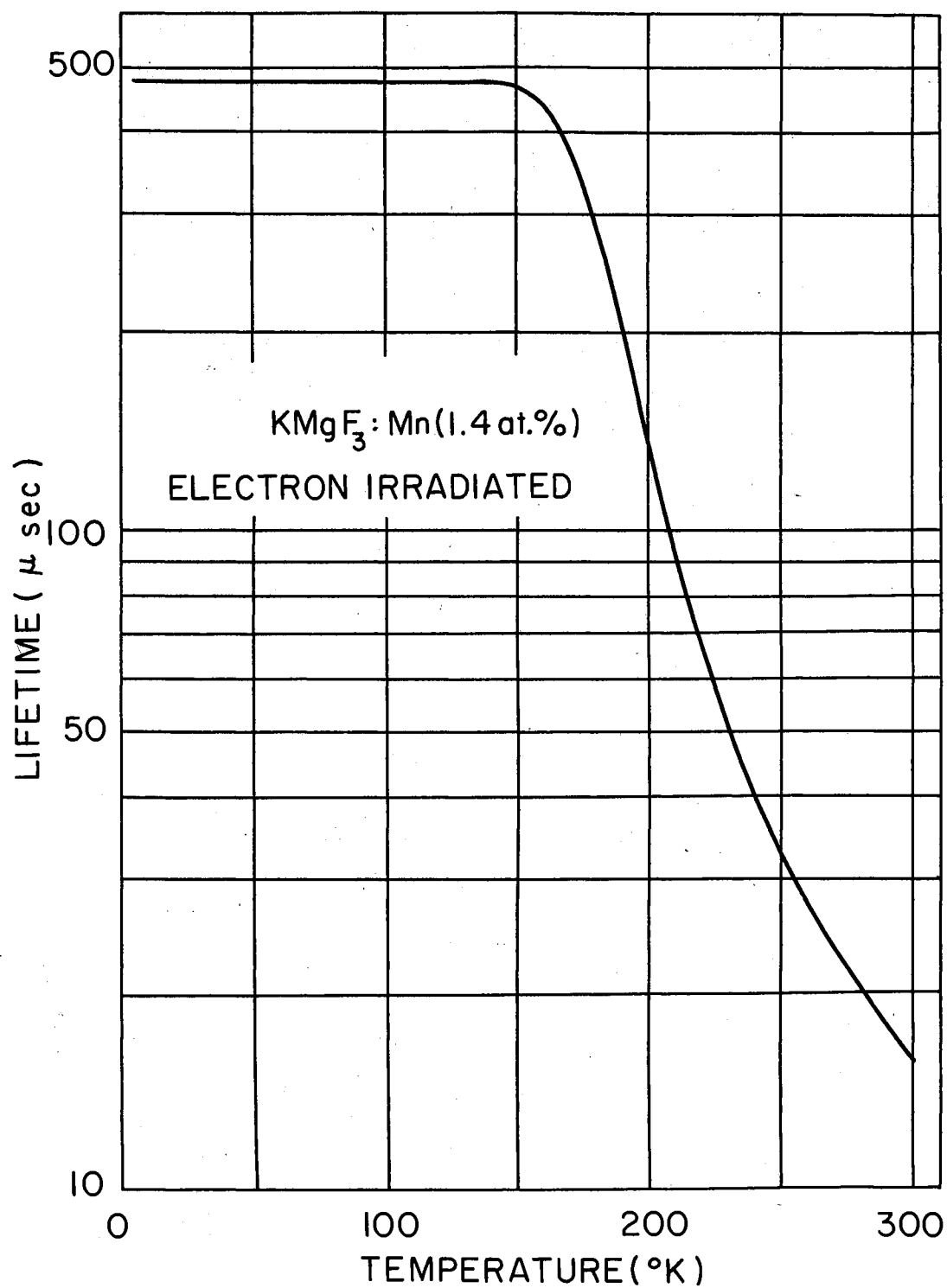


Figure 45. Temperature Dependence of the Emission Lifetime for 677 nm Emission in $\text{KMgF}_3:\text{Mn}$ (1.4 at. %)

Experimentally,

$$\frac{\tau(^4A_2; 4.2^\circ K)}{\tau(^4E; 300^\circ K)} \approx 30 \quad \text{and} \quad \frac{I(^4E; 300^\circ K)}{I(^4A_2; 4.2^\circ K)} \approx 5. \quad (89)$$

Then

$$\frac{n(^4E; 300^\circ K)}{n(^4A_2; 4.2^\circ K)} \approx \frac{n(^4A_2; 300^\circ K) 2e^{-\Delta/300k}}{n(^4A_2; 300^\circ K) + n(^4E; 300^\circ K)} = \frac{2}{2+e^{\Delta/300k}} = 0.167, \quad (90)$$

where Δ is the energy separation between 4E and 4A_2 levels, and k is boltzmann's constant. The approximate value of Δ obtained from Equation (87) by using above values is 480 cm^{-1} . From the luminescence energy difference of 1000 cm^{-1} (630 to 677 nm) it is expected that $^4A_2 \rightarrow ^6A_1$ transition is 520 cm^{-1} higher in ground state vibrational energy before relaxation than the $^4E \rightarrow ^6A_1$ transition. Figure 46 shows the configuration coordinate for the luminescence system of Mn^{2+} in KMgF_3 .

Since the energy difference Δ is 480 cm^{-1} , we might expect the change of luminescence band from 630 to 677 nm to occur at about the same temperature the phonon side bands disappear. This is the case, as can be seen by comparing Figures 31 and 37. The excitation spectra illustrated in Figures 27 and 38 indicate that both the 677 nm and 630 nm bands arise from the Mn-F-Mn defect and that electrons in all of the higher energy levels decay to the lowest level before emission occurs.

The sharp line structure observed on both the emission and the absorption bands at 7°K must arise from electron-phonon interactions or spin-orbit interactions. Similar sharp line structure has been observed in RbMnF_3 , MnF_2 , and KMnF_3 (101-104). The number of lines seems to be

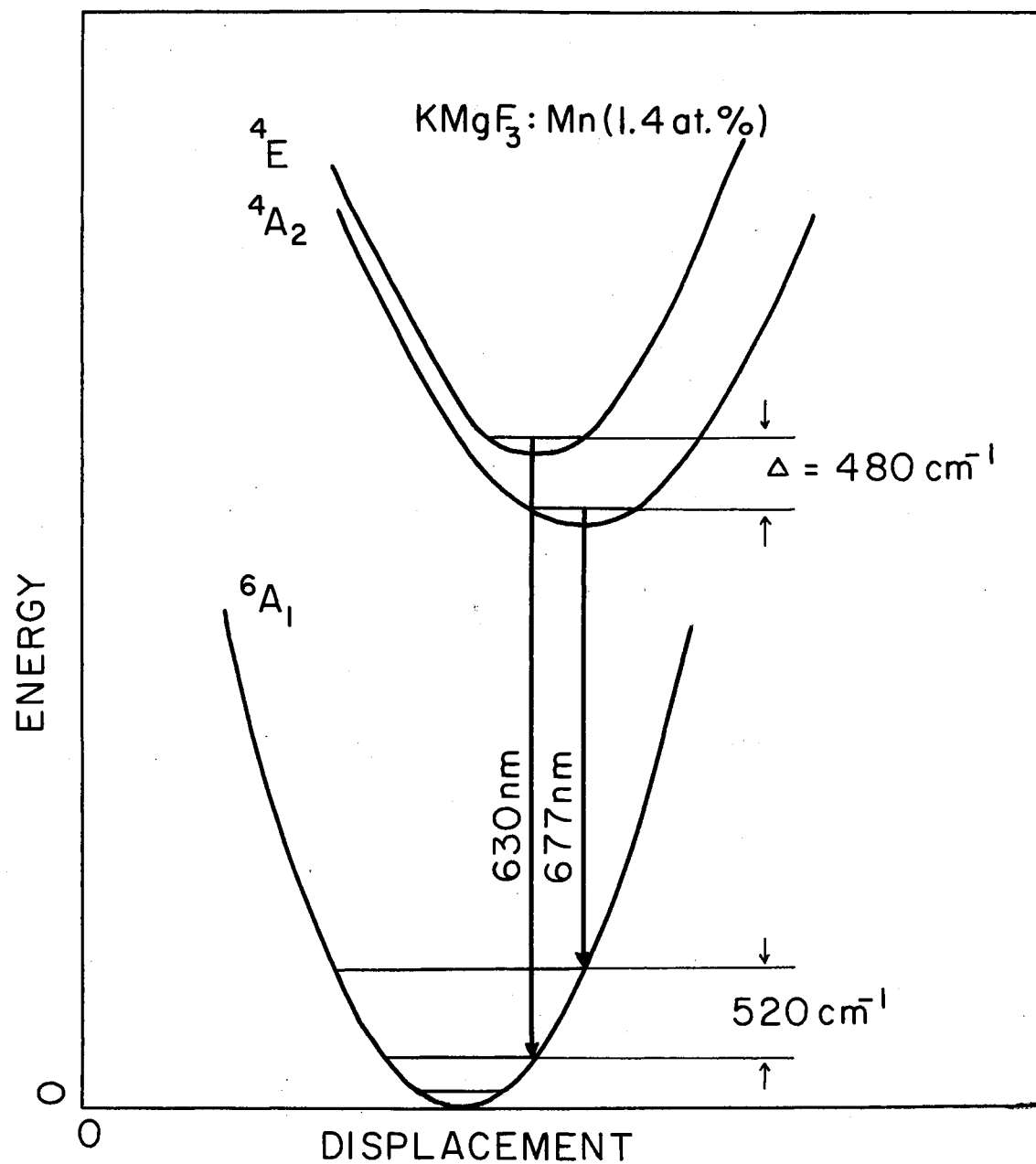


Figure 46. Configuration Coordinate Diagram for the Luminescence System of Mn^{2+} in an Electron Irradiated $\text{KMgF}_3:\text{Mn}$

dependent on impurity and temperature⁽¹⁰¹⁾. The energy differences between the transition peaks are shown in Table VI. The 410 nm band is due to a σ transition and the 565 nm absorption band is due to a π transition. The separation of the peaks is much greater in the case of the σ transition than for the π transition as might be expected if exchange interactions are the cause of the splitting. However, it is not at all clear whether the observed splittings are due to exchange, spin-orbit coupling, or even magnon interactions, although latter is extremely doubtful.

KMgF₃:Mn crystals which were electron irradiated at 300°K show F, F₂, F₃, and 570 nm absorption bands regardless of the concentrations of Mn²⁺ ions. But sample, KMgF₃:Mn (0.4 at. %) and KMgF₃:Mn (1.4 at. %) show some additional absorption bands at 570, 350, etc. There were no absorption bands corresponding to Mn-F-Mn defects in these samples. The emission from room temperature irradiated KMgF₃:Mn shows not only F₂, F₃, and 750 nm emission bands but also 650, 720, and 360 nm emission bands. The 720, 360, and 650 nm emission bands have fine structures at low temperature and the 720 nm band is equivalent to the 720 nm emission band observed in low temperature irradiated KMgF₃:Mn. There were no 677 and 630 nm emission bands in room temperature irradiated KMgF₃:Mn. The origin of the additional absorption bands and 720, 360 and 650 nm emission bands is not clear at this time, but it is clear that these bands are not related to Mn-F-Mn defects and are possibly related to more complicated clusters of F centers, Mn²⁺ ions, and interstitials. By comparing with the emission from the low temperature irradiated KMgF₃:Mn it is much more clear that at least 720 and 650 nm emission is due to more complicated F center-Mn complex. In summary we may say that during

room temperature irradiation the probabilities of producing more complicated clusters and F-aggregate centers are larger than that of Mn-F-Mn defects. But more work has to be done before we can make any definite identification between these defect clusters and the observed absorption and emission bands. Gooen et al.⁽¹⁰¹⁾ related two emission bands in RbMnF_3 to different fluorescence transitions corresponding to different trapping sites using an idea involving free-exciton absorption and trapped excitation emission. The same idea was used to explain luminescence in MnF_2 by Green et al.⁽¹⁰²⁾ Our data are not inconsistent with this interpretation.

The lifetime of Mn^{2+} luminescence at 20°K from KMnF_3 was reported as 30 msec whereas Mn^{2+} luminescence at 7°K from an irradiated $\text{KMgF}_3:\text{Mn}$ has a lifetime of 4.8×10^{-4} sec. The lifetime difference between these two systems can be explained by the Mn^{2+} transition probabilities in two systems. Mn^{2+} transitions in KMnF_3 are partially forbidden and have a relatively long lifetime, while Mn^{2+} transitions in an irradiated $\text{KMgF}_3:\text{Mn}$ satisfy the parity selection rule and have a relatively short lifetime. In addition, in an irradiated $\text{KMgF}_3:\text{Mn}$, there are exchange interactions of three paramagnetic ions, the Mn^{2+} pair and an F center. This is the other factor shortening the lifetime of Mn^{2+} transitions in $\text{KMgF}_3:\text{Mn}$.

It appears that it is possible with low doses of γ -rays or electrons to increase the magnitude of the absorption bands for the 3d transition metal ions sufficiently that they can be studied in detail. However, Ikeya^(105,106) has irradiated $\text{NaCl}:\text{Mn}$ and found that the radiation changes the valence state of Mn^{2+} to Mn^{1+} and M^0 . Jain and Lal⁽¹⁰⁷⁾ found similar effects for $\text{NaCl}:\text{Co}$.

CHAPTER VI

SUMMARY AND PROBLEMS FOR FURTHER STUDY

It has been shown that F_2 centers have absorption bands at 282 and 445 nm and an emission at 590 nm. F_3 centers absorb light of 250 and 395 nm and emit light of 465 nm. Both of these centers can be reoriented by optical polarized bleaching and F_2 centers reorient by 60° jump, but the exact mechanism for the reorientation is not yet known.

The absorption bands due to an F center trapped at a fluorine site between adjacent substitutional Mn-ion impurities (Mn-F-Mn) have been assigned to various energy levels by means of polarized bleaching experiments and crystal field theory. The spin forbiddenness of the transition is partially lifted by the exchange interactions of the three paramagnetic ions, the Mn^{2+} pair and an F center, and the parity forbiddenness is also lifted by the trapped F center between two Mn^{2+} ions. It has been found that spin forbiddenness is more effective in the transition probabilities of Mn^{2+} than parity forbiddenness. Four vibronic absorption bands at 435, 426, 394, and 597 nm have been described as due to one of the T_{1u} vibrational frequencies, 478 cm^{-1} , of $KMgF_3$ lattice.

The luminescence from these Mn-F-Mn defects in low temperature irradiated $KMgF_3:Mn$ has been studied and is found to consist of two bands. One of these, the 677 nm band, is a partially forbidden transition with a long lifetime, 4.8×10^{-4} sec. at low temperature, whereas the 630 nm band seen at room temperature is an allowed transition with relatively

short lifetime of 16×10^{-6} sec. Sharp line structures were apparent at low temperature both in absorption and emission bands, but no definitive statement can be made about this fine structure.

The problems to be considered for further study include:

(1) The identification of the narrow 477 nm absorption line observed at LHeT in irradiated KMgF_3 . Since LiF has an F_3^+ center zero-phonon line at 478.4 nm this narrow line observed in KMgF_3 may be due to the zero-phonon line of F_3^+ center in KMgF_3 . Since uniaxial stress has proved to be a very powerful technique, and examination of the splitting patterns of zero-phonon lines for stresses applied in crystal symmetry directions has provided in most cases an unambiguous symmetry determination^(67,96,108), a stress splitting along with the polarized emission from this center seems to be a means of determining the symmetry of this center.

(2) The identification of the origin of narrow 220 nm and the broad 340 nm absorption bands at LNT in an irradiated KMgF_3 after low temperature UV bleaching should be made. From the annealing data and the shapes of the bands the 340 nm band may be due to F^- centers whereas the 220 nm band may come from $\text{F}^+(\alpha)$ centers. But more work must be done before any definite assignment of these bands can be made.

(3) The identification of the 720 and 650 nm luminescence bands in an irradiated $\text{KMgF}_3\text{:Mn}$ crystal is important. These bands may possibly be related to more complicated clusters of F centers, Mn^{2+} ions, and interstitials. If so, this study would be closely connected to understanding of the radiation damage processes in pure and Mn-doped KMgF_3 . Additive coloration of KMgF_3 and $\text{KMgF}_3\text{:Mn}$ will help to understand this radiation damage process and also will be one of the best ways of con-

firming our model, Mn- \bar{F} -Mn defect.

(4) F_A type centers in an irradiated $KMgF_3:Mn$ should be studied. The 250 nm band that is observed after UV bleaching may be due to F_A type centers but so far it has not been possible to identify this band by polarized bleaching techniques. A study of systems such as $KMgF_3:Na;Li$, etc., is also important because it will help us to understand the effect of doping with larger cations on the F_A type centers in these systems.

(5) Studies of the enhancement of 3d impurity ion absorption by color centers in systems such as $KMgF_3:Fe;Ni;Co;V;Cr$ and $MgF_2:Mn;Fe;Ni;Co;V;Cr$, etc., will give a better idea of optical transitions of 3d ions as perturbed by trapped F centers. In the rutile structure it is possible to distinguish between the electric dipole and magnetic dipole transitions and the effects of F centers on electric dipole and magnetic dipole transitions can be studied separately. Furthermore, since some of these transition metal ions have allowed transitions it is possible to investigate the effects of F centers on the spin allowed and the spin forbidden transitions separately.

(6) Identification of 369.4 nm zero-phonon line observed in an irradiated $KMgF_3$ should be made by means of stress splitting techniques.

(7) An experimental determination of excited state splittings will yield information on the Jahn-Teller interactions in the excited states of the Mn- \bar{F} -Mn system.

(8) A theoretical treatment of the Mn- \bar{F} -Mn system must be attempted.

BIBLIOGRAPHY

- (1) Van Doorn, C. Z., Philips. Res. Rept. Suppl. 4, 1 (1962).
- (2) Maurer, R. J., J. Chem. Phys. 50, 1974 (1969).
- (3) Van Doorn, C. Z., Rev. Sci. Inst. 32, 755 (1961).
- (4) Pohl, R. W., Proc. Phys. Soc. (London) Suppl. 49, 3 (1937).
- (5) Seitz, F., Rev. Mod. Phys. 26, 7 (1954).
- (6) Seitz, F., Rev. Mod. Phys. 18, 384 (1946).
- (7) Schulman, J. H. and W. D. Compton, Color Centers in Solids (Pergamon, New York, 1971).
- (8) Compton, W. D. and Rabin, Solid State Physics 16, 121 (1964) edited by F. Seitz and D. Turnbull (Academic Press, New York).
- (9) Fowler, W. B., Physics of Color Centers (Academic Press, New York, 1968).
- (10) Crawford, J. H. and L. M. Slifkin, Point Defects in Solids (Plenum, New York, 1972).
- (11) Markham, J. J., Solid State Physics, Suppl. 8 (Academic Press, New York, 1966).
- (12) Vehse, W. E., W. A. Sibley, F. J. Keller and Y. Chen, Phys. Rev. 167, 828 (1968).
- (13) Ward, W. C. and E. B. Henseley, Phys. Rev. 175, 1230 (1968).
- (14) Vehse, W. E., O. E. Facey and W. A. Sibley, Phys. Stat. Sol. (a) 1, 679 (1970).
- (15) Hersh, H. N. and Bronstein, Am. J. Phys. 25, 306 (1957).
- (16) Uchida, Y. and Y. Nakai, J. Phys. Soc. Japan 8, 795 (1953).
- (17) Paramo, N., J. Phys. Soc. Japan 30, 1106 (1971).
- (18) Sonder, E. and W. A. Sibley, In Point Defects in Solids, edited by J. H. Crawford and L. M. Slifkin (Plenum, New York, 1972).
- (19) Crawford, J. H., Adv. in Physics 17, 93 (1968).

- (20) Knox, R. S., Phys. Rev. Letters 2, 87 (1959).
- (21) de Boer, J. H., Recueil Trav. Chim. Pays-Bas 56, 301 (1937).
- (22) Johnson, L. F., H. J. Guggenheim and R. A. Thomas, Phys. Rev. 149, 179 (1966).
- (23) Johnson, L. F., R. E. Dietz and H. J. Guggenheim, Phys. Rev. Letters 17, 13 (1966).
- (24) Bishop, H. E., R. P. Henderson, P. Iredal and D. Pooley, Appl. Phys. Letters 20, 504 (1972).
- (25) Schneider, I., Appl. Optics 10, 980 (1971) and Appl. Optics 6, 2197 (1967).
- (26) Tubbs, M. R. and D. K. Wright, Phys. Stat. Sol. (a) 7, 155 (1971).
- (27) Riley, C. R., Ph.D. thesis (University of Tennessee, 1970).
- (28) Wyckoff, R. W. G., Crystal Structures, Vol. 2 (Interscience, New York, 1964) p. 392.
- (29) Hall, T. P. P. and A. Leggeat, Solid State Commun. 7, 1657 (1969).
- (30) Vehse, W. E. and W. A. Sibley, Phys. Rev. B 6, 2443 (1972).
- (31) Riley, C. R. and W. A. Sibley, Phys. Rev. B 1, 2789 (1970).
- (32) Hall, T. P. P., Brit. J. Appl. Physics 17, 1011 (1966).
- (33) Lewis, J. T., J. L. Kolopus, E. Sonder and M. M. Abraham (to be published).
- (34) Okamoto, F., Phys. Rev. 124, 1090 (1961).
- (35) Ferguson, J., H. J. Guggenheim and Y. Tanabe, J. Phys. Soc. Japan 21, 692 (1966).
- (36) Mehra, A. and P. Venkateswarlu, J. Chem. Phys. 47, 2334 (1967).
- (37) Srivastava, J. P. and A. Mehra, J. Chem. Phys. 57, 1587 (1972).
- (38) Stout, J. W., J. Chem. Phys. 31, 709 (1959).
- (39) Holloway, W. W., E. W. Prohofsky and M. Kestigan, Phys. Rev. 139, A954 (1965).
- (40) Klasens, H. A., P. Zalm and F. O. Huysman, Philips. Res. Rept. 8, 441 (1953).
- (41) McClure, D. S., Solid State Physics 9, 399 (1959) edited by F. Seitz and D. Turnbull (Academic, New York).

- (42) Hush, N. S. and R. J. M. Hobbs, Progress in Inorganic Chemistry 10, 259 (1968), edited by F. A. Cotton (Interscience, New York).
- (43) Ferguson, J., H. J. Guggenheim, H. Kamimura and Y. Tanabe, J. Chem. Phys. 42, 775 (1965).
- (44) Ferguson, J., D. L. Wood and K. Knox, J. Chem. Phys. 39, 881 (1963).
- (45) Ferguson, J., Progress in Inorganic Chemistry 12, 159 (1970, edited by S. J. Lippard (Interscience, New York).
- (46) Ferguson, J., H. J. Guggenheim and Y. Tanabe, J. Appl. Phys. 36, 1046 (1965).
- (47) Tanabe, Y. and S. Sugano, J. Phys. Soc. Japan 9, 753 (1954).
- (48) Schroeder, K. A., J. Chem. Phys. 37, 1587 (1962).
- (49) Ballhausen, C. J., Introduction to Ligand Field Theory (McGraw-Hill, New York, 1962).
- (50) Sugano, S., Y. Tanabe and H. Kamimura, Multiplets of Transition-Metal Ions in Crystals (Academic, New York, 1970).
- (51) Fujiwara, T., W. Gebhardt, K. Petanides and Y. Tanabe, J. Phys. Soc. Japan 33, 39 (1972).
- (52) Schawlow, A. L., D. L. Wood and A. M. Clogstoni, Phys. Rev. Letters 3, 271 (1959).
- (53) Ferguson, J., H. J. Guggenheim and Y. Tanabe, Phys. Rev. Letters 14, 737 (1965).
- (54) McClure, D. S., J. Chem. Phys. 39, 2850 (1963).
- (55) Kisliuk, P., A. L. Schawlow and M. D. Sturge, Quantum Electronics, 3, 725 (1964), edited by P. Grivet and B. Bloembergen (Columbia University Press, New York).
- (56) Kisliuk, P. and W. F. Krupke, J. Appl. Phys. 36, 1025 (1965).
- (57) Blazey, K. W. and G. Burns, Phys. Letters 15, 117 (1965).
- (58) Ferguson, J., H. J. Guggenheim and E. R. Krausz, J. Phys. C, 4, 1866 (1971).
- (59) Ferguson, J., H. J. Guggenheim and Y. Tanabe, J. Chem. Phys. 45, 1134 (1966).
- (60) Codling, A. J. B., J. Phys. C 4, 1409 (1971).
- (61) Sell, D. D. and S. E. Stokowski, Phys. Rev. B 3, 2844 (1971).

- (62) Okada, M., M. N. Nakagawa, K. Atobe and T. Shibata, J. Phys. Soc. Japan 30, 1096 (1971).
- (63) Agrawal, M. D. and K. V. Rao, Phys. Stat. Sol. (a) 6, 693 (1971).
- (64) Shore, B. W. and D. H. Menzel, Principles of Atomic Spectra (Wiley, New York, 1967).
- (65) Di Bartolo, B., Optical Interactions in Solids (Wiley, New York 1968).
- (66) Fowler, W. B., In Physics of Color Centers, edited by W. B. Fowler (Academic, New York, 1968).
- (67) Fitchen, D. B., In Physics of Color Centers, edited by W. B. Fowler (Academic, New York, 1968).
- (68) Schiff, L. I., Quantum Mechanics (McGraw-Hill, New York, 1955), p. 246 and 373.
- (69) Stepanov, B. I. and V. P. Gribkovskii, Theory of Luminescence (ILIFEE, London, 1968).
- (70) Dexter, D. L., Solid State Physics 6, 355 (1958).
- (71) Condon, E. U. and G. H. Shortley, The Theory of Atomic Spectra (Cambridge Press, London, 1935).
- (72) Pines, D., Elementary Excitations in Solids (Benjamin, New York, 1963).
- (73) Fermi, E., Nuclear Physics (University of Chicago Press, 1950), p. 142.
- (74) Stepanov, B. I., and V. P. Gribkovskii, Theory of Luminescence (ILIFEE, London, 1968), p. 240.
- (75) Smakula, A., Z. für Physik 59, 603 (1930).
- (76) Smith, D. Y. and D. L. Dexter, Progress in Optics, Vol. X (to be published).
- (77) Feofilov, P. P., The Physical Basis of Polarized Emission (Consultant, New York, 1961).
- (78) Mostoller, M., B. N. Ganguly and R. F. Wood, Phys. Rev. B 4, 2015 (1971).
- (79) Jacobs, P. W. M. and A. K. Menon, J. Chem. Phys. 55, 5357 (1971).
- (80) Klick, C. C., D. A. Patterson and R. S. Knox, Phys. Rev. 133, A1717 (1964).
- (81) Keil, T. H., Phys. Rev. 140, A601 (1965).

- (82) Huang, K. and A. Rhys, Proc. Roy. Soc. (London) A204, 406 (1950).
- (83) Tuttle, E. R., Am. J. Phys. 35, 26 (1967).
- (84) Brice, J. C., The Growth of Crystals From the Melt (Wiley, New York, 1965).
- (85) Vehse, W. E., F. Sherril and C. R. Riley, J. Appl. Phys. 43, 1320 (1972).
- (86) Farge, Y., M. Lambert and R. Smoluchowski, Phys. Rev. 159, 700 (1967).
- (87) Schneider, I., Solid State Commun. 9, 2191 (1971).
- (88) Riley, C. R., S. I. Yun and W. A. Sibley, Phys. Rev. B 5, 3285 (1972).
- (89) Behringer, R. E., J. Chem. Phys. 29, 537 (1958).
- (90) Kreitman, M. M., and F. Hamaker, J. Chem. Phys. 45, 2396 (1966).
- (91) Turner, T. J., R. De Batist and Y. Haven, Phys. Stat. Sol. 11, 267 (1965).
- (92) Dreyfus, R. W., Phys. Rev. 1B, 4826 (1970).
- (93) Schneider, I., Phys. Rev. Letters 24, 1296 (1970).
- (94) Hughes, A. E., Ph.D. thesis (University of Oxford, 1966).
- (95) Farge, Y., G. Toulouse and M. Lambert, J. Phys. (Paris) 27, 287 (1966).
- (96) Baumann, G., W. Von der Osten and W. Waidelich, Z. Angew. Phys. 22, 246 (1967).
- (97) Wyckoff, R. W. G., Crystal Structures, Vol. 1 (Interscience, New York, 1963), p. 88.
- (98) Cotton, F. A., Chemical Applications of Group Theory (Wiley, New York, 1971).
- (99) Hunt, G. R., C. H. Perry and J. Ferguson, Phys. Rev. 134, A688 (1964).
- (100) Nakagawa, I., A. Tsuchida and T. Shimanouchi, J. Chem. Phys. 47, 982 (1967).
- (101) Gooen, K., B. Di Bartolo, M. Alam, R. C. Powell and A. Linz, Phys. Rev. 177, 615 (1969).
- (102) Green, R. L., D. D. Sell and R. S. Feigelson, Phys. Rev. 171, 600 (1968).

- (103) Green, R. L., D. D. Sell and R. M. White, Optical Properties of Ions in Crystals, edited by H. M. Crosswhite and H. W. Moos Interscience, New York, 1969), p. 289.
- (104) Dietz, R. E., A. E. Meixner and H. J. Guggenheim, J. of Luminescence 1, 2, 279 (1970).
- (105) Ikeya, M., and N. Itoh, J. Phys. Soc., Japan 29, 1295 (1970).
- (106) Ikeya, M., Phys. Stat. Sol. (b) 51, 409 (1972).
- (107) Jain, S. C. and K. Lal, in Non-Metallic Crystals, edited by S. C. Jain and L. T. Chadderton (Gordon and Breach, New York, 1969), p. 219.
- (108) Silsbee, R. H., Phys. Rev. 138, A180 (1965).

VITA

Soo In Yun

Candidate for the Degree of

Doctor of Philosophy

Thesis: OPTICAL STUDIES OF IMPURITIES AND RADIATION INDUCED DEFECTS IN
 KMgF_3

Major Field: Physics

Biographical:

Personal Data: Born in Kyungjoo, Korea, November 6, 1937, the son of Jang Suck and Kae Won Yun.

Education: Attended primary and middle schools in Pusan, Korea; graduated from Pusan Technical High School in 1956; received Bachelor of Science from Pusan National University with major in physics in March, 1960; received Master of Science degree in physics from Pusan National University, Pusan, Korea, in August, 1962; received Master of Science degree in physics from Carnegie-Mellon University, Pittsburgh, Pennsylvania, in May, 1970; attended Oklahoma State University, Stillwater, Oklahoma, 1970-1973; completed requirements for the Doctor of Philosophy degree in May, 1973.

Experience: Instructor in the Physics Department of the Pusan National University, Pusan, Korea (1964-1965); Staff Assistant in the Physics Department of the Pusan National University (1965-1966); Full-time Instructor in the Physics Department of the Pusan National University (1966-1968); Assistant Professor in the Physics Department of the Pusan National University (1968); Teaching Assistant in the Physics Department of the Carnegie-Mellon University, Pittsburgh, Pennsylvania (1968-1970); Teaching Assistant in the Physics Department of the Oklahoma State University, Stillwater, Oklahoma (1970-1971); Research Assistant in the Physics Department of the Oklahoma State University (1971-1972).

Organizations: Member of Sigma Pi Sigma, American Physical Society and Korean Physical Society.